



Universiteit Gent
Faculteit Wetenschappen
Vakgroep Fysica en Sterrenkunde

² No title yet

³ No sub-title neither, obviously...

⁴ Alexis Fagot

5



Thesis to obtain the degree of
Doctor of Philosophy in Physics
Academic years 2012-2017



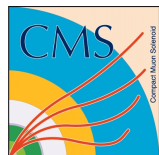


Universiteit Gent
Faculteit Wetenschappen
Vakgroep Fysica en Sterrenkunde

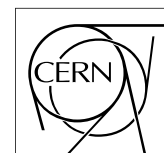
Promotoren: Dr. Michael Tytgat
Prof. Dr. Dirk Ryckbosch

Universiteit Gent
Faculteit Wetenschappen
Vakgroep Fysica en Sterrenkunde
Proeftuinstraat 86, B-9000 Gent, België
Tel.: +32 9 264.65.28
Fax.: +32 9 264.66.97

17



Thesis to obtain the degree of
Doctor of Philosophy in Physics
Academic years 2012-2017



Acknowledgements

¹⁹ Ici on remerciera tous les gens que j'ai pu croiser durant cette aventure et qui m'ont permis de passer
²⁰ un bon moment

²¹ *Gent, ici la super date de la mort qui tue de la fin d'écriture*
²² *Alexis Fagot*

Table of Contents

23

24	Acknowledgements	i
25	Nederlandse samenvatting	vii
26	English summary	ix
27	1 Introduction	1-1
28	1.1 A story of High Energy Physics	1-1
29	1.2 Organisation of this study	1-1
30	2 Investigating the TeV scale	2-1
31	2.1 The Standard Model of Particle Physics	2-2
32	2.1.1 A history of particle physics	2-2
33	2.1.2 Construction and test of the model	2-11
34	2.1.3 Investigating the TeV scale	2-12
35	2.2 The Large Hadron Collider & the Compact Muon Solenoid	2-14
36	2.2.1 LHC, the most powerful particle accelerator	2-14
37	2.2.1.1 Particle acceleration	2-15
38	2.2.2 CMS, a multipurpose experiment	2-18
39	2.2.2.1 The silicon tracker, core of CMS	2-20
40	2.2.2.2 The calorimeters, measurement of particle's energy	2-20
41	2.2.2.3 The muon system, corner stone of CMS	2-22
42	3 Muon Phase-II Upgrade	3-1
43	3.1 High Luminosity LHC	3-2
44	3.2 Muon system requirements through HL-LHC	3-3
45	3.3 Foreseen upgrades of DTs and CSCs	3-7
46	3.4 New detectors and increased acceptance	3-7
47	3.5 Implications of the different upgrades on the Level-1 Trigger	3-8
48	3.6 Improvement of physics performance	3-8
49	4 Physics of Resistive plate chambers	4-1
50	4.1 Principle	4-1
51	4.1.1 Electron drift velocity	4-4
52	4.2 Rate capability and time resolution of Resistive Plate Chambers	4-4
53	4.2.1 Operation modes	4-4
54	4.2.2 Detector designs and performance	4-6
55	4.2.2.1 Double-gap RPC	4-7
56	4.2.2.2 Multigap RPC (MRPC)	4-8
57	4.2.2.3 Charge distribution and performance limitations	4-9
58	4.3 Signal formation	4-12

59	4.4 Gas transport parameters	4-12
60	5 Longevity studies and Consolidation of the present CMS RPC subsystem	5-1
61	5.1 Resistive Plate Chambers at CMS	5-1
62	5.1.1 Overview	5-1
63	5.1.2 The present RPC system	5-2
64	5.1.3 Pulse processing of CMS RPCs	5-3
65	5.2 Testing detectors under extreme conditions	5-4
66	5.2.1 The Gamma Irradiation Facilities	5-7
67	5.2.1.1 GIF	5-7
68	5.2.1.2 GIF++	5-9
69	5.3 Preliminary tests at GIF	5-11
70	5.3.1 Resistive Plate Chamber test setup	5-11
71	5.3.2 Data Acquisition	5-13
72	5.3.3 Geometrical acceptance of the setup layout to cosmic muons	5-13
73	5.3.3.1 Description of the simulation layout	5-14
74	5.3.3.2 Simulation procedure	5-16
75	5.3.3.3 Results	5-17
76	5.3.4 Photon flux at GIF	5-17
77	5.3.4.1 Expectations from simulations	5-17
78	5.3.4.2 Dose measurements	5-22
79	5.3.5 Results and discussions	5-23
80	5.4 Longevity tests at GIF++	5-24
81	5.4.1 Description of the Data Acquisition	5-27
82	5.4.2 RPC current, environmental and operation parameter monitoring	5-28
83	5.4.3 Measurement procedure	5-29
84	5.4.4 Longevity studies results	5-29
85	6 Investigation on high rate RPCs	6-1
86	6.1 Rate limitations and ageing of RPCs	6-1
87	6.1.1 Low resistivity electrodes	6-1
88	6.1.2 Low noise front-end electronics	6-1
89	6.2 Construction of prototypes	6-1
90	6.3 Results and discussions	6-1
91	7 Conclusions and outlooks	7-1
92	7.1 Conclusions	7-1
93	7.2 Outlooks	7-1
94	A A data acquisition software for CAEN VME TDCs	A-1
95	A.1 GIF++ DAQ file tree	A-1
96	A.2 Usage of the DAQ	A-2
97	A.3 Description of the readout setup	A-3
98	A.4 Data read-out	A-3
99	A.4.1 V1190A TDCs	A-4
100	A.4.2 DataReader	A-6
101	A.4.3 Data quality flag	A-10
102	A.5 Communications	A-12
103	A.5.1 V1718 USB Bridge	A-13
104	A.5.2 Configuration file	A-13

105	A.5.3 WebDCS/DAQ intercommunication	A-17
106	A.5.4 Example of inter-process communication cycle	A-18
107	A.6 Software export	A-18
108	B Details on the offline analysis package	B-1
109	B.1 GIF++ Offline Analysis file tree	B-1
110	B.2 Usage of the Offline Analysis	B-2
111	B.2.1 Output of the offline tool	B-3
112	B.2.1.1 ROOT file	B-3
113	B.2.1.2 CSV files	B-5
114	B.3 Analysis inputs and information handling	B-6
115	B.3.1 Dimensions file and IniFile parser	B-6
116	B.3.2 TDC to RPC link file and Mapping	B-7
117	B.4 Description of GIF++ setup within the Offline Analysis tool	B-9
118	B.4.1 RPC objects	B-9
119	B.4.2 Trolley objects	B-10
120	B.4.3 Infrastructure object	B-11
121	B.5 Handeling of data	B-12
122	B.5.1 RPC hits	B-13
123	B.5.2 Clusters of hits	B-14
124	B.6 DAQ data Analysis	B-15
125	B.6.1 Determination of the run type	B-16
126	B.6.2 Beam time window calculation for efficiency runs	B-17
127	B.6.3 Data loop and histogram filling	B-18
128	B.6.4 Results calculation	B-19
129	B.6.4.1 Rate normalisation	B-19
130	B.6.4.2 Rate and activity	B-21
131	B.6.4.3 Strip masking tool	B-23
132	B.6.4.4 Output CSV files filling	B-25
133	B.7 Current data Analysis	B-29

¹³⁴

Nederlandse samenvatting –Summary in Dutch–

¹³⁵

¹³⁶ Le resume en Neerlandais (j'aurais peut-être pu apprendre la langue juste pour ça...).

English summary

¹³⁸ Le meme résume mais en Anglais (on commencera par la hein!).

List of Figures

139

140	2.1	Through the gold foil experiment Rutherford could show that most of the mass of atoms was contained in a positively charged nucleus and could then propose a more accurate atomic model than that of Thomson.	2-3
141	2.2	Figure 2.2a: Meson octet. Figure 2.2b: Baryon octet. Figure 2.2c: Baryon decuplet.	2-8
142	2.3	The elementary particles of the Standard Model are showed along with their names and properties. Their interactions with the strong, weak and electromagnetic forces have been explicated using color squares. In the left column, the scalar higgs boson is depicted, while the central is focused on the matter particles, the fermions, and the right on the force carriers, the gauge bosons. The role of the Higgs boson in electroweak symmetry breaking is highlighted, and the corresponding way properties of the various particles differ in the (high-energy) symmetric phase (top) and the (low-energy) broken-symmetry phase (bottom) are showed.	2-11
143	2.4	CERN accelerator complex.	2-15
144	2.5	Pictures of the different accelerators. From top to bottom: first the LINAC 2 and the <i>Pb</i> source of LINAC 3. Then the Booster and the LEIR. Finally, the PS, the SPS and the LHC.	2-16
145	2.6	Figure 2.6a: schematics of the LHC cryodipoles. 1: Superconducting Coils, 2: Beam pipe, 3: Heat exchanger Pipe, 4: Helium-II Vessel, 5: Superconducting Bus-bar, 6: Iron Yoke, 7: Non-Magnetic Collars, 8: Vacuum Vessel, 9: Radiation Screen, 10: Thermal Shield, 11: Auxiliary Bus-bar Tube, 12: Instrumentation Feed Throughs, 13: Protection Diode, 14: Quadrupole Bus-bars, 15: Spool Piece Bus-bars. Figure 2.6b: magnetic field and resulting motion force applied on the beam particles.	2-17
146	2.7	Figure 2.7a: picture of the LHC quadrupoles. Figure 2.7b: magnetic fields and resulting focussing force applied on the beam by 2 consecutive quadrupoles.	2-18
147	2.8	Picture of the CMS barrel. The red outer layer is the muon system hosted into the red iron return yokes. The calorimeters are the blue cylinder inside in magnet solenoid and the tracker is the inner yellow cylinder built around the beam pipe.	2-19
148	2.9	View of the CMS apparatus and of its different components.	2-19
149	2.10	Slice showing CMS sub-detectors and how particles interact with them.	2-20
150	2.11	CMS tracker.	2-20
151	2.12	Figure 2.12a: picture of the ECAL. Figure 2.12b: picture of the lead tungstate crystals composing the ECAL.	2-21
152	2.13	CMS hadron calorimeter barrel.	2-21
153	2.14	A quadrant of the muon system, showing DTs (yellow), RPCs (blue), and CSCs (green).	2-22
154	2.15	Figure 2.15a: Barrel wheel with its detector rings and return yokes. Figure 2.15b: CSC endcap disk with the 2 CSC stations. The outer station is made of 10 deg detectors while the inner station is made of 20 deg detectors. Figure 2.15c: RPC endcap disk. The inner station is not equipped and the inner CSC station can be seen.	2-23
155			
156			
157			
158			
159			
160			
161			
162			
163			
164			
165			
166			
167			
168			
169			
170			
171			
172			
173			
174			
175			
176			
177			
178			

- 179 2.16 Figure 2.16a: Cross section of a DT module showing the two superlayers measur-
 180 ing the ϕ coordinate, perpendicular to the cross section plane, and the superlayer
 181 measuring the η coordinate, placed in between the two others with honeycomb and
 182 parallel to the cross section plane. The DT detector is sandwiched in between 2
 183 RPCs whose readout strips are perpendicular to the cross section plane, measuring
 184 the ϕ coordinate. Figure 2.16b: A DT cell is shown together with its electric field.
 185 The path of a muon through a superlayer is shown. 2-23
- 186 2.17 Figure 2.17a: cathode strips and anode wire layout of a CSC panel. Figure 2.17b
 187 avalanche development and charge collection by anode wires and induction on cath-
 188 ode strips inside of a CSC panel. 2-24
- 189 2.18 Muon track reconstruction through the 6 panels of a CMS CSC using the infor-
 190 mation of anode wire groups and cathode strip charge distribution combined with
 191 comparator bits to decide on which half strip the muon is more likely to have passed. 2-24
- 192 2.19 Double gap layout of CMS RPCs. Muons passing through the gas volumes will cre-
 193 ate electron-ions pairs by ionising the gas. this ionisation will immediately translate
 194 into a developing avalanche. 2-25
- 195 3.1 Detailed timeline projection of for LHC and HL-LHC operation until 2039 show-
 196 ing the evolution of the instantaneous and integrated luminosity as designed (Fig-
 197 ure 3.1a) and in the ultimate case where the instantaneous luminosity is increased to
 198 $7.5 \times 10^{34} \text{ cm}^{-2}\text{s}^{-1}$ (Figure 3.1b) [20, 22]. 3-2
- 199 3.2 Absorbed dose in the CMS cavern after an integrated luminosity of 3000 fb. Using
 200 the interaction point as reference, R is the transverse distance from the beamline and
 201 Z is the distance along the beamline. 3-3
- 202 3.3 A quadrant of the muon system, showing DTs (yellow), RPCs (blue), and CSCs
 203 (green). The locations of new forward muon detectors for Phase-II are contained
 204 within the dashed box and indicated in red for GEM stations (ME0, GE1/1, and
 205 GE2/1) and dark blue for improved RPC (iRPC) stations (RE3/1 and RE4/1). 3-4
- 206 3.4 Figure 3.4a: extrapolated fraction of failing channels of the present DT MiC1 elec-
 207 tronics as a function of the integrated luminosity. Considering the most optimistic
 208 scenario, at least 19% of the channels could have failed by LS4, far before the end of
 209 the HL-LHC campain. Figure 3.4b: Comparison of the current (left) and upgraded
 210 (right) DT data processing. So far, the data is sent to service cavern of CMS facility
 211 via copper-to-optical-fiber translators (CuOF) by each MiC1. There, data including
 212 RPCs and outer hadron calorimeter is combined into trigger primitives (TPG) and
 213 transmitted by the TwinMux system to CMS Track Finder. The time-to-digital con-
 214 verter (TDC) data is collected and sent to the CMS data acquisition system (DAQ)
 215 by the micro read-out server (μ ROS). After the upgrade, the TDC data will be sent
 216 via optical links to a patch panel inside the experimental cavern by each MiC2, and
 217 transferred to the back-end, where triggering and event building will be performed. 3-5
- 218 3.5 Figure 3.5a: The event loss fractions as a function of the instantaneous luminosity is
 219 compared for CFEBs (Phase-1) and DCFEBs (Phase-II) at different CSC locations.
 220 HL-LHC luminosity is marked with the dashed brown line. Figure 3.5b: Comparison
 221 of the current (left) and upgraded (right) CSC data processing. A part of the con-
 222 nections in between ALCTs and DCFEBs, and the trigger mother boards (TMBs)
 223 and data acquisition mother boards (DMBs) will be upgraded toward optical data
 224 transfer. The detector dependent units (DDUs) used as interface in between CSCs'
 225 front-end electronics and the CMS DAQ will be replaced by new FED boards. 3-6

226	3.6	RMS of the multiple scattering displacement as a function of muon p_T for the proposed forward muon stations. All of the electromagnetic processes such as bremsstrahlung and magnetic field effect are included in the simulation.	3-8
229	4.1	Different phases of the avalanche development in the RPC gas volume subjected to a constant electric field E_0 . a) An avalanche is initiated by the primary ionisation caused by the passage of a charged particle through the gas volume. b) Due to its growing size, the avalanche starts to locally influence the electric field. c) The electrons, lighter than the cations reach the anode first. d) The ions reach the cathode. While the charges have not recombined, the electric field in the small region around the avalanche stays affected and locally blind the detector.	4-2
236	4.2	Efficiency (circles and stars with 30 mV and 100 mV thresholds respectively) and streamer probability (opened circles) as function of the operating voltatge of a 2 mm single gap HPL RPC flushed with a gas mixture containing (a) 5%, (b) 2%, (c) 1% and (d) no SF_6 [36].	4-3
240	4.3	Movement of the charge carriers in an RPC. Figure 4.3a: Voltage across an RPC whose electrode have a relative permittivity of 5 at the moment the tension s applied. Figure 4.3b: After the charge carriers moved, the electrodes are charged and there is no voltage drop over the electrodes anymore. The full potential is applied on the gas gap only. Figure 4.3c: The streamer discharge initiated by a charged particle transports electrons and cations towards the anode and cathode respectively.	4-5
246	4.4	Typical oscilloscope pulses in streamer mode (Figure 4.4a) and avalanche mode(Figure 4.4b). In the case of streamer mode, the very small avalanche signal is visible.	4-5
248	4.5	Rate capability comparison for the streamer and avalanche mode of operation. An order of magnitude in rate capability for a maximal efficiency drop of 10% is gained by using the avalanche mode over the streamer mode.	4-6
251	4.6	Possible double-gap RPC layouts: a) "standard" 1D double-gap RPC, as used in CMS experiment, where the anodes are facing each other and a 1D read-out plane is sandwiched in between them, b) double read-out double-gap RPC as used in ATLAS experiment, where the cathodes are facing each other and 2 read-out planes are used on the outer surfaces. This last layout can offer the possibility to use a 2D reconstruction by using orthogonal read-out planes.	4-7
257	4.7	Comparison of performance of CMS double and single gap RPCs using cosmic muons [47]. Figure 4.7a: Comparison of efficiency sigmoids. Figure 4.7b: Voltage distribution at 95% of maximum efficiency. Figure 4.7c: $\Delta_{10\%}^{90\%}$ distribution.	4-7
260	4.8	Presentation of ALICE MRPC using 250 μm gas gaps, 620 μm outer glass electrodes and 550 μm inner floating electrodes. More details on the labels are given in [48].	4-8
262	4.9	Particle identification applied to electrons in the STAR experiment. The identification is performed combining ToF and dE/dx measurements [53].	4-9
264	4.10	Comparison of the detector performance of ALICE ToF MRPC [54] at fixed applied voltage (in blue) and at fixed effective voltage (in red). The effective voltage is kept fixed by increasing the applied voltage accordingly to the current drawn by the detector.	4-9
267	4.11	Ratio between total induced and drifting charge have been simulated for single gap, double-gap and multigap layouts [55]. The total induced charge for a double-gap RPC is a factor 2 higher than for a multigap.	4-10
271	4.12	Charge spectra have been simulated for single gap, double-gap and multigap layouts [55]. It appears that when single gap shows a decreasing spectrum, double and multigap layouts exhibit a spectrum whose peak is detached from the origin. The detachment gets stronger as the number of gaps increases.	4-11

274	4.13 The maximal theoretical efficiency is simulated for single gap, double-gap and multi-gap layouts [55] at a constant gap thickness of 2 mm and using an effective Townsend coefficient of 9 mm^{-1}	4-11
277	5.1 Signals from the RPC strips are shaped by the FEE described on Figure 5.1a. Output LVDS signals are then read-out by a TDC module connected to a computer or converted into NIM and sent to scalers. Figure 5.1b describes how these converted signals are put in coincidence with the trigger.	5-3
281	5.2 Description of the principle of a CFD. A comparison of threshold triggering (left) and constant fraction triggering (right) is shown in Figure 5.2a. Constant fraction triggering is obtained thanks to zero-crossing technique as explained in Figure 5.2b. The signal arriving at the input of the CFD is split into three components. A first one is delayed and connected to the inverting input of a first comparator. A second component is connected to the noninverting input of this first comparator. A third component is connected to the noninverting input of another comparator along with a threshold value connected to the inverting input. Finally, the output of both comparators is fed through an AND gate.	5-4
290	5.3 (5.3a) Extrapolation from 2016 data of single hit rate per unit area in the barrel region. (5.3b) Extrapolation from 2016 data of single hit rate per unit area in the endcap region.	5-6
293	5.4 Background Fluka simulation compared to 2016 Data at $L = 10^{34} \text{ cm}^{-2} \cdot \text{s}^{-1}$ in the fourth endcap disk region. A mismatch in between simulation and data can be observed. [To be understood.]	5-7
296	5.5 Layout of the test beam zone called X5c GIF at CERN. Photons from the radioactive source produce a sustained high rate of random hits over the whole area. The zone is surrounded by 8 m high and 80 cm thick concrete walls. Access is possible through three entry points. Two access doors for personnel and one large gate for material. A crane allows installation of heavy equipment in the area.	5-8
301	5.6 ^{137}Cs decays by β^- emission to the ground state of ^{137}Ba (BR = 5.64%) and via the 662 keV isomeric level of ^{137}Ba (BR = 94.36%) whose half-life is 2.55 min.	5-9
303	5.7 Floor plan of the GIF++ facility. When the facility downstream of the GIF++ takes electron beam, a beam pipe is installed along the beam line (z-axis). The irradiator can be displaced laterally (its center moves from $x = 0.65 \text{ m}$ to 2.15 m), to increase the distance to the beam pipe.	5-9
307	5.8 Simulated unattenuated current of photons in the xz plane (Figure 5.8a) and yz plane (Figure 5.8b) through the source at $x = 0.65 \text{ m}$ and $y = 0 \text{ m}$. With angular correction filters, the current of 662 keV photons is made uniform in xy planes.	5-10
310	5.9 Description of the RPC setup. Dimensions are given in mm. A tent containing RPCs is placed at 1720 mm from the source container. The source is situated in the center of the container. RE-4-2-BARC-161 chamber is 160 mm inside the tent. This way, the distance between the source and the chambers plan is 2060 mm. Figure 5.9a provides a side view of the setup in the xz plane while Figure 5.9b shows a top view in the yz plane.	5-11
316	5.10 RE-4-2-BARC-161 chamber is inside the tent as described in Figure 5.9. In the top right, the two scintillators used as trigger can be seen. This trigger system has an inclination of 10° relative to horizontal and is placed above half-partition B2 of the RPCs. PMT electronics are shielded thanks to lead blocks placed in order to protect them without stopping photons from going through the scintillators and the chamber.	5-12

321	5.11 Hit distributions over all 3 partitions of RE-4-2-BARC-161 chamber is showed on these plots. Top, middle and bottom figures respectively correspond to partitions A, B, and C. These plots show that some events still occur in other half-partitions than B2, which corresponds to strips 49 to 64, in front of which the trigger is placed, contributing to the inefficiency of detection of cosmic muons. In the case of partitions A and C, the very low amount of data can be interpreted as noise. On the other hand, it is clear that a little portion of muons reach the half-partition B1, corresponding to strips 33 to 48.	5-13
329	5.12 Results are derived from data taken on half-partition B2 only. On the 18 th of June 2014, data has been taken on chamber RE-2-BARC-161 at building 904 (Prevessin Site) with cosmic muons providing us a reference efficiency plateau of $(97.54 \pm 0.15)\%$ represented by a black curve. A similar measurement has been done at GIF on the 21 st of July with the same chamber giving a plateau of $(78.52 \pm 0.94)\%$ represented by a red curve.	5-14
335	5.13 Representation of the layout used for the simulations of the test setup. The RPC is represented as a yellow trapezoid while the two scintillators as blue cuboids looking at the sky. A green plane corresponds to the muon generation plane within the simulation. Figure 5.9a shows a global view of the simulated setup. Figure 5.9b shows a zommed view that allows to see the 2 scintillators as well as the full RPC plane.	5-15
340	5.14 γ flux $F(D)$ is plot using values from table 5.1. As expected, the plot shows similar attenuation behaviours with increasing distance for each absorption factors.	5-18
342	5.15 Figure 5.15a shows the linear approximation fit done via formulae 5.7 on data from table 5.2. Figure 5.15b shows a comparison of this model with the simulated flux using a and b given in figure 5.15a in formulae 5.4 and the reference value $D_0 = 50\text{cm}$ and the associated flux for each absorption factor F_0^{ABS} from table 5.1	5-20
346	5.16 Dose measurements has been done in a plane corresponding to the tents front side. This plan is 1900 mm away from the source. As explained in the first chapter, a lens-shaped lead filter provides a uniform photon flux in the vertical plan orthogonal to the beam direction. If the second line of measured fluxes is not taken into account because of lower values due to experimental equipments in the way between the source and the tent, the uniformity of the flux is well showed by the results.	5-22
352	5.17	5-23
353	5.18 Evolution of the maximum efficiency for RE2 (5.18a) and RE4 (5.18b) chambers with increasing extrapolated γ rate per unit area at working point. Both irradiated (blue) and non irradiated (red) chambers are shown.	5-25
356	5.19 Evolution of the working point for RE2 (5.19a) and RE4 (5.19b) with increasing extrapolated γ rate per unit area at working point. Both irradiated (blue) and non irradiated (red) chambers are shown.	5-25
359	5.20 Evolution of the maximum efficiency at HL-LHC conditions, i.e. a background hit rate per unit area of 300 Hz/cm ² , with increasing integrated charge for RE2 (5.20a) and RE4 (5.20b) detectors. Both irradiated (blue) and non irradiated (red) chambers are shown. The integrated charge for non irradiated detectors is recorded during test beam periods and stays small with respect to the charge accumulated in irradiated chambers.	5-26
365	5.21 Comparison of the efficiency sigmoid before (triangles) and after (circles) irradiation for RE2 (5.21a) and RE4 (5.21b) detectors. Both irradiated (blue) and non irradiated (red) chambers are shown.	5-26
368	5.22 Evolution of the Bakelite resistivity for RE2 (5.22a) and RE4 (5.22b) detectors. Both irradiated (blue) and non irradiated (red) chambers are shown.	5-27
369		

370	5.23 Evolution of the noise rate per unit area for the irradiated chamber RE2-2-BARC-9 only.	5-27
372	A.1 (A.1a) View of the front panel of a V1190A TDC module [61]. (A.1b) View of the 373 front panel of a V1718 Bridge module [62]. (A.1c) View of the front panel of a 6U 374 6021 VME crate [63].	A-3
375	A.2 Module V1190A <i>Trigger Matching Mode</i> timing diagram [61].	A-4
376	A.3 Structure of the ROOT output file generated by the DAQ. The 5 branches (<code>EventNumber</code> , 377 <code>number_of_hits</code> , <code>Quality_flag</code> , <code>TDC_channel</code> and <code>TDC_TimeStamp</code>) are visible on 378 the left panel of the ROOT browser. On the right panel is visible the histogram cor- 379 responding to the variable <code>nHits</code> . In this specific example, there were approximately 380 50k events recorded to measure the gamma irradiation rate on the detectors. Each 381 event is stored as a single entry in the <code>TTree</code>	A-10
382	A.4 The effect of the quality flag is explained by presenting the content of <code>TBranch</code> 383 <code>number_of_hits</code> of a data file without <code>Quality_flag</code> in Figure A.4a and the con- 384 tent of the same <code>TBranch</code> for data corresponding to a <code>Quality_flag</code> where all TDCs 385 were labelled as <code>GOOD</code> in Figure A.4b taken with similar conditions. It can be noted 386 that the number of entries in Figure A.4b is slightly lower then in Figure A.4a due 387 to the excluded events.	A-12
388	A.5 Using the same data as previously showed in Figure A.4, the effect of the quality 389 flag is explained by presenting the reconstructed hit multiplicity of a data file with- 390 out <code>Quality_flag</code> in Figure A.5a and the reconstructed content of the same RPC 391 partition for data corresponding to a <code>Quality_flag</code> where all TDCs were labelled as 392 <code>GOOD</code> in Figure A.5b taken with similar conditions. The artificial high content of bin 393 0 is completely suppressed.	A-12
394	A.6 WebDCS DAQ scan page. On this page, shifters need to choose the type of scan 395 (Rate, Efficiency or Noise Reference scan), the gamma source configuration at the 396 moment of data taking, the beam configuration, and the trigger mode. These in- 397 formation will be stored in the DAQ ROOT output. Are also given the minimal 398 measurement time and waiting time after ramping up of the detectors is over before 399 starting the data acquisition. Then, the list of HV points to scan and the number of 400 triggers for each run of the scan are given in the table underneath.	A-14
401	B.1 Example of expected hit time distributions in the cases of efficiency (Figure B.1a) 402 and noise/gamma rate per unit area (Figure B.1b) measurements as extracted from 403 the raw ROOT files. The unit along the x-axis corresponds to ns. The fact that 404 "the" muon peak is not well defined in Figure B.1a is due to the contribution of all 405 the RPCs being tested at the same time that don't necessarily have the same signal 406 arrival time. Each individual peak can have an offset with the ones of other detectors. 407 The inconsistancy in the first 100 ns of both time distributions is an artefact of the 408 TDCs and are systematically rejected during the analysis.	B-16
409	B.2 The effect of the quality flag is explained by presenting the reconstructed hit multi- 410 plicity of a data file without <code>Quality_flag</code> . The artificial high content of bin 0 is the 411 effect of corrupted data.	B-19

List of Tables

420

421	4.1 Properties of the most used electrode materials for RPCs.	4-4
422	5.1 Total photon flux ($E\gamma \leq 662$ keV) with statistical error predicted considering a	
423	^{137}Cs activity of 740 GBq at different values of the distance D to the source along	
424	the x-axis of irradiation field [58].	5-17
425	5.2 Correction factor c is computed thanks to formulae 5.5 taking as reference $D_0 =$	
426	50 cm and the associated flux F_0^{ABS} for each absorption factor available in table 5.1. .	5-19
427	5.3 The data at D_0 in 1997 is taken from [58]. In a second step, using Equations 5.8	
428	and 5.9, the flux at D can be estimated in 1997. Then, taking into account the	
429	attenuation of the source activity, the flux at D can be estimated at the time of the	
430	tests in GIF in 2014. Finally, assuming a sensitivity of the RPC to γ $s = 2 \cdot 10^{-3}$,	
431	an estimation of the hit rate per unit area is obtained.	5-21
432	A.1 Inter-process communication cycles in between the webDCS and the DAQ through	
433	file string signals.	A-19

434

List of Acronyms

435

436

437

A

438

439

440

AFL Almost Full Level
ALCTs anode local charged track boards

442

443

B

444

445

446

BARC Bhabha Atomic Research Centre
BLT Block Transfer
BNL Brookhaven National Laboratory
BR Branching Ratio

450

451

452

453

C

454

CAEN Costruzioni Apparecchiature Elettroniche Nucleari S.p.A.
CERN European Organization for Nuclear Research
CFD Constant Fraction Discriminator
CFEBs cathode front-end boards
CMB Cosmic Microwave Background
CMS Compact Muon Solenoid
CSC Cathode Strip Chamber
CuOF copper-to-optical-fiber translators

462

463

464

465

D

466

DAQ Data Acquisition
DCS Detector Control Software
DQM Data Quality Monitoring
DT Drift Tube

470		
471	E	
472		
473		
474	ECAL	electromagnetic calorimeter
475		
476	F	
477		
478		
479	FCC	Future Circular Collider
480	FEE	Front-End Electronics
481	FEB	Front-End Board
482		
483	G	
484		
485		
486	GE-/-	Find a good description
487	GE1/1	Find a good description
488	GE2/1	Find a good description
489	GEANT	GEometry ANd Tracking - a series of software toolkit platforms developed by CERN
490		
491	GEM	Gas Electron Multiplier
492	GIF	Gamma Irradiation Facility
493	GIF++	new Gamma Irradiation Facility
494		
495	H	
496		
497		
498	HCAL	hadron calorimeter
499	HL-LHC	High Luminosity LHC
500	HPL	High-pressure laminate
501	HV	High Voltage
502		
503	I	
504		
505		
506	iRPC	improved RPC
507	IRQ	Interrupt Request
508	ISR	Intersecting Storage Rings
509		
510		
511	L	
512		

513	LEIR	Low Energy Ion Ring
514	LEP	Large Electron-Positron
515	LHC	Large Hadron Collider
516	LS1	First Long Shutdown
517	LS2	Second Long Shutdown
518	LS3	Third Long Shutdown
519	LV	Low Voltage
520	LVDS	Low-Voltage Differential Signaling

521

522

M

524

525	MiC1	first version of Minicrate electronics
526	MC	Monte Carlo
527	MCNP	Monte Carlo N-Particle
528	ME-/	Find good description
529	ME0	Find good description
530	MRPC	Multigap RPC

531

532

N

534

535	NIM	Nuclear Instrumentation Module logic signals
-----	-----	--

536

537

P

539

540	PMT	PhotoMultiplier Tube
541	PS	Proton Synchrotron
542	PU	pile-up

543

544

Q

546

547	QCD	Quantum Chromodynamics
548	QED	Quantum Electrodynamics

549

550

R

552

553	RE-/	Find a good description
554	RE2/2	Find a good description
555	RE3/1	Find a good description

556	RE3/2	Find a good description
557	RE4/1	Find a good description
558	RE4/2	Find a good description
559	RE4/3	Find a good description
560	RMS	Root Mean Square
561	ROOT	a framework for data processing born at CERN
562	RPC	Resistive Plate Chamber

563

564

S

566

567	SC	Synchrocyclotron
568	SLAC	Stanford Linear Accelerator Center
569	SM	Standard Model
570	SPS	Super Proton Synchrotron
571	SUSY	supersymmetry

572

573

T

574

576	TDC	Time-to-Digital Converter
577	TDR	Technical Design Report
578	ToF	Time-of-flight
579	TPG	trigger primitives

580

581

W

583

584	webDCS	Web Detector Control System
-----	--------	-----------------------------

585

586

Y

588

589	YETS	Year End Technical Stop
-----	------	-------------------------

1

Introduction

590

591

⁵⁹² **1.1 A story of High Energy Physics**

⁵⁹³ **1.2 Organisation of this study**

2

594

595

Investigating the TeV scale

596 „We may regard the present state of the universe as the effect of the
597 past and the cause of the future. An intellect which at any given mo-
598 ment knew all of the forces that animate nature and the mutual posi-
599 tions of the beings that compose it, if this intellect were vast enough
600 to submit the data to analysis, could condense into a single formula
601 the movement of the greatest bodies of the universe and that of the
602 lightest atom; for such an intellect nothing could be uncertain and
603 the future just like the past would be present before its eyes.”

604

605 - Pierre Simon de Laplace, *A Philosophical Essay on Probabilities*, 1814

Throughout history, physics experiment became more and more powerful in order to investigate finer details of nature and helped understanding the elementary blocks of matter and the fundamental interactions that bond them in the microscopic world. Nowadays, the Standard Model (SM) of particle physics is the most accurate theory designed to explain the behaviour of particles and was able to make very precise predictions that are constantly verified, although some hints of new physics are visible as bricks are still missing to have a global comprehension of the Universe.

To highlight the limits of the SM and test the different alternative theories, ever more powerful machines are needed. This is in this context that the Large Hadron Collider (LHC) has been thought and built to accelerate and collide particles at energies exceeding anything that had been done before. Higher collision energies and high pile-up imply the use of enormous detectors to measure the properties of the interaction products. The Compact Muon Solenoid (CMS) is a multipurpose experiment that have been designed to study the proton-proton collisions of the LHC and give answers on various high energy physics scenari. Nevertheless, the luminosity delivered by the collider will in the future be increased to levels beyond the original plans to improve its discovery potential giving no choice to experiments such as CMS to upgrade their technologies to cope with the increased radiation levels and detection rates.

2.1 The Standard Model of Particle Physics

In this early 21st century it is now widely accepted that matter is made of elementary blocks referred to as *elementary particles*. The physics theory that classifies and describes the best the behaviour and interaction of such elementary particles is the so called Standard Model that formalizes 3 of the 4 fundamental interactions (electromagnetic, weak and strong interactions). It's development took place during the 20th century thanks to a strong collaboration in between the theoretical and experimental physicists.

2.1.1 A history of particle physics

The idea that nature is composed of elementary bricks, called *atomism*, is not contemporary as it was already discussed by Indian or Greek philosophers during antiquity. In Greece, atomism has been rejected by Aristotelianism as the existance of *atoms* would imply the existance of a void that would violate the physical principles of Aristotle philosophy. Aristotelianism has been considered as a reference in the european area until the 15th century and the italian *Rinascimento* where antic text and history started to be more deeply studied. The re-discovery of Platon's philosophy would allow to open the door to alternative theories and give a new approach to natural sciences where experimentation would become central. A new era of knowledge was starting. By the begining of the 17th century, atomism was re-discovered by philosophers and the very first attempt to estimate an *atom* size would be provided by Magnetus in 1646. Although his *atoms* correspond to what would nowadays be called *molecules*, Magnetus achieved feats by calculating that the number of molecules in a grain of incense would be of the order of 10^{18} simply by considering the time necessary to smell it everywhere in a large church after the stick was lit on. It is now known that this number only falls short by 1 order of magnitude.

An alternative philosophy to atomism popularized by Descartes was corpuscularianism. Built on ever divisible corpuscles, contrary to atoms, it's principles would be mainly used by alchemists like Newton who would later develop a corpuscular theory of light. Boyle would combine together ideas of both atomism or corpuscularianism leading to mechanical philosophy. The 18th century have

seen the development of engineering providing philosophical thought experiments with repeatable demonstration and a new point of view to explain the composition of matter and Lavoisier would greatly contribute to chemistry and atomism by publishing in 1789 a list of 33 chemical elements corresponding to what is now called *atoms*. In the early 19th century Dalton would summarize the knowledge on composition of matter and Fraunhofer would invent the spectrometer and discover the spectral lines. The rise of atomic physics, chemistry and mathematical formalism would unravel the different atomic elements and ultimately, the 20th century would see the very first sub-atomic particles.

Discovery of the inner structure of the atom

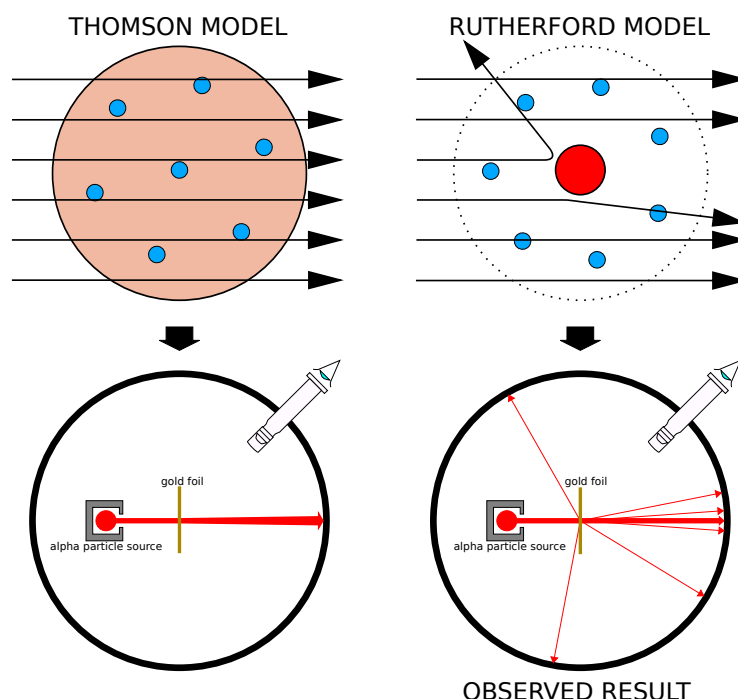


Figure 2.1: Through the gold foil experiment Rutherford could show that most of the mass of atoms was contained in a positively charged nucleus and could then propose a more accurate atomic model than that of Thomson.

The negative *electron* would be the first to be discovered in 1897 by Thomson after 3 decades of research on cathode rays by proving that the electrification observed in an electroscope, as reported by Perrin, was due to the rays themselves and that they had to be composed of electrically charged particles. In 1900, Becquerel would show the *beta rays* emitted by radium had the same charge over mass ratio than what measured by Thomson for cathode rays, pointing to electrons as a constituent of atoms. In 1907, Rutherford and Royds showed that *alpha* particles, once captured in a tube and subjected to an electric spark causing an electron avalanche, where helium ions as they could combine with 2 electrons to form a ${}^4\text{He}$. This discovery was directly followed by the constraint of the atom structure in 1909 through the gold foil experiment in which the deflection angle of alpha particles fired at a very thin gold foil was measured and highlighted atoms where mainly empty with

667 nearly all its mass contained into a tiny positively charged *nucleus*. With these two observations,
 668 he could formulate the Rutherford model of the atom in 1911, shown together with the Thomson
 669 plum pudding model in Figure 2.1. The link in between atomic number and number of positive and
 670 negative charges contained into the atoms would fast be understood and the different kind of element
 671 transmutation appeared to be purely nuclear processes making clear that the electromagnetic nature
 672 of chemical transformation could not possibly change nuclei. Thus a new branch in physics appeared
 673 to study nuclei exclusively: the nuclear physics.

674 Moreover, in 1913 quantum physics would be introduced into the atomic model by Bohr based
 675 on the assumptions of Plank to explain spectral lines, and other observed quantum effects. The same
 676 year, Moseley would confirm Borh's model and Debye would extend it by introducing elliptical
 677 orbits.

678 By studying alpha emission and the product of their interaction with nitrogen gas, Rutherford
 679 reported in 1919 the very first nuclear reaction leading to the discovery that the hydrogen nucleus was
 680 composed of a single positively charged particle that was later baptised *proton*. This idea came from
 681 1815 Prout's hypothesis proposing that all atoms are composed of "*protyles*" (i.e. hydrogen atoms).
 682 By using scintillation detectors, Rutherford could highlight typical hydrogen nuclei signature and
 683 understand that the impact of alpha particles with nitrogen would knock out an hydrogen nucleus
 684 and produce an oxygen 17, as explicated in Formula 2.1 and would then postulate that protons are
 685 building bricks of all elements.



686 With this assumption and the discovery of isotopes together with Aston, elements with identical
 687 atomic number but different masses, Rutherford would propose that all elements' nuclei but hydrogen's are composed of both charged particles, protons, and of chargeless particles, which he called
 688 *neutrons*, and that these neutral particles would help maintaining nuclei as one, as charged protons
 689 were likely to electrostatically repulse each other, and introduced the idea of a new force, a *nuclear*
 690 force. Though the first idea concerning neutrons was a bond state of protons and electrons as it was
 691 known that the beta decay, emitting electrons, was taking place in the nucleus, it was then showed
 692 that such a model would hardly be possible due to Heisenberg's uncertainty principle and by the
 693 recently measured *spin* of both protons and electrons. The spin, discovered through the study of
 694 the emission spectrum of alkali metals, would be understood as a "two-valued quantum degree of
 695 freedom" and formalized by Pauli and extended by Dirac, to take the relativist case into account.
 696 Measured to be $\frac{1}{2}\hbar$ for both, it was impossible to arrange an odd number of half integer spins and
 697 obtain a global nucleus spin that would be integer. Finally, in 1932, following the discovery of a new
 698 neutral radiation, Chadwick could discover the neutron as an uncharged particle with a mass similar
 699 to that of the proton whose half integer spin would reveal to be the solution to explain the nuclear
 700 spin.

702 Development of the Quantum Electrodynamics

703 Historically, the development of the quantum theory revolved around the question of emission and
 704 absorption of discrete amount of energy through light. Einstein used the initial intuition of Plank
 705 about the black-body radiation to develop in 1905 a model to explain the photoelectric effect in
 706 which light was described by discrete quanta now called *photons*. For this model, Einstein introduced
 707 the concept of wave-particle duality as classical theory was not able to describe the phenomenon.
 708 With the new understanding of atoms and of their structure, classical theories also proved unable

709 to explain atoms stability. Indeed, using classical mechanics, electrons orbiting around a nucleus
 710 should radiate an energy proportional to their angular momentum and thus lose energy through
 711 time and the spectrum of energy emission should then be continuous, but it was known since the
 712 19th century and the discovery of spectral lines that the emission spectrum of material was discrete.

713 This was Bohr who first suggested that a quantum description of the atom was necessary in 1913.
 714 Using the correspondence principle stating that at large enough numbers the quantum calculations
 715 should give the same results than the classical theory, he proposed the very first quantum model
 716 of the hydrogen atom explaining the line spectrum by introducing the principal quantum number
 717 n describing the electron shell. This model would then be improved by Sommerfeld that would
 718 quantize the z-component of the angular momentum, leading to the second and third quantum
 719 numbers, or azimuthal and magnetic quantum number, l and m defining for the second the orbital
 720 angular momentum of the electrons on their shells and thus, the shape of the orbital, and for the third
 721 the available orbital on the subshell for each electron. Nevertheless, although the model was not only
 722 limited to spherical orbitals anymore, making the atom more realistic, the Zeeman effect couldn't be
 723 completely explained by just using n , l and m . A solution would be brought after the discovery of
 724 Pauli in 1924, as Uhlenbeck, Goudsmit, and Kramers proposed in 1925 the idea of intrinsic rotation
 725 of the electron, introducing a new angular momentum vector associated to the particle itself, and
 726 not to the orbital, and associated to a new quantic number s , the *spin* projection quantum number
 727 explaining the lift of degeneracy to an even number of energy levels.

728 The introduction of the *spin* happened 1 year after another attempt of improvement of the theory
 729 was made by De Broglie in his PhD thesis. The original formulation of the quantum theory only
 730 considered photons as energy quanta behaving as both waves and particles. De Broglie proposed
 731 that all matter are described by waves and that their momentum is proportional to the oscillation of
 732 quantized electromagnetic field oscillators. This interpretation was able to reproduce the previous
 733 version of the quantum energy levels by showing that the quantum condition involves an integer
 734 multiple of 2π , as shown by Formula 2.2.

$$p = \hbar k \Leftrightarrow \int pdx = \hbar \int kdx = 2\pi\hbar n \quad (2.2)$$

735 Although the intuition of De Broglie about the wave-particle duality of all matter, his interpretation
 736 was semiclassical and it's in 1926 that the first fully quantum mechanical wave-equation would
 737 be introduced by Schrödinger to describe electron-like particles, reproducing the previous semiclassical
 738 formulation without inconsistencies. This complexe equation describes the evolution of the
 739 wave function Ψ of the quantum system, defined by its position vector \mathbf{r} and time t as an energy
 740 conservation law, in which the hamiltonian of the system \hat{H} is explicit, by solving the Equation 2.3.

$$i\hbar \frac{\partial}{\partial t} |\Psi(\mathbf{r}, t)\rangle = \hat{H} |\Psi(\mathbf{r}, t)\rangle \quad (2.3)$$

741 In 1927, Dirac would go further in his paper about emission and absorption of radiation by
 742 proposing a second quantization not only of the physical process at play but also of the electromagnetic
 743 field, providing the ingredients to the first formulation of *Quantum Electrodynamics (QED)*
 744 and the description of photon emission by electrons dropping into a lower energy state in which the
 745 final number of particles is different than the initial one. To complete this model to the many-body
 746 wave functions of identical particles, Jordan included creation and annihilation operators for fields
 747 obeying Fermi-Dirac statistics leading to a model describing particles that would be referred to as
 748 *fermions*. Nevertheless, in order to properly treat electromagnetism, the incorporation of the relativ-

ity theory developed by Einstein. Including gravity into quantum physics still is a challenge nowadays, but in 1928 Pauli and Jordan would show that special relativity's coordinate transformations could be applied to quantum fields as the field commutators were Lorentz invariant. Finally derived the same year, the Dirac equation, shown as Equation 2.4, similarly to Schrödinger's equation, is a single-particle equation but it incorporates special relativity in addition to quantum mechanics rules. It features the 4×4 gamma matrices γ^μ built using 2×2 Pauli matrices and unitary matrix, the 4-gradient ∂_μ , the rest mass m of any half integer spin massive particle described by the wave function $\psi(x, t)$, also called a Dirac spinor, and the speed of light c . In addition to perfectly reproduce the results obtained with quantum mechanics so far, it also provided with *negative-energy solutions* that would later be interpreted as a new form of matter, *antimatter* and give a theoretical justification to the Pauli equation that was phenomenologically constructed to account for the spin as in the non-relativistic limit, the Dirac equation is similar.

$$i\hbar\gamma^\mu\partial_\mu\psi - mc\psi = 0 \quad (2.4)$$

The successes of the QED was soon followed with theoretical problems as computations of any physical process involving photons and charged particles were showed to be only reliable at the first order of perturbation theory. At higher order of the theory, divergent contributions were appearing giving nonsensical results. Only two effects were contributing to these infinities.

- The self-energy of the electron (or positron), the energy that the particle has due its own interaction with its environment.
- The vacuum polarization, virtual electron–positron pairs produced by a background electromagnetic field in the vacuum which is not an "empty" space. These virtual pairs affect the charge and current distributions generated by the original electromagnetic field.

Solving this apparent problem was done by carefully defining the concepts of each observables, for example mass or charge, as these quantities are understood within the context of a non-interacting field equation, and that from the experiment point of view, they are abstractions as what is measured are "renormalized observables" shifted from there "bare" value by the interaction taking place in the measuring process. The infinities needed to be connected to corrections of mass and charge as those are fixed to finite values by experiment. This was the intuition of Bethe in 1947 who successfully computed the effect of such *renormalization* in the non-relativist case. Fully covariant formulations of QED including renormalization was achieved by 1949 by Tomonaga, Schwinger, Feynman and Dyson and Feynman is now famous for his association of diagrams to the term of the scattering matrix, greatly simplifying the representation and computation of interactions as the diagrams directly corresponded the measurable physical processes and would then be used in every quantum field theories. With the resolution of infinities, QED had mostly reached its final form, being still today the most accurate physical theory and would serve as a model to build all other quantum field theories.

Development of the quark model and Quantum Chromodynamics

To explain the nuclear force that holds *nucleons* (protons and neutrons) together, Yukawa theoretically proposed in 1934 the existence of a force carrier called *meson* due to it's predicted mass in the range in between the electron and nucleon masses. Discovered in 1936 by Anderson and Neddermeyer, and confirmed using bubble chambers in 1937 by Street and Stevenson, a first meson

789 candidate was observed in the decay products of cosmic rays. Assuming it had the same electric
 790 charge than electrons and protons, this particle was observed to have a curvature due to magnetic
 791 field that was sharper than protons but smoother than electrons resulting in a mass in between that
 792 of electrons and protons. But its properties were not compatible with Yukawa's theory, which was
 793 emphasized by the discovery of a new candidate in 1947, again in cosmic ray products using photo-
 794 graphic emulsions.

795 This new candidate, although it had a similar mass than the already believed *meson*, would rather
 796 decay into it. For distinction, the first candidate would then be renamed "*mu meson*" when the second
 797 would be the "*pi meson*". The *mu meson* was behaving like a heavy electron and didn't participate
 798 in the strong interaction whereas the pion was believed to be the carrier of the nuclear interaction.
 799 This lead to classify the *mu* in a new category of particles called *leptons* together with the electron
 800 that shared similar properties and *the neutrino*, and be renamed *muon*. The *pi meson* was finally
 801 found to be a triplet of particles: a positively charged, a negatively charged, and a neutral particle.
 802 The neutral *pi meson* has been more difficult to identify as it wouldn't leave tracks on emulsions nor
 803 on bubble chambers and needed to be studied via it's decay products. It was ultimately identified in
 804 University of California's cyclotron in 1950 through the observation of its decay into 2 photons.

805 Also discovered in 1947 but in cloud chamber photographs, the *K meson* as also been an im-
 806 portant step towards the establishment of the Standard Model. A triplet of particle, 2 charged and a
 807 neutral, with a mass roughly half that of a proton, were reported. These particles were baptised *K*
 808 *meson* in contrast to the "light" *pi* and *mu* "L-mesons". The particularity of the *K* were there very
 809 slow decays with a typical lifetime of the order of 10^{-10} s much greater than the 10^{-23} s of *pi*-proton
 810 reactions. The concept of *strangeness*, a new quantum number was then introduced by Pais as an
 811 attempt to explain this phenomenon as *strange* particles appeared as a pair production of a strange
 812 and anti-strange particle.

813 With the development of synchrotrons, the particle *zoo* would grow to several dozens during the
 814 1950s as higher energies were reachable through acceleration. In 1961, a first classification system,
 815 called Eightfold Way, was proposed by Gell-Mann and finding its roots in the Gell-Mann–Nishijima
 816 formula, which relates the electric charge Q , the third component of the isospin I_3 , the *baryon*
 817 number B and the strangeness S , as explicitated in Formula 2.5. The isospin was a quantum number
 818 introduced in 1932 to explain symmetries of the newly discovered neutron using representation
 819 theory of SU(2). The baryon number, was introduced by Nishijima as a quantum number for baryons,
 820 i.e. particles of the same family as nucleons. The mesons were classified in an octet and baryons of
 821 spin $\pm \frac{1}{2}$ and $\pm \frac{3}{2}$ were respectively classified into an octet and a decuplet, as shown in Figure 2.2. To
 822 complete the baryon decuplet, Gell-Mann predicted the existance of baryon Ω^- which would later
 823 be discovered in 1964.

$$Q = I_3 + \frac{1}{2}(B + S) \quad (2.5)$$

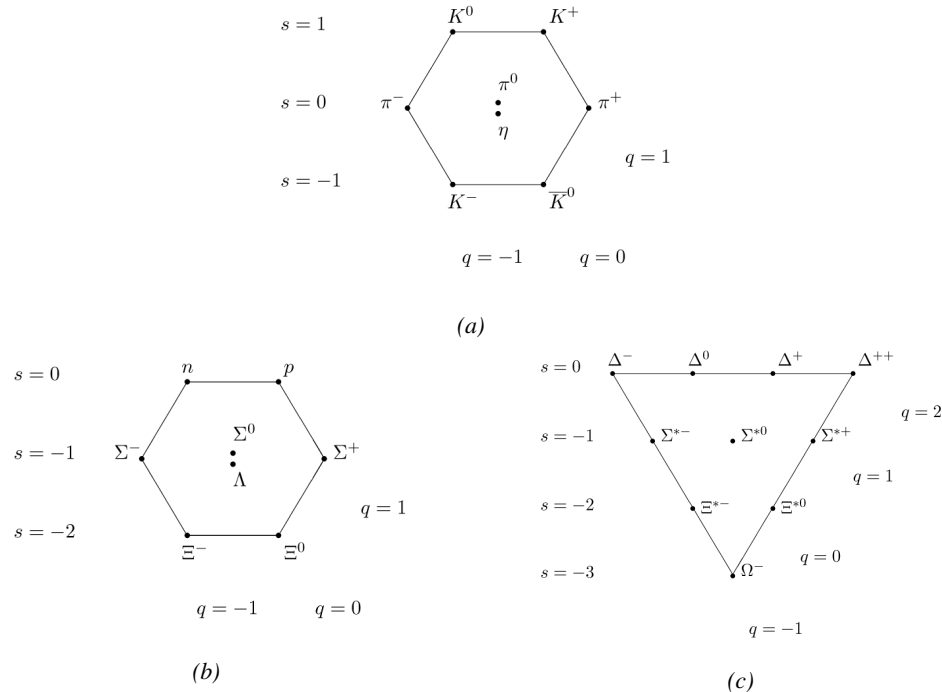


Figure 2.2: Figure 2.2a: Meson octet. Figure 2.2b: Baryon octet. Figure 2.2c: Baryon decuplet.

Strong of this classification using an SU(3) flavor symmetry, Gell-Mann, and independently Zweig, would propose a full theoretical model in which *hadrons* (strongly interacting particles, i.e. mesons and baryons) were not elementary particles anymore. They would rather be composed with 3 flavors of particles called *quarks* and there anti-particles. The 3 flavors were called *up*, *down* and *strange*. *Up* and *down* would be used to explain the nucleons and non-strange mesons, while *strange* would come into the composition of hadrons showing strangeness. *Up* and *down* flavors would be discovered in 1968 thanks to the deep inelastic scattering experiments conducted at the Stanford Linear Accelerator Center (SLAC), and *strange* could only be indirectly validated even though it provided a robust explanation to *kaon* (K) and *pion* (π). However, in the decade following the Gell-Mann-Zweig quark model proposition, several improvement to the model were brought, first by Glashow and Bjorken the same year that predicted the existence of a fourth quark flavor, the *charm*, that would equalize the then known number of quarks and leptons and finally in 1973 by Kobayashi and Maskawa that would increase the number of quarks to 6 to explain the experimental observation of CP violation. These two quarks would be referred to as *top* and *bottom* for the first time in 1975. It's only after these additions to the quark model that finally the *charm* would be discovered in 1974 at both SLAC and Brookhaven National Laboratory (BNL). A meson where the *charm* was bound with an *anti-charm*, called J/ψ , would help convince the physics community of the validity of the model. The *top* would be discovered soon after in 1977 in Fermilab and indicate the existence of the *bottom* that would resist to discovery until Fermilab's experiments CDF and D \emptyset in 1995 due to its very large mass and the energy needed to produce it.

As remarked by Struminsky, the original quark model proposal composed of 3 quarks should possess an additional quantum number due to mesons such as Ω^- or Δ^{++} . Indeed, these mesons are composed of 3 identical quarks, respectively 3 *strange* and *up* quark, with parallel spins, which

should be forbidden by the exclusion principle. Independentle, Greenberg and Han-Nambu proposed an additional SU(3) degree of freedom possessed by the quarks, that would later be refered to as *color charge gauge*, that could interact through *gluons*, the gauge boson octet corresponding to this degree of freedom. Nevertheless, as observing free quarks proved to be impossible, two visions of the quarks were argued mainly due to the failures to observe these particles free to prove their existence. On one side, Gell-Mann proposed to see quarks as mathematical construct instead of real particles, as they are always confined, implying that quantum field theory would not describe entirely the strong interaction. Opposed to this vision, Feynman on the contrary argued that quarks were real particles, that he would call *partons*, that should be described as all other particles by a distribution of position and momentum. The implications of quarks as point-like particles would be verified at SLAC and the concept of *color* would be added to the quark model in 1973 by Fritzsch and Leutwyler together with Gell-Mann to propose a description of the strong interaction through the theory of Quantum Chromodynamics (QCD). The discovery the same year of asymptotic freedom within the QCD by Groos, Politzer and Wilczek, allowed for very precise predictions thanks to the perturbation theory. Nowadays, the confinement of quarks is studied in experiments such as ALICE, through exploration of the quark-gluon plasma.

863 The Weak interaction, spontaneous symmetry breaking, the Higgs mechanism and the Elec- 864 troweak unification

865 The weak interaction is the process that causes radioactive decays. Thanks to the neutron discovery,
866 Fermi could explain in 1934 the beta radiations through the beta decay process in which the neutron
867 decays into a proton by emitting an electron. Though the missing energy observed during this
868 process triggered a huge debate about the apparent non conservation of energy, momentum and spin
869 of the process, Fermi, as Pauli before him, proposed that the missing energy was due to a neutral
870 not yet discovered particle that would then be baptised *neutrino*. The impossibility to detect such
871 a particle would leave some members of the scientific community sceptical, but hints of energy
872 conservation and of the existence of the neutrino were provided by measuring the energy spectrum
873 of electrons emitted through beta decay, as there was a strict limit on their energy. It's only 30 years
874 later in 1953 that it would be discovered by the team of Cowan and Reines using the principle of
875 inverse beta decay described through Formula 2.6. The experiment consisted in placing water tanks
876 sandwiched in between liquid scintillators near a nuclear reactor with an estimated neutrino flux of
877 $5 \times 10^{13} \text{ s}^{-1} \text{ cm}^{-2}$. However, in order to explain the absence of some reactions in the experiment
878 of Cowan and Reines, and constraint the beta decay theory of Fermi and extend it to the case of
879 the muon, Konopinski and Mahmoud proposed in 1953 that the muon decay would eject a particle
880 similar to the neutrino and thus predicted the existence of a muon neutrino that would be different
881 than the one involved in the beta decay, related to the electron. With this, the idea of lepton number
882 would arise. The muon neutrino would successfully be detected in 1962 by Lederman, Schwartz and
883 Steinberger.

$$\bar{\nu} + p \rightarrow n + e^+ \quad (2.6)$$

884 The theory could not be valid though as the probability of interaction, called cross-section, would
885 have been increasing without bond with the square of the energy. Fermi assumed in a two vector
886 current coupling but Lee and Yang noted that an axial current could appear and would violate parity.
887 The experiment of Wu in 1956 would confirm the parity violation and Gamow and Teller would try to
888 account for it by describing Fermi's interaction through allowed (parity-violating) and superallowed

889 (parity-conserving) decays. But the success of QED as a quantum field theory would spark the
890 development of such a theory to describe the weak interaction.

891 As previously discussed, the great success of QED was built on an underlying symmetry, interpreted
892 as a gauge invariance so that the effect of the force is the same in all space-time coordinates,
893 and of the possibility to renormalize it in order to absorb the infinities. Independently in 1958,
894 Glashow, and Salam and Ward used 1957 Schwinger ideas about vector intermediary for the decay
895 processes, could find a way to unite both the electromagnetic and weak interaction into a gauge
896 theory involving 4 gauge bosons, 3 of which were massive and carried out the weak interaction and
897 a massless boson carrying the electromagnetic interaction. Among the 3 massive bosons, 2 were
898 charged and 1 was neutral, similarly to the previously theorized *pi meson* vector of the Yukawa
899 model and all have a mass much greater than nucleons and thus a very short life time implying a
900 finite very short range contrary to the contact interaction originally proposed by Fermi.

901 Breakthrough in other fields of physics contributed in giving theoretical support and interpretation
902 to the unified electroweak theory. The stepping stone would be the use of spontaneous symmetry
903 breaking that was inspired to Nambu at the end of the 1950s following the development of the BCS
904 superconductivity mechanism in 1957. Cooper had shown that BCS pairs, pairs of electrons bound
905 together at low temperature, could have lower energy than the Fermi energy and where responsible
906 for superconductivity. This lead to the discovery of Goldstone-Nambu bosons as a result of the
907 spontaneous breaking of the chiral symmetry in a theory describing nucleons and mesons developed
908 by Nambu and Jona-Lasinio in 1961, and now understood as a low-energy approximation of
909 QCD. Similarly to mechanism of energy gap appearance in superconductivity, the nucleon mass
910 is suggested to the result of a self-energy of a fermion field and is studied through a four-fermion
911 interaction in which, as a consequence of the symmetry, bound states of nucleon-antinucleon pairs
912 appear and can be regarded as virtual pions. Though the symmetry is maintained in the equations,
913 the ground state is not preserved. Goldstone would later the same year show that the bound states
914 corresponds to spinless bosons with zero mass.

915 Although the model in itself didn't revolutionize particle physics, spontaneous symmetry breaking
916 would be generalized to quantum field theories. As all fundamental interactions are described
917 using gauge theories based on underlying symmetries, processes such as the chiral symmetry breaking
918 would be introduced soon after the publication of Nambu and Jona-Lasinio. In 1962, Anderson,
919 following an idea of Schwinger who suggested that zero-mass vector bosons were not necessarily
920 required to describe the conservation of baryons contrary to the bosons emerging from chiral symmetry
921 breaking, discussed the implications of spontaneous symmetry breaking in particles physics.
922 A model was finally independently built in 1964 by Brout and Englert, Higgs, and Guralnik, Hagen,
923 and Kibble, who discovered that combining an additional field into a gauge theory in order to break
924 the symmetry, the resulting gauge bosons acquire a nonzero mass. Moreover, Higgs stated that this
925 implied the existence of at least one new massive, i.e. self-interacting, scalar boson, that are now
926 known as *Higgs bosons* corresponding to this additional field. The Higgs mechanism today specifically
927 refers to the process through which the gauge bosons of the weak interaction acquire mass. In
928 1968, Weinberg could point to the Higgs mechanism to integrate a Higgs field into a new version
929 of the electroweak theory in which the spontaneous symmetry breaking mechanism of the Higgs
930 field would explicitly explain the masses of the weak interaction gauge bosons and the zero-mass
931 of photons.

932 2.1.2 Construction and test of the model

933 The Standard Model of particle physics was built in the middle of the 1970s after the experimental
 934 confirmation of the existence of quarks. It is based on the assembly of the models previously introduced
 935 and describing the fundamental interactions, except for gravitation, and their gauge bosons
 936 as well as the way elementary "matter" particles interact with the fields associated with these force
 937 carriers. In this sense, the development of QED and the unification of the electroweak interaction,
 938 of the Yukawa interaction and of QCD, and of the Higgs mechanism made it possible to explain most
 939 of contemporary physics.

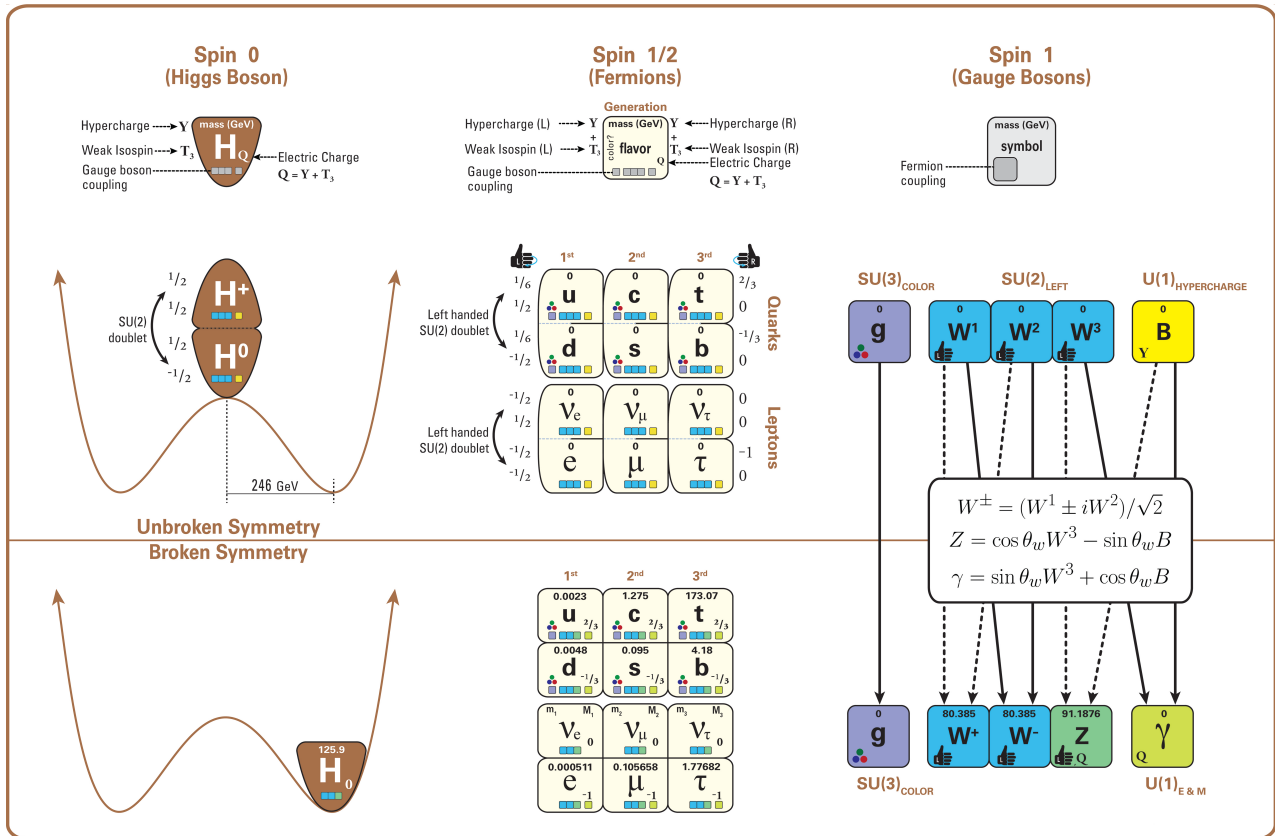


Figure 2.3: The elementary particles of the Standard Model are showed along with their names and properties. Their interactions with the strong, weak and electromagnetic forces have been explicited using color squares. In the left column, the scalar higgs boson is depicted, while the central is focused on the matter particles, the fermions, and the right on the force carriers, the gauge bosons. The role of the Higgs boson in electroweak symmetry breaking is highlighted, and the corresponding way properties of the various particles differ in the (high-energy) symmetric phase (top) and the (low-energy) broken-symmetry phase (bottom) are showed.

940 In the SM, "matter" particles, are described by 12 fermion fields of spin $\frac{1}{2}$ obeying the Fermi-
 941 Dirac statistics, i.e. subjected to the Pauli exclusion principle. To each fermion is associated its
 942 corresponding antiparticle. The fermions are classified according to the way they interact and, thus,
 943 according to the charges they carry. 6 of them are classified as quarks (u, d, c, s, t , and b) and
 944 are subjected to all interactions and the 6 others as leptons ($e^-, \mu^-, \tau^-, \nu_e, \nu_\mu$, and ν_τ). Leptons

945 are not subjected to the strong interaction and among them, the 3 neutrinos only interact weakly as
 946 they are neutral particles, which explains why they are so difficult to detect. The gauge boson fields
 947 are the gluons g for the strong interaction, the photon γ for the electromagnetic interaction and the
 948 weak bosons W^+ , W^- , and Z^0 for the weak interaction. Finally, the Higgs field H^0 is responsible,
 949 through the spontaneous symmetry breaking, of the mixing of the massless electroweak boson fields
 950 W_1 , W_2 , W_3 , and B leading to the observable states γ , W^+ , W^- , and Z^0 that can gain mass while
 951 interacting with the Higgs field. This picture of the SM is summarized through Figure 2.3 where the
 952 antifermions are not showed.

953 When the model was first finalized, the existence of the weak gauge bosons, of the charm, of the
 954 third quark generation composed of top and bottom quarks to explain the observed CP violation was
 955 not proven but the predictions were measured with good precision in the years following. First, the
 956 charm quark would be discovered in 1974, followed by the bottom quark in 1977. The weak bosons
 957 would be discovered during the next decade in 1983. The top quark would resist until 1995 due to
 958 its very large mass but would offer the last piece of the elementary QCD particles. The very last
 959 predicted elementary particle of the model that was not observed yet would prove to be very difficult
 960 to observe. the Higgs boson needed the start of the LHC to finaly be oberved in 2012. A few years
 961 more of tests were necessary to measure its properties to confirm the observation of a scalar boson
 962 compatible with the predicted Higgs boson H^0 . Eventhough only quark-antiquark (mesons) and 3
 963 quark states (baryons) were observed, exotic hadrons were not forbidden by QCD and no limit of
 964 quark is imposed by the theory. Moreover, gluons could form bond states by themselves and with
 965 quarks. These two types of states are called *glueballs* and *hybrid hadrons*. For decades, experi-
 966 ments have been conducted without confirmation of such possible states existing. Nevertheless, in
 967 2014, tetraquarks were observed by LHCb, one of LHC's main experiments, and in 2015, the same
 968 experiment reported the discovery of pentaquarks making the SM one of the best tested theories of
 969 physics.

970 2.1.3 Investigating the TeV scale

971 Even though the SM is a well tested theory, several hints of physics going beyond its scope have
 972 been observed. First of all, gravity is not explained through this model and huge difficulties are en-
 973 countered when trying to include gravitation. The strength of gravitational interaction is expected to
 974 be negligible at the scale of elementary particles, nevertheless, adding gravitation in the perspective
 975 of developing a "theory of everything" leads to divergent integrals that could not be fixed through
 976 renormalization.

977 Moreover, the SM considers neutrinos to be massless but it was shown in the late 1960s by the
 978 Homestake experiment that the flux of solar neutrinos (i.e. ν_e) measured didn't match the predicted
 979 values due to neutrino oscillations, confirmed in the early 2000s by the Sudbury Neutrino Obser-
 980 vatory. This oscillation implies that neutrinos that can be observed are a superposition of massive
 981 neutrino states. The research on neutrino oscillation is already quite advanced with experiments
 982 looking at atmospheric, reactor or beam neutrinos in order to determine the elements of the mixing
 983 matrix similar to the CKM matrix describing the mixing of quarks. Nevertheless, no answer to the
 984 origin of neutrino mass is provided.

985 Another intriguing fact is that the universe is dominated by matter. However, the SM predicted
 986 that matter and antimatter should have been created in equal amounts and no mechanism is able to
 987 explain this matter-antimatter asymmetry. Although this asymmetry is seen from the visible uni-
 988 verse, it may be possible that other unknown regions of the Universe are dominated by antimatter.

989 Another possibility to explain the apparent asymmetry would be the existence of a electric dipole
990 in any fundamental particle that would permit matter and antimatter particles to decay at different
991 rates.

992 The discrepancy of velocity dispersion of stars in galaxies with respect to the visible mass they
993 contain is known since the end of the 19th century where Kelvin proposed that this problem could
994 be solved if a "*great majority of [the stars] would be dark bodies*". Throughout the 20th century,
995 physicists like Kapteyn, Zwicky, showed the first hints of a "*dark matter*" by studying star veloc-
996 ities and galactic clusters, followed by robust measurements of galaxy rotation curves by Babcock
997 which suggested that the mass-to-luminosity ratio was different from what would be expected from
998 watching the visible light. Later in the 1970s, Rubin and Ford from direct light observations and
999 Rogstad and Shostak from radio measurements showed that the radial velocity of visible objects in
1000 galaxies was increasing with increasing distance to the center of the galaxy. Finally observation of
1001 lensing effect by galaxy clusters, temperature distribution of hot gas in galaxies and clusters, and
1002 the anisotropies in the Cosmic Microwave Background (CMB) kept on pointing to a "*dark matter*".
1003 From all the data accumulated, the visible matter would only account to no more than 5% of the total
1004 content on the visible universe. Alternative theories have tried to investigate modified versions of
1005 the General Relativity as this theory is only well tested at the scale of the solar system but is not suf-
1006 ficiently tested on wider ranges or even theories in which gravitation is not a fundamental force but
1007 rather an emergent one, but so far, such theories have difficulties to reproduce all the experimental
1008 observations as easily as through dark matter.

1009 A possible theory to offer dark matter candidates would be supersymmetry (SUSY) which pro-
1010 poses a relationship in between bosons and fermions. In this model, each elementary particle,
1011 through a spontaneous spacetime symmetry breaking mechanism would have a *super partner* from
1012 the other family of particles. On top of providing heavy dark matter candidates, supersymmetry
1013 could also help solving the *Hierarchy problem*, the very large scale difference in between the weak
1014 interaction and gravity, although, as mentioned before, in the case gravity is found not to be a funda-
1015 mental force, this problem would automatically fade.

1016

1017 All these different aspects of physics beyond the Standard Model of particle physics and the
1018 Standard model itself can be tested through the use of very energetic and intense hadron and ion col-
1019 liders. The LHC at CERN is a perfect tool to seek answers to these open questions except maybe for
1020 the gravity as gravity is extremely weak at particles level. For example, one of LHCb experiment's
1021 goal is to investigate CP-violation and thus baryonic asymmetry. In 2017, the collaboration has an-
1022 nounced to have so far a 3.3σ statistical significance over a CP-violation through the study of the
1023 decays of Λ_b^0 and $\overline{\Lambda}_b^0$ into a proton (or antiproton) and 3 pions. Many analysis teams are also working
1024 hard on supersymmetry both in ATLAS and CMS collaborations, the two multipurpose experiments
1025 of LHC, even though no evidence of a supersymmetrical theory was seen, the few hint having the
1026 tendency to confirm the standard model. These experiments also have the possibility to investigate
1027 ways to explain Majorana neutrino mass through Yukawa interactions of scalar particles.

1028

1029 The higher the center-of-mass energy, the smaller details the experiments will be able to see, the
1030 heavier the potential particle creation barrier will be, the stronger the cross-section of certain rare
1031 decay channels will be. As a comparison, with collisions happening at 14 TeV, the LHC is approxi-
1032 mately 2 orders of magnitude more sensitive to the Higgs than the Tevatron was with its already very
1033 powerful 2 TeV. All these advantages eventually lead to new discoveries and deeper understanding
1034 of the models describing our Universe. But the LHC only is a step forward to gather more precise
tests of the Standard Model and new knowledge about the physics beyond it. A successful physics

1035 campaign will probably serve to justify the building of new accelerators with even greater discovery
 1036 potential like for example the Future Circular Collider (FCC) that would push even further the study
 1037 of the unanswered questions of contemporary physics.

1038 2.2 The Large Hadron Collider & the Compact Muon Solenoid

1039 Throughout its history, CERN has played a leading role in high energy particle physics. Large re-
 1040 gional facilities such as CERN were thought after the second world war in an attempt to increase
 1041 international scientific collaboration and allows scientists to share the forever increasing costs of
 1042 experiment facilities required due to the need for increasing the energy in the center of mass to
 1043 deeper probe matter. The construction of the first accelerators at the end of the 50s, the Synchro-
 1044 cyclotron (SC) and the Proton Synchrotron (PS), was directly followed by the first observation of
 1045 antinuclei in 1965 [1]. Strong from the experience of the Intersecting Storage Rings (ISR), the very
 1046 first proton-proton collider that showed hints that protons are not elementary particles, the Super
 1047 Proton Synchrotron (SPS) was built in the 70s to investigate the structure of protons, the preference
 1048 for matter over antimatter, the state of matter in the early universe or exotic particles, and lead to
 1049 the discovery in 1983 of the W and Z bosons [2–5]. These newly discovered particles and the elec-
 1050 troweak interaction would then be studied in details by the Large Electron-Positron (LEP) collider
 1051 that will help to prove in 1989 that there only are three generations of elementary particles [6]. The
 1052 LEP would then be dismantled in 2000 to allow for the LHC to be constructed in the existing tunnel.

1053 2.2.1 LHC, the most powerful particle accelerator

1054 The LHC has always been considered as an option to the future of CERN. At the moment of the
 1055 construction of the LEP beneath the border between France and Switzerland, the tunnel was built in
 1056 order to accomodate what would be a Large Hadron Collider with a dipole field of 10 T and a beam
 1057 energy in between 8 and 9 TeV [7] directly followed in 1985 with the creation of a 'Working Group
 1058 on the Scientific and Technological Future of CERN' to investigate such a collider [8]. The decision
 1059 was finally taken almost 10 years later, in 1994, to construct the LHC in the LEP tunnel [9] and the
 1060 approval of the 4 main experiments that would take place at the 4 interaction points would come in
 1061 1997 [10] and 1998 [11]:

- 1062 • ALICE [12] has been designed in the purpose of studying quark-gluon plasma that is believed
 1063 to have been a state of matter that existed in the very first moment of the universe.
- 1064 • ATLAS [13] and CMS [14] are general purpose experiments that have been designed with
 1065 the goal of continuing the exploration of the Standard Model and investigate new physics.
- 1066 • LHCb [15] has been designed to investigate the preference of matter over antimatter in the
 1067 universe through the CP violation.

1068 These large scale experiments, as well as the full CERN accelerator complex, are displayed on
 1069 Figure 2.4. The LHC is a 27 km long hadron collider and the most powerful accelerator used for
 1070 particle physics since 2008 [16]. The LHC was originally designed to collide protons at a center-
 1071 of-mass energy of 14 TeV and luminosity of $10^{34} \text{ cm}^{-2}\text{s}^{-1}$, as well as Pb ions at a center-of-mass
 1072 energy of 2.8 TeV/A with a peak luminosity of $10^{27} \text{ cm}^{-2}\text{s}^{-1}$. Run 1 of LHC, when the center-of-
 1073 mass energy only was half of the nominal LHC energy, was enough for both CMS and ATLAS to

discover the Higgs boson [17] and for LHCb to discover pentaquarks [18] and confirm the existance of tetraquarks [19]. Nevertheless, after the Third Long Shutdown (LS3) (2024-2026), the accelerator will be in the so called High Luminosity LHC (HL-LHC) configuration [20], increasing its instantaneous luminosity to $10^{35} \text{ cm}^{-2}\text{s}^{-1}$ for pp collisions and to $4.5 \times 10^{27} \text{ cm}^{-2}\text{s}^{-1}$, boosting the discovery potential of the LHC. The HL-LHC phase should last at least another 10 years depending on the breakthrough this machine would lead to. Already a new accelerating device, the FCC, as been proposed to prepare the future of high energy physics after the LHC.

CERN's Accelerator Complex

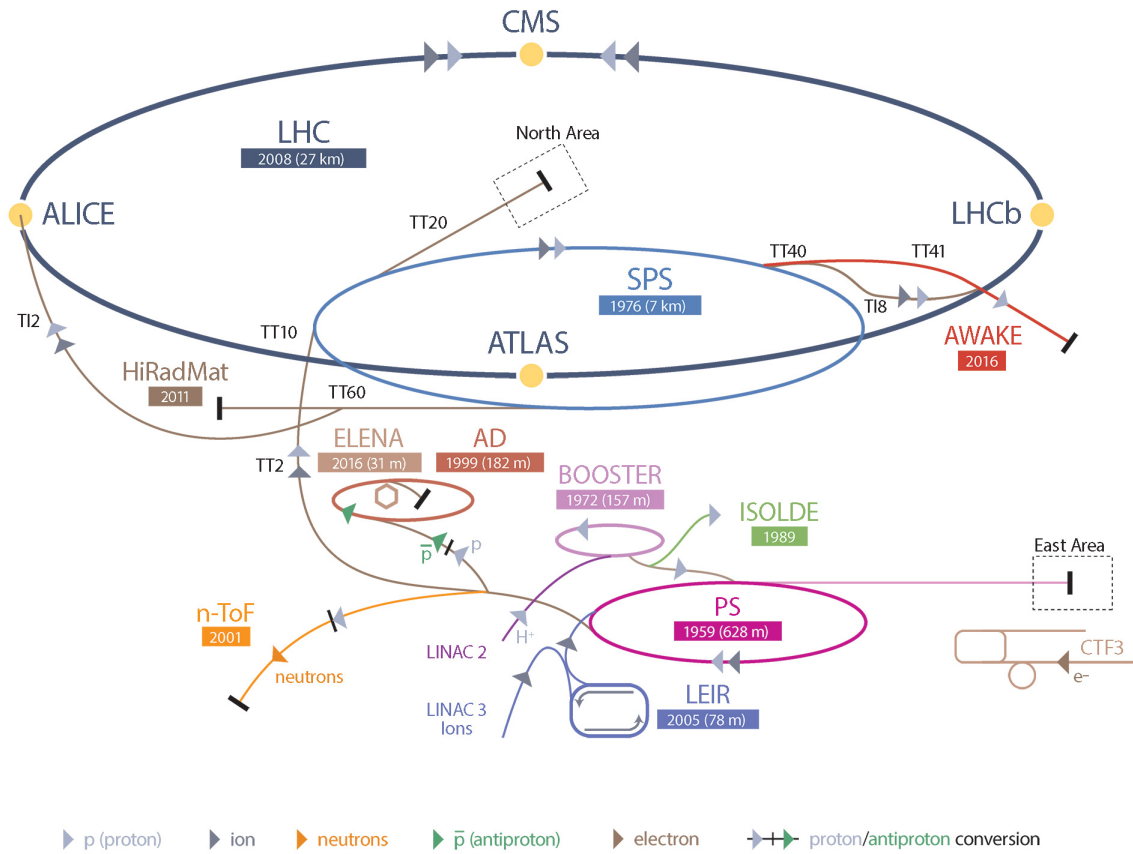


Figure 2.4: CERN accelerator complex.

2.2.1.1 Particle acceleration

The LHC is the last of a long series of accelerating devices. Before being accelerated by the LHC, the particles need to pass through different acceleration stages. All these acceleration stages are visible on Figure 2.4 and pictures of the accelerators are showed in Figure 2.5.

The story of accelerated protons at CERN starts with a bottle of hydrogen gas injected into the source chamber of the linear particle accelerator *LINAC 2* in which a strong electric field strips the

1088 electron off the hydrogen molecules only to keep their nuclei, the protons. The cylindrical conductors,
 1089 alternatively positively or negatively charged by radiofrequency cavities, accelerate protons by
 1090 pushing them from behind and pulling them from the front and ultimately give them an energy of
 1091 50 MeV, increasing their mass by 5% in the process.

1092

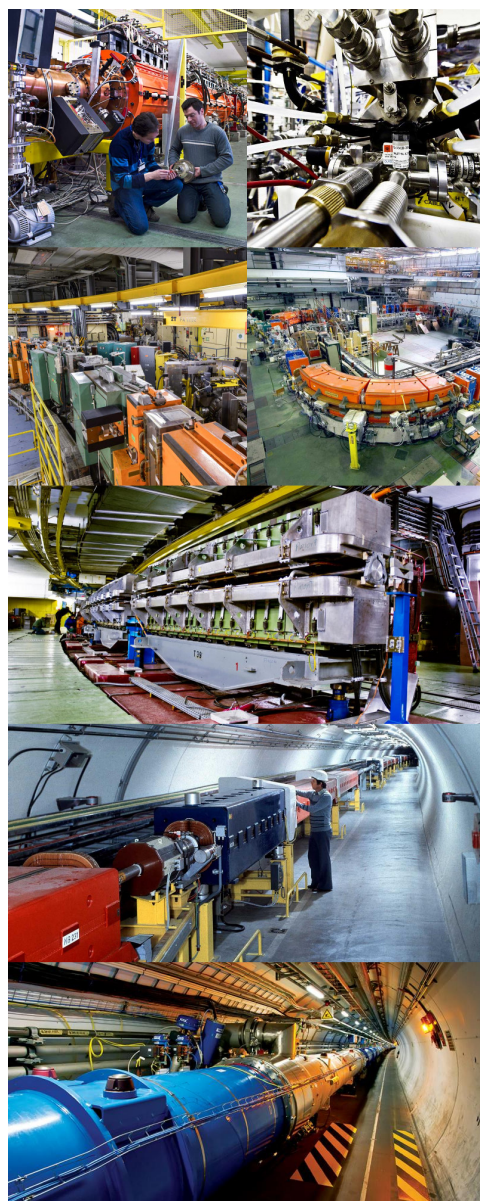


Figure 2.5: Pictures of the different accelerators. From top to bottom: first the LINAC 2 and the Pb source of LINAC 3. Then the Booster and the LEIR. Finally, the PS, the SPS and the LHC.

1093 When exiting the LINAC 2, the protons are divided into 4 bunches and injected into the 4 su-
 1094 perimposed synchrotron rings of the *Booster* where they are then accelerated to reach an energy of

1095 1.4 GeV before being injected into the PS. Before the Booster was operational in 1972, the protons
 1096 were directly injected into the PS from the LINAC 2 but the low injection energy limited the amount
 1097 of protons that could be accelerated at once by the PS. With the Booster, the PS accepts approxi-
 1098 mately 100 times more particles.

1099

1100 The 4 proton bunches are thus sent as one to the PS where their energy eventually reaches
 1101 26 GeV. Since the 70s, the main goal of this 628 m circumference synchrotron has been to sup-
 1102 ply other machines with accelerated particles. Nowadays, not only the PS accelerates protons, it also
 1103 accelerates heavy ions from the *Low Energy Ion Ring (LEIR)*. Indeed, the LHC experiments are not
 1104 only designed to study *pp*-collisions but also *Pb*-collisions. Lead is first injected into the dedicated
 1105 linear collider *LINAC 3*, that accelerate the ions using the same principle than LINAC 2. Electrons
 1106 are striped off the lead ions all along the acceleration process and eventually, only bare nuclei are
 1107 injected in the LEIR whose goal is to transform the long ion pulses received into short dense bunches
 1108 for LHC. Ions injected and stored in the PS were aceelerated by the LEIR from 4.2 MeV to 72 MeV.

1109

1110 Directly following the PS, is finally the last acceleration stage before the LHC, the 7 km long
 1111 *SPS*. The SPS accelerates the protons to 450 GeV and inject proton in both LHC accelerator rings
 1112 that will increase their energy up to 7 TeV. When the LHC runs with heavy lead ions for ALICE
 1113 and LHCb, ions are injected and accelerated to reach the energy of 2.8 TeV/A.

1114

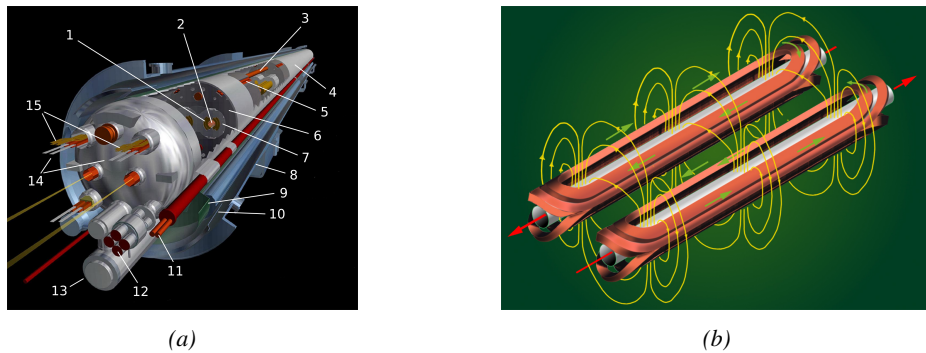


Figure 2.6: Figure 2.6a: schematics of the LHC cryodipoles. 1: Superconducting Coils, 2: Beam pipe, 3: Heat exchanger Pipe, 4: Helium-II Vessel, 5: Superconducting Bus-bar, 6: Iron Yoke, 7: Non-Magnetic Collars, 8: Vacuum Vessel, 9: Radiation Screen, 10: Thermal Shield, 11: Auxiliary Bus-bar Tube, 12: Instrumentation Feed Throughs, 13: Protection Diode, 14: Quadrupole Bus-bars, 15: Spool Piece Bus-bars. Figure 2.6b: magnetic field and resulting motion force applied on the beam particles.

1115

1116 The LHC beams are not continuous and are rather organised in bunch of paticles. When in *pp*-
 1117 collision mode, the beams are composed of 2808 bunches of 1.15×10^{11} protons separated by 25 ns.
 1118 When in *Pb* collision mode, the 592 *Pb* bunches are on the contrary composed of 2.2×10^8 ions
 1119 separated by 100 ns. The two parrallel proton beams of the LHC are contained in a single twin-
 1120 bore magnet due to the space restriction in the LEP tunnel. Indeed, building 2 completely separate
 1121 accelerator rings next to each other was impossible. The dipoles of the 1232 twin-bore magnets are
 1122 showed in Figure 2.6 alongside the magnetic field generated along the dipole section to accelerate the
 1123 particles. The dipoles generate a nominal field of 8.33 T, needed to give protons and lead nucleons
 their nominal energy. Some 392 quadrupoles, presented in Figure 2.7, are also used to focus to the

¹¹²⁴ beams, as well as other multipoles to correct smaller imperfections.

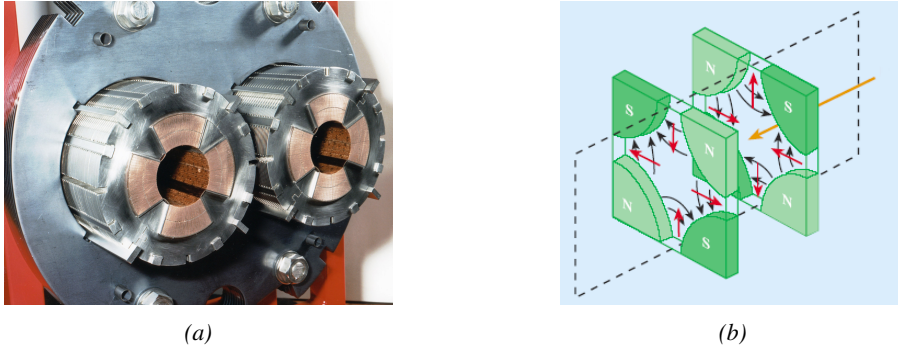


Figure 2.7: Figure 2.7a: picture of the LHC quadrupoles. Figure 2.7b: magnetic fields and resulting focussing force applied on the beam by 2 consecutive quadrupoles.

¹¹²⁵ 2.2.2 CMS, a multipurpose experiment

¹¹²⁶ Among the four main LHC experiments is the Compact Muon Solenoid used as a multipurpose tool to
¹¹²⁷ investigate the SM and physics beyond its scope. Proposed through a letter of intention in 1992 [14],
¹¹²⁸ and as its name suggests, this very compact detector's uses the muons as a clear tag of most of SM
¹¹²⁹ and new physics interesting channels. In the original 1997 Technical Design Report (TDR) [21], the
¹¹³⁰ very first sentences were stating that "*Muons are an unmistakable signature of most of the physics*
¹¹³¹ *LHC is designed to explore. The ability to trigger on and reconstruct muons at the highest lumi-*
¹¹³² *nosities is central to the concept of CMS, the Compact Muon Solenoid.*" CMS participated in the
¹¹³³ discovery of the Higgs boson and the measurement of its properties and couplings together with
¹¹³⁴ ATLAS and is also actively involved in the search for SUSY and heavy ion collisions. Other exotic
¹¹³⁵ physics are also being investigated using the data collected by CMS.

¹¹³⁶ The CMS apparatus in itself is the heaviest detector ever built starring a SI15m diameter and a
¹¹³⁷ 29 m length for a total weight of 14 kT. A thick 4 T solenoid magnet located at the beam interaction
¹¹³⁸ point hosts trackers and calorimeters. Extending in all directions around the magnet, heavy iron
¹¹³⁹ return yokes are installed to extend the magnetic field and support a muon system. The apparatus
¹¹⁴⁰ consists of a barrel, referring to the magnet and the detectors contained in it and the part of the muon
¹¹⁴¹ system built directly in the cylinder around the magnet, and of 2 endcaps in the forward and back-
¹¹⁴² ward region of the detector that closes the apparatus and complete the detection coverage along the
¹¹⁴³ beam line. A front view on the barrel is provided in Figure 2.8 while a detailed view of the apparatus
¹¹⁴⁴ is given in Figure 2.9.

¹¹⁴⁵

¹¹⁴⁶ In order to efficiently detect all long leaving particles and measure their properties with good
¹¹⁴⁷ precision, the CMS detector uses an onion like layout around of the interaction point in order to
¹¹⁴⁸ maximize the covered solid angle. As detailed in Figure 2.10, in the innermost region of the detector,
¹¹⁴⁹ closest to the interaction point, the silicon tracker records the trajectory of charged particles. Around
¹¹⁵⁰ it, the electromagnetic calorimeter (ECAL) stops and measure the energy deposition of electrons
¹¹⁵¹ and photons. In the next layer, the hadron calorimeter (HCAL), hadrons are stopped and their energy
¹¹⁵² measured. These layers are contained inside of the magnet of CMS, the superconducting solenoid.
¹¹⁵³ Outside of the magnet are the muon chambers embedded into iron return yokes used to control the

1154 magnetic field and gives muons, the only particles traveling completely through the whole detector, a
 1155 double bending helping in reconstructing their energy and trajectory. Note that photons and neutral
 1156 hadrons are differentiated from electrons and charged hadrons in the calorimeters by the fact that
 1157 don't interact with the silicon tracker and that they are not influenced by the magnetic field.

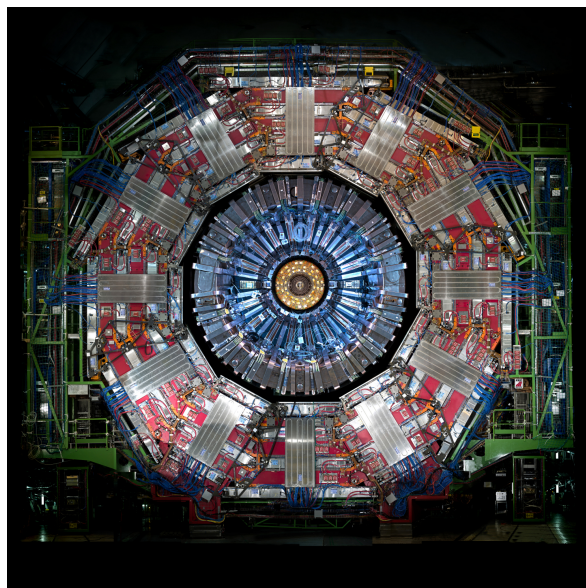


Figure 2.8: Picture of the CMS barrel. The red outer layer is the muon system hosted into the red iron return yokes. The calorimeters are the blue cylinder inside in magnet solenoid and the tracker is the inner yellow cylinder built around the beam pipe.

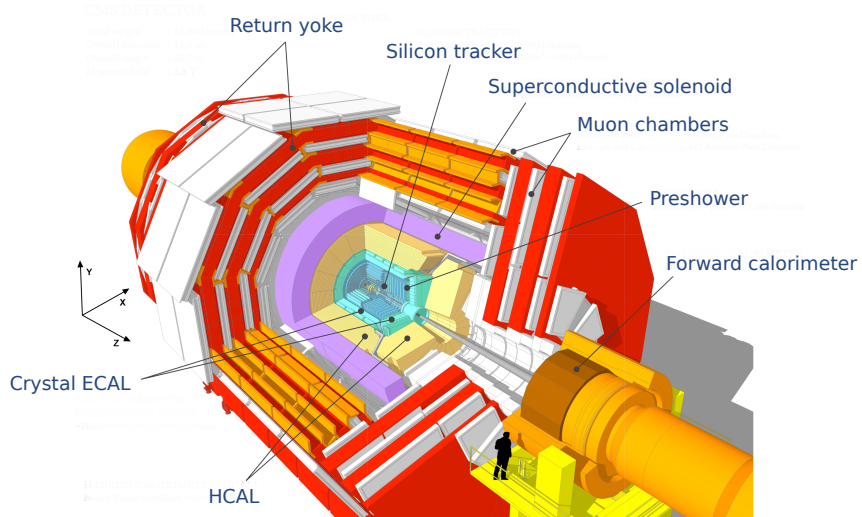


Figure 2.9: View of the CMS apparatus and of its different components.

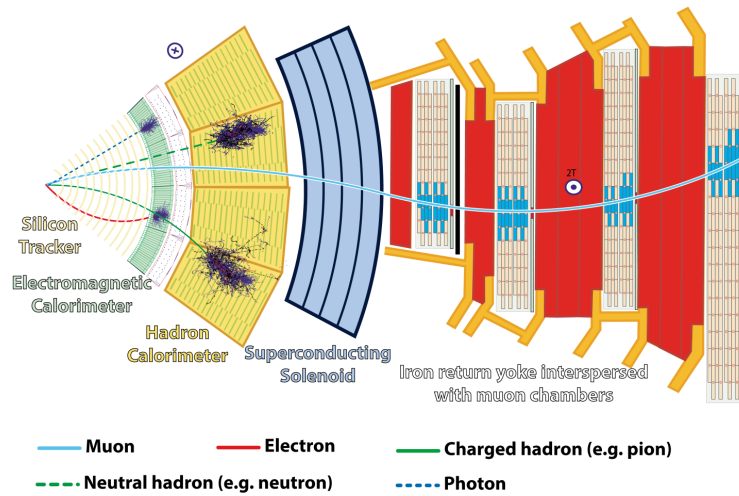


Figure 2.10: Slice showing CMS sub-detectors and how particles interact with them.

2.2.2.1 The silicon tracker, core of CMS

The silicon tracker visible on Figure 2.11 is divided into 2 different sub-systems: the *pixel detector* at the very core and the *microstrip detector* around it. This system is composed of 75 million individual readout channels with up to 6000 channels per squared centimeter for the pixels making it the world's biggest silicon detector. This density allows for measurements of the particle tracks with a precision of the order of $10\ \mu\text{m}$. This is necessary to reconstruct all the different interaction vertices with precision and have a precise measure of the curvature of the charged particles traveling through the magnetic field to estimate their charge and momentum.

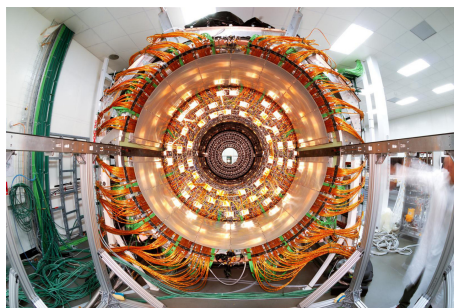


Figure 2.11: CMS tracker.

2.2.2.2 The calorimeters, measurement of particle's energy

The ECAL directly surrounding the tracker is composed of crystals of lead tungstate, PbWO_4 , a very dense but optically transparent material used to stop high energy electrons and photons. These crystal blocks basically are extremely dense scintillators which scintillate in fast, short light bursts proportionally to the energy deposition. The light is yielded rapidly and contained at 80% in the corresponding 25 ns lasting bunch crossing. Each crystal is isolated from the other by the carbon fiber matrix they are embedded in. It is composed of a barrel containing more than 60,000 crystals

1173 and of closing endcaps containing another 15,000 crystals. In front of the ECAL endcap is installed
 1174 a preshower detector made out of two layers of lead and silicon strip detectors to increase the spatial
 1175 resolution close to the beam line for pion-photon and single-double photon discrimination purposes.
 1176 Figure 2.12 shows the calorimeter inside of the magnet and the crystals.

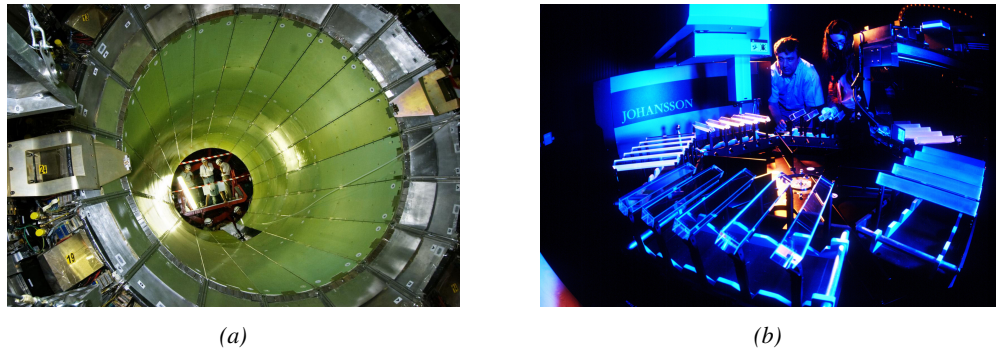


Figure 2.12: Figure 2.12a: picture of the ECAL. Figure 2.12b: picture of the lead tungstate crystals composing the ECAL.

1177 The next layer is the HCAL measuring the hadrons momentum and providing indirect hints of
 1178 non interacting neutral particles, such as neutrinos, as missing transverse momentum. Several layers
 1179 of brass or steel are interleaved with plastic scintillators readout by photodiodes using wavelength-
 1180 shifting fibers. The HCAL is also composed of a barrel, showed in Figure 2.13 and of endcaps. It
 1181 also features forward calorimeters on both sides of CMS in the region very close to the beam line at
 1182 high pseudorapidity ($3.0 < |\eta| < 5.0$). The role of these forward calorimeters, made using steel and
 1183 quartz fibers, is to measure very energetic hadrons.



Figure 2.13: CMS hadron calorimeter barrel.

1184 Finally, in the outer region of the apparatus, a muon system is used to trigger on potentially
 1185 interesting event by identifying muons. Indeed, the muon system is a very important part of the
 1186 CMS trigger infrastructure designed to efficiently select data from the enormous data flow received
 1187 by the detectors as the LHC delivers collisions at a rate of 40 MHz with a pile-ip of 20 to 30 collisions
 1188 per bunch crossing during Phase-I and up to 200 during Phase-II, representing billions of interactions
 1189 per second among which a large quantity are low energy collisions that are not likely to produce new
 1190 reactions, and which is physically impossible for nowadays technologies to cope with. Working at
 1191 a maximum rate of 100 kHz, the trigger system is able to select the 100,000 more interesting events

1192 by looking at the energy distribution of the interaction products and clear signatures like muons
 1193 reconstructed by the muon system. the vast majority of these events will not finally be stored after
 1194 physics tests are applied.

1195 **2.2.2.3 The muon system, corner stone of CMS**

1196 The challenge for the muon system is to provide a robust and fast measurement of muons. Three
 1197 different subsystems, and soon 4 after LS2, compose the muon system as showed in Figure 2.14 in
 1198 which a quadrant of the CMS detector focused on muon system. Drift Tube (DT) are found in the
 1199 barrel region covering the low pseudorapidity region where particles transverse momentum is lower
 1200 and Cathode Strip Chamber (CSC) are found in the endcap region covering higher pseudorapidity
 1201 region closer to beam line where particles have a stronger momentum. The redundancy of the system
 1202 is insured by Resistive Plate Chamber (RPC) in both the barrel and endcap region. Nevertheless, the
 1203 region closest to the beam line ($|\eta| > 1.8$) was not equipped with RPCs. This lack of redundancy
 1204 in the high pseudo rapidity region will be solved during LS2, the following Year End Technical
 1205 Stop (YETS) in 2021 and 2022, and LS3 where the necessary services, detectors and Link System,
 1206 that collects the data and synchronizes them, will be installed.

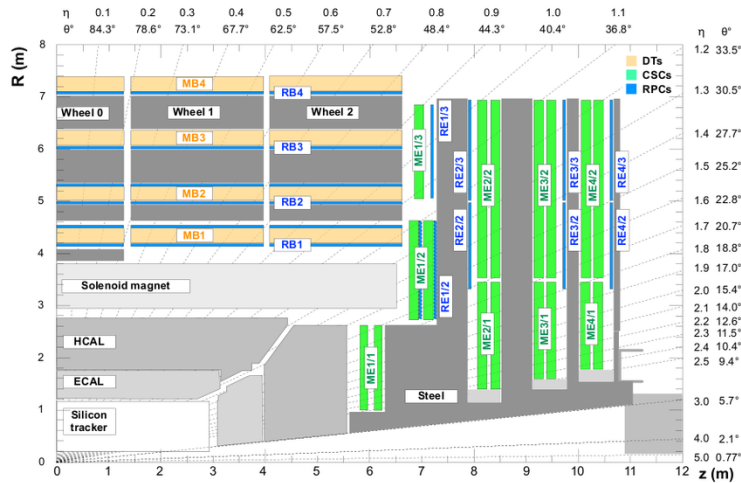


Figure 2.14: A quadrant of the muon system, showing DTs (yellow), RPCs (blue), and CSCs (green).

1207 The barrel region is divided into 5 *wheels* made out of 4 *rings* of detectors with iron return yokes
 1208 in between them whereas the endcaps are made out of 4 disks, each divided into pseudorapidity
 1209 stations, 2 for CSCs (except for the first disk where 3 stations are equipped) and 3 for RPCs, although
 1210 only 2 RPCs stations are equipped at present. The wheels and disks are showed in Figure 2.15. So
 1211 far, each subsystem was dedicated to a particular task. DTs, in the barrel, and CSCs, in the endcaps,
 1212 are used mainly for their spatial resolution. Indeed, DTs' resolution is of the order of 100 μm along
 1213 both the $(r - \phi)$ and $(r - z)$ components while the resolution of CSCs is similar but varies in a range
 1214 from 50 μm to 140 μm depending on the distance to the beamline. On the other hand, RPCs are used
 1215 for their time resolution as they can deliver an information on the muon tracks within 1.5 ns.

1216 The 250 CMS DTs, found in the barrel covering the pseudorapidity region $0 < |\eta| < 1.2$
 1217 and whose structure is shown in Figure 2.16, are composed of 3 *superlayers* of DT cells. Two of
 1218 these superlayers are dedicated to measuring the ϕ coordinate of the muons and while the last one

measures the η (or z) coordinate. Each superlayer consists on 4 layers of 60 to 70 DT cells arranged in quincunx to allow for a precise reconstruction of the muon path through the DT layers. Each DT cell is a rectangular aluminium gas volume with a central anode wire. Cathode strips are placed on the narrow surface of the cells and electrode strips are placed on the wide surface to help shaping the electric field to ensure a consistent drift velocity of electrons in the drift volume. These detectors are operated using a 85/15 mixture of Ar and CO_2 .

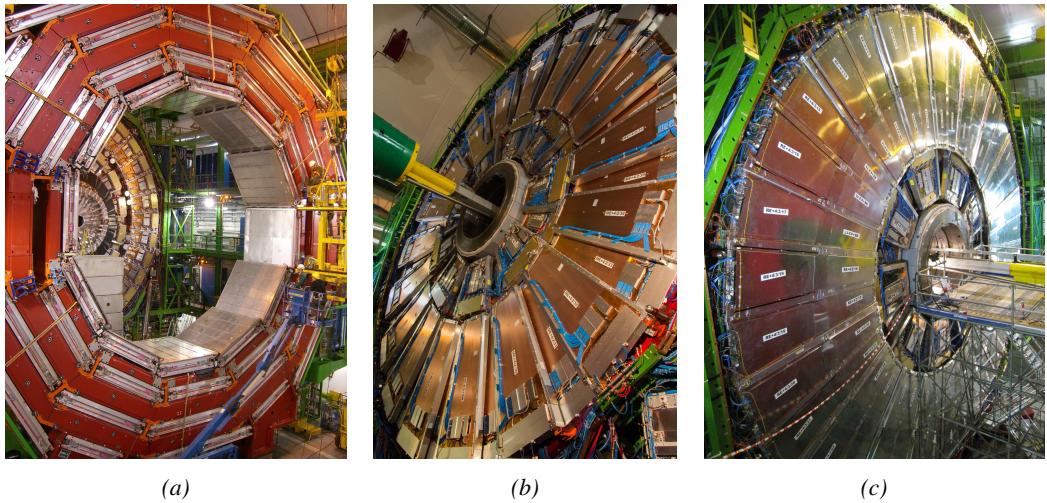


Figure 2.15: Figure 2.15a: Barrel wheel with its detector rings and return yokes. Figure 2.15b: CSC endcap disk with the 2 CSC stations. The outer station is made of 10 deg detectors while the inner station is made of 20 deg detectors. Figure 2.15c: RPC endcap disk. The inner station is not equipped and the inner CSC station can be seen.

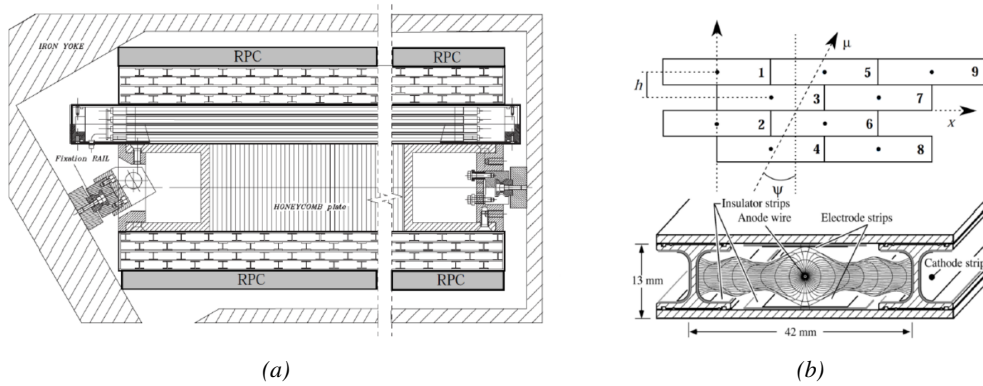


Figure 2.16: Figure 2.16a: Cross section of a DT module showing the two superlayers measuring the ϕ coordinate, perpendicular to the cross section plane, and the superlayer measuring the η coordinate, placed in between the two others with honeycomb and parallel to the cross section plane. The DT detector is sandwiched in between 2 RPCs whose readout strips are perpendicular to the cross section plane, measuring the ϕ coordinate. Figure 2.16b: A DT cell is shown together with its electric field. The path of a muon through a superlayer is shown.

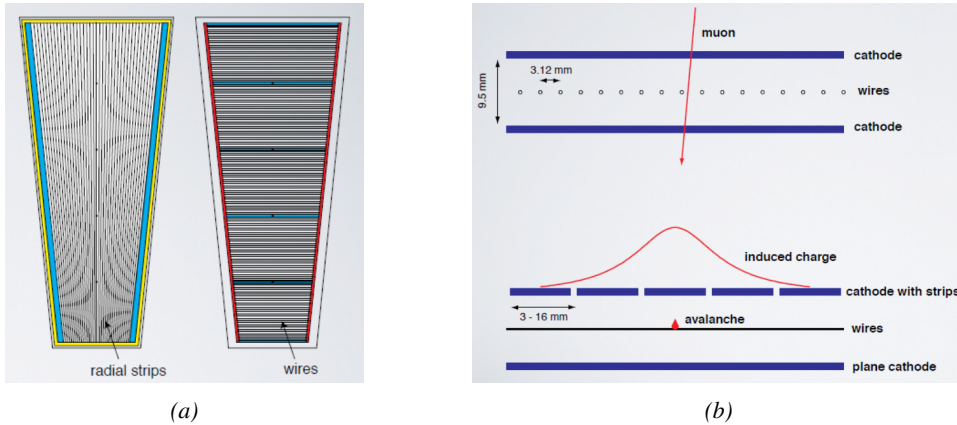


Figure 2.17: Figure 2.17a: cathode strips and anode wire layout of a CSC panel. Figure 2.17b avalanche development and charge collection by anode wires and induction on cathode strips inside of a CSC panel.

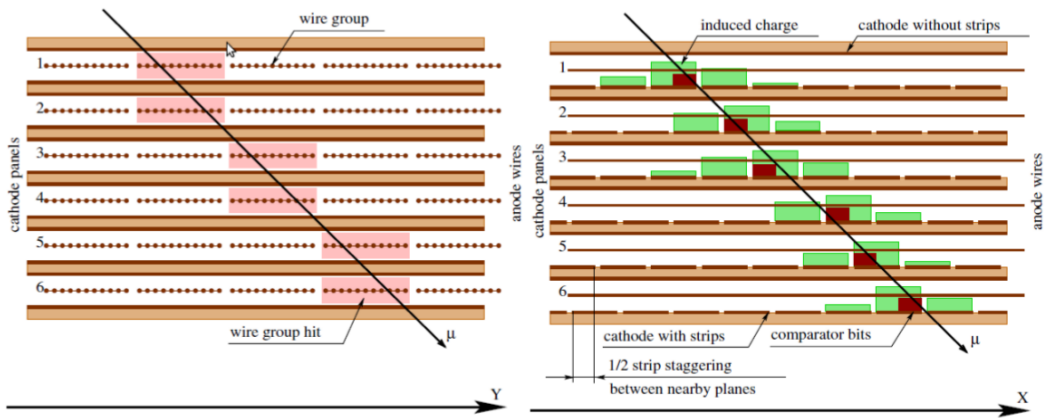


Figure 2.18: Muon track reconstruction through the 6 panels of a CMS CSC using the information of anode wire groups and cathode strip charge distribution combined with comparator bits to decide on which half strip the muon is more likely to have passed.

The 540 CMS CSCs, found in the endcaps covering the pseudorapidity region $0.9 < |\eta| < 2.5$ and described through Figure 2.17, are composed of 6 panels of CSC, each panel consisting in a wide gas volume of 9.5 mm (7 mm in the case of ME1/1 station) containing anode wires and whose surfaces are cathodes. The top cathode is a wide copper plane of the size of the gas volume. The bottom cathode is divided into thin trapezoidal copper strips radially arranged to measure the azimuthal coordinate ϕ with a pitch ranging from 8 to 16 mm. The $0.50 \mu\text{m}$ anode wires are placed perpendicularly to the strips to measure radial coordinate r and are grouped by 10 to 15 with a wire to wire space of 3.2 mm. In the specific case of ME1/1 placed against the HCAL endcap, the $0.30 \mu\text{m}$ anode wires have a wire to wire distance of 2.5 mm and are not disposed perpendicularly to the strips but slightly tilted by an angle of 29 deg to compensate for the lorentz force due to the very strong local magnetic field of 4 T. These detectors are operated with a 40/50/10 mixture of Ar, CO₂ and CF₄. Combining the information of the multiple CSC panels, the detectors achieve a very precise measurement of the muon track.

Despite their excellent spatial resolution, the wire chambers (DTs and CSCs) are limited in terms of time resolution by the fact that the charge needs to drift towards the anode wire and be collected before having the confirmation that a particle was detected as the drift volume is not used to develop avalanches. Indeed, the stronger electric field close to the anode wire triggers the avalanche and the gain of the detector. Due to the drift, the time resolution is thus limited at best to approximately 2 to 3 ns. In addition, even though the intrinsic time resolution of the tracking chambers is rather good compared to the 25 ns in between successive collisions, the processing time of the trigger system doesn't allow for very fast triggering as it provides a time precision of only 12.5 ns. Thus, detectors fully dedicated to timing measurement have been installed as a redundant system. These detectors are RPCs, also gaseous detectors but that use current induction instead of charge collection allowing for a time resolution of the order of 1.5 ns only. Theoretically, depending on the design used, RPCs could reach a time resolution of the order of 10 ps but in the context of LHC where bunch crossing happen every 25 ns, a time resolution of 1.5 ns is sufficient to accurately assign the right bunch crossing to each detected muon.

The 1056 RPCs equipping the CMS muon system both in the barrel and endcap regions and covering the pseudorapidity region $0 < |\eta| < 1.6$ are composed of two layers of RPC *gaps* as described in Figure 2.19. Each gap consists in two resistive electrodes made out of 2 mm thick Bakelite enclosing a 2 mm thick gas volume containing a 95.2/4.5/0.3 mixture of $C_2H_2F_4$, $i - C_4H_{10}$ and SF_6 . Due to this geometry, the electric field inside of a gap is homogeneous and linear at every point in the gas translating into a uniform development of avalanches in the gas volume as soon as a passing muon ionises the gas. The two gaps sandwich a readout copper strip plane. A negative voltage is applied on the outer electrodes, used as cathodes, and the inner electrodes, the anodes, are simply connected to the ground as well as the readout panel that picks up the current induced by the accumulated charge of the growing avalanches in one or both of the gas gaps. This OR system allows for a lower gain (i.e. a lower electric field) on both gaps to reach the maximal efficiency of such a detector.

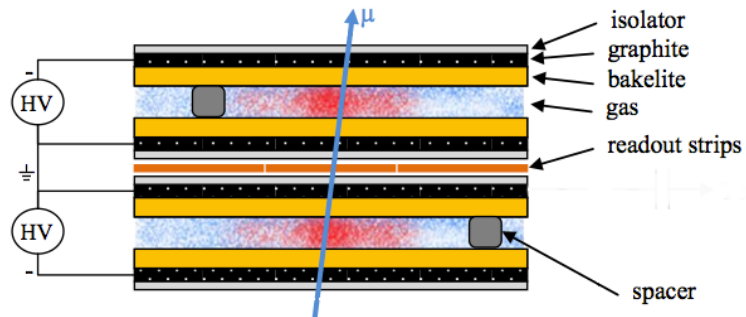


Figure 2.19: Double gap layout of CMS RPCs. Muons passing through the gas volumes will create electron-ion pairs by ionising the gas. this ionisation will immediately translate into a developing avalanche.

3

1264

1265

Muon Phase-II Upgrade

1266 The very first proton beam successfully circulated in the LHC in September 2008 directly followed
1267 by an incident leading to mechanical damage that would delay the LHC program for a year until
1268 November 2009, the very first collisions at a center-of-mass energy of 7 TeV taking place in March
1269 2010. The energy of the beam would be increased after a First Long Shutdown (LS1) starting early
1270 2013 after less than 3 years of data taking. Nevertheless, this first data taking period at only 7 TeV
1271 was sufficient to claim the discovery of a new particle compatible with the Higgs boson in July 2012.
1272 During the 2 years of shutdown, the upgrade of the accelerator allowed for several maintainances
1273 along the beam pipes, repair and consolidation of magnet connection and high-current splices. But
1274 not only the LHC was upgraded. Indeed, the experiments at the 4 collision points also took the
1275 advantage of this time to upgrade their system in prevision of the next LHC run (Run-II) until
1276 2018 and the Second Long Shutdown (LS2) as the luminosity and energy of the beam would be
1277 continuously increasing. By the end of Run-II, the luminosity will have reached twice its nominal
1278 value when the center-of-mass energy has already got close to its nominal value by reaching an
1279 historical 13 TeV for the first time in 2017.

1280 The next long shutdown will occur at the end of this year and will again be the occasion for sim-
1281 ilar maintenance and consolidation in prevision of Run-III and the future upgrade of LS3. Still, the
1282 main occupation of LS2 on LHC side will be the upgrade of LHC injectors. On the experiments side,
1283 LHCb and ALICE will, in a very tight schedule, implement major upgrades while ATLAS and CMS
1284 will wait until LS3 to upgrade their detectors in prevision of high luminosity *LHC-Phase-II*. ALICE
1285 main challenge is an upgrade of their apparatus to cope with the 50 kHz $Pb - Pb$ collisions. Simi-
1286 larly, LHCb will upgrade their frontend readout electronics to cope with the full 40 MHz collisions
1287 delivered by LHC. ATLAS will perform standard maintenance and CMS will focus on the urgent up-
1288 grade of the pixel detector and on the installation of new muon detectors in order to take profit of LS2
1289 time to mitigate the upgrade of detectors foreseen during LS3. Run-III will start in 2021 with the LHC
1290 at its nominal center-of-mass energy and will bring LHC-Phase-I to an end at the end of 2023. By
1291 then the luminosity will only increase to reach 2.5 times the nominal luminosity but during these 3
1292 years of run, the LHC will deliver as much integrated luminosity as what what brought during the al-

most 7 years of both Run-I and II of data taking. Phase-I will end with an overall 300 fb^{-1} delivered.

1294

1295 3.1 High Luminosity LHC

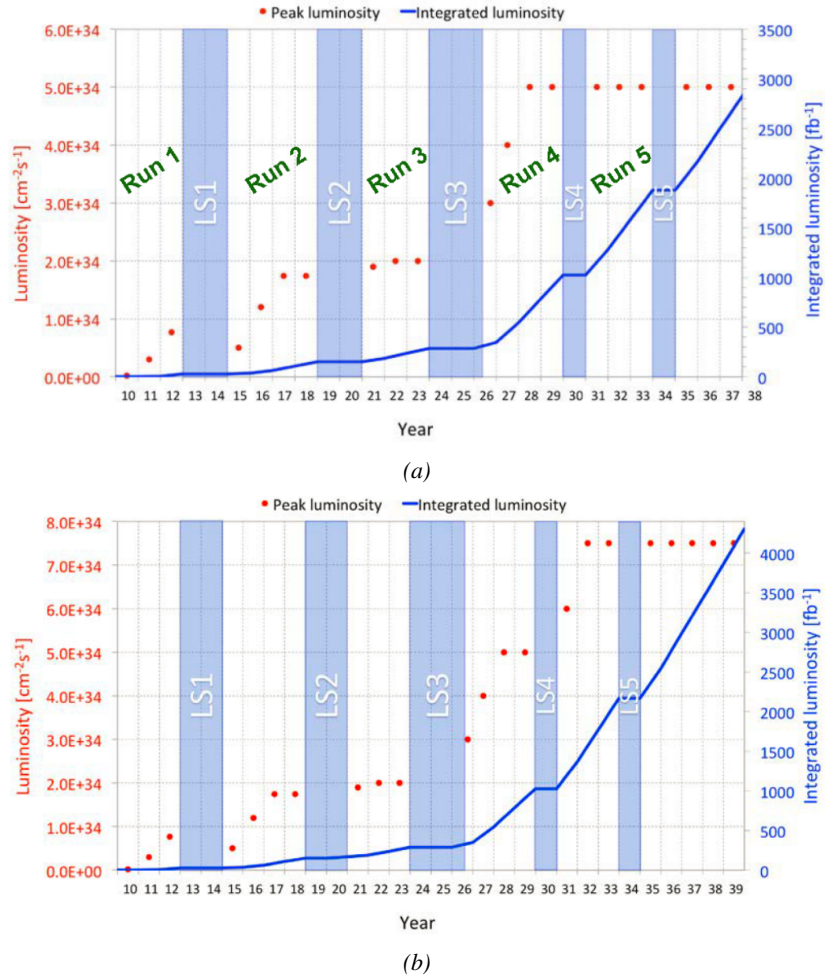


Figure 3.1: Detailed timeline projection of for LHC and HL-LHC operation until 2039 showing the evolution of the instantaneous and integrated luminosity as designed (Figure 3.1a) and in the ultimate case where the instantaneous luminosity is increased to $7.5 \times 10^{34} \text{ cm}^{-2}\text{s}^{-1}$ (Figure 3.1b) [20, 22].

1296 After approximately 15 years of operation, the LHC will undergo a new series of upgrade during
 1297 the LS3 in order to boost its discovery potential as showed in Figure 3.1. This moment onward is
 1298 what is referred to HL-LHC or Phase-II. The goal is to aim for a luminosity 5 to 7 times stronger
 1299 than the nominal one trying to reach even 10 times this value if possible. Increasing the luminosity
 1300 means that the beam size at the collision points needs to be reduced to boost the number of collisions
 1301 per bunch crossing. For this purpose, new focusing and bending magnets, and collimators will be
 1302 installed at the collision points as well as newly developed "crab cavities" that will tilt the particle

1303 bunched just prior to the collisions by giving them transverse momentum and thus increasing their
 1304 meeting area. In addition, the full proton injection line will be upgraded.

1305 Over its full lifetime, the HL-LHC is expected to deliver an outstanding integrated luminosity of
 1306 3000 fb^{-1} leading, in the case of Higgs studies to measuring the couplings of the boson to a precision
 1307 of 2 to 5% thanks to the estimated 15 millions of Higgs created every year providing a more precise
 1308 measurement of potential deviations from the theoretical predictions. SUSY and heavy gauge boson
 1309 studies would also see their mass range limits pushed away by at least 1 TeV and could lead to a new
 1310 breakthrough. SUSY is a particularly important topic as it could give an answer to why the Higgs
 1311 boson can stay so light while coupled to heavy particles by introducing the contributions of the super
 1312 partners on top of providing dark matter candidates. Finally, the increase of luminosity will give the
 1313 possibility to investigate "exotic" mode like for example the models introducing extra dimensions to
 1314 explain the hierarchy problem.

1315 On the experiments side, the pile-up (PU) will be increased up to 150 to 200 interactions per
 1316 bunch crossing in ATLAS and CMS, making necessary an strong upgrade of the trigger system and
 1317 of the inner trackers and of the calorimeters. Both ATLAS and CMS will also need to upgrade
 1318 the muon trigger at the level of the endcaps mainly focusing on the coverage near the beam line in
 1319 order to increase the detection acceptance and event selection. Moreover, the increased luminosity
 1320 will also lead to an increased background rate and a faster ageing of the detectors. This PhD work
 1321 takes place into this very specific context of muon detector consolidation and certification for the
 1322 HL-LHC period in order to provide the CMS experiment with robust new detectors and confirm that
 1323 the present system will survive through the next 20 years of HL-LHC.

1324 3.2 Muon system requirements through HL-LHC

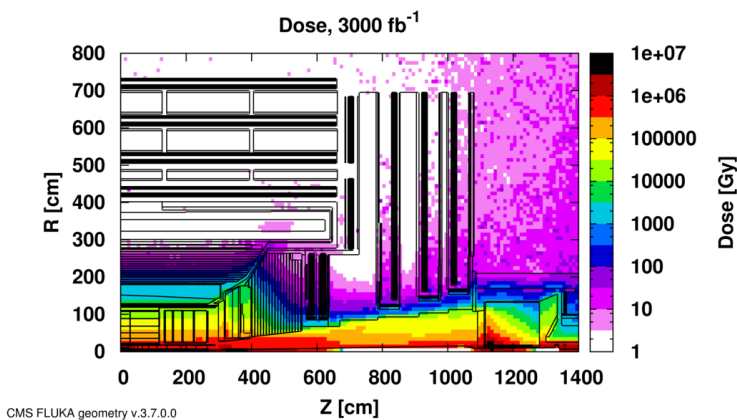


Figure 3.2: Absorbed dose in the CMS cavern after an integrated luminosity of 3000 fb . Using the interaction point as reference, R is the transverse distance from the beamline and Z is the distance along the beamline.

1325 The end of 2018 will mark the beginning of LS2 and the start of Phase-II upgrade activities. From
 1326 the HL-LHC period onwards, i.e. past LS3, the performance degradation due to integrated radiation
 1327 as well as the average number of inelastic collisions per bunch crossing, seen as pile-up into the
 1328 detectors' readout that far exceeds this of the original LHC plans, will rise substantially and become
 1329 a major challenge for all of the LHC experiments, like CMS, that were forced to address an upgrade

program for Phase-II [23]. Dealing with the data from the muon detectors will force to upgrade the detectors and electronics towards the most recent technologies. Simultaneously, this will push new latency requirements onto the Level-1 trigger and the Data Acquisition (DAQ) that will only be fulfilled by upgrading the system with electronics having deeper buffering and faster processing. Simulations of the expected distribution of absorbed dose in the CMS detector under HL-LHC conditions show, in Figure 3.2, that detectors placed close to the beam line will have to withstand high irradiation, the radiation dose being of the order of a few tens of Gy.

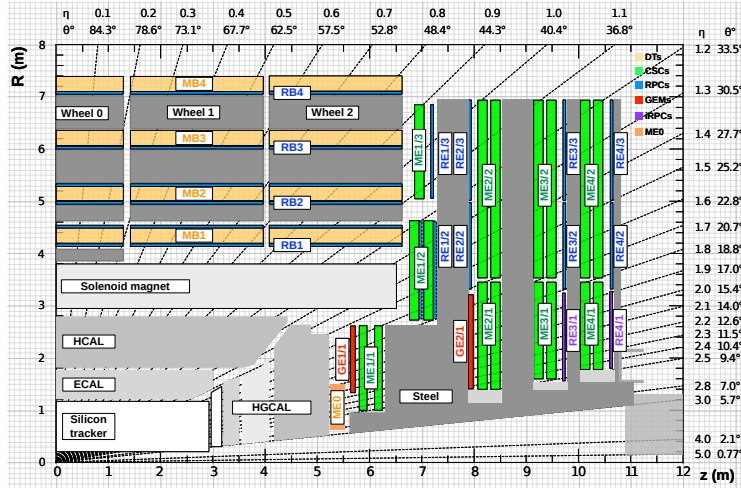


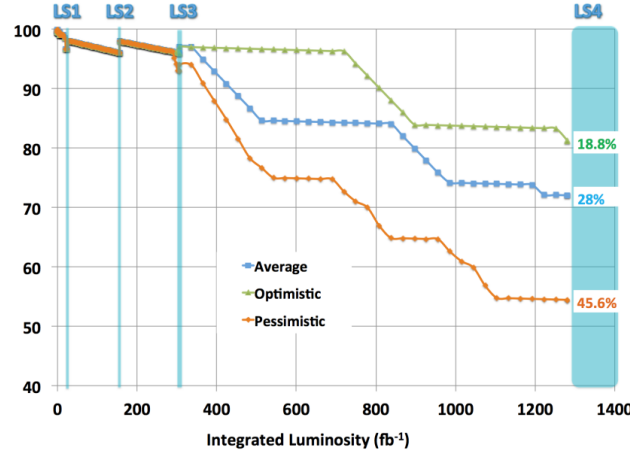
Figure 3.3: A quadrant of the muon system, showing DTs (yellow), RPCs (blue), and CSCs (green). The locations of new forward muon detectors for Phase-II are contained within the dashed box and indicated in red for GEM stations (MEO, GE1/I, and GE2/I) and dark blue for improved RPC (iRPC) stations (RE3/I and RE4/I).

While only the RPCs' electronic system is able to operate under Phase-II requirements, DTs and CSCs will need to improve their trigger accept rate and latency to ensure that Level-1 trigger threshold stays at the same level [24], and DAQ data transfer rate, that respectively need to achieve a minimum of 500 kHz, get down to 12.5 μ s [25], and increase to 1082 Gbit/s DTs and to 1026 Gbit/s for CSCs. As of today, the Level-1 trigger accept rate of DTs doesn't reach 300 kHz while this of CSCs is bellow 250 kHz but the foreseen upgrades are expected to increase the rate way beyond the requirement in the of DTs and up to 4 MHz for CSCs [23].

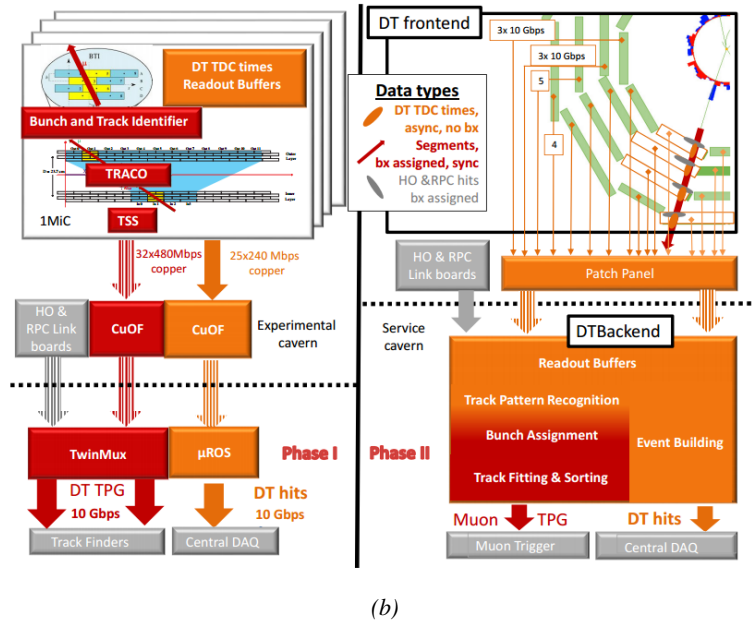
The first version of Minicrate electronics (MiC1) used by DTs don't allow for high enough trigger rate. In addition to this problem, it was showed that these electronics contain components that are not radiation hard enough to sustain HL-LHC conditions and thus, a too large number of channels may fail due to radiations (Figure 3.4). On the other hand, CSCs showed that there electronics would be able to live through the 10 years of Phase-II but the limited buffer depth might cause memory overflows and readout inefficiencies with a fraction of event loss ranging from 5 to 10% depending on the expected background (Figure 3.5). Thus the replacement of CSCs' cathode front-end boards (CFEBs) by digital ones, DCFEBs, with deeper buffer would solve the problem and satisfy HL-LHC requirements. Moreover, a lack of FPGA memory resources is feared for CSCs' anode local charged track boards (ALCTs) and the boards that were not already upgraded during LS1 will need to be replaced, also ensuring that the out bandwidth will be sufficient for the expected high data rate. Finally, all these new DT and CSC electronics will be connected to the trigger electronics

via optical links to ensure a faster communication [23].

1356



(a)



(b)

Figure 3.4: Figure 3.4a: extrapolated fraction of failing channels of the present DT MiC1 electronics as a function of the integrated luminosity. Considering the most optimistic scenario, at least 19% of the channels could have failed by LS4, far before the end of the HL-LHC campaign. Figure 3.4b: Comparison of the current (left) and upgraded (right) DT data processing. So far, the data is sent to service cavern of CMS facility via copper-to-optical-fiber translators (CuOF) by each MiC1. There, data including RPCs and outer hadron calorimeter is combined into trigger primitives (TPG) and transmitted by the TwinMux system to CMS Track Finder. The time-to-digital converter (TDC) data is collected and sent to the CMS data acquisition system (DAQ) by the micro read-out server (μ ROS). After the upgrade, the TDC data will be sent via optical links to a patch panel inside the experimental cavern by each MiC2, and transferred to the back-end, where triggering and event building will be performed.

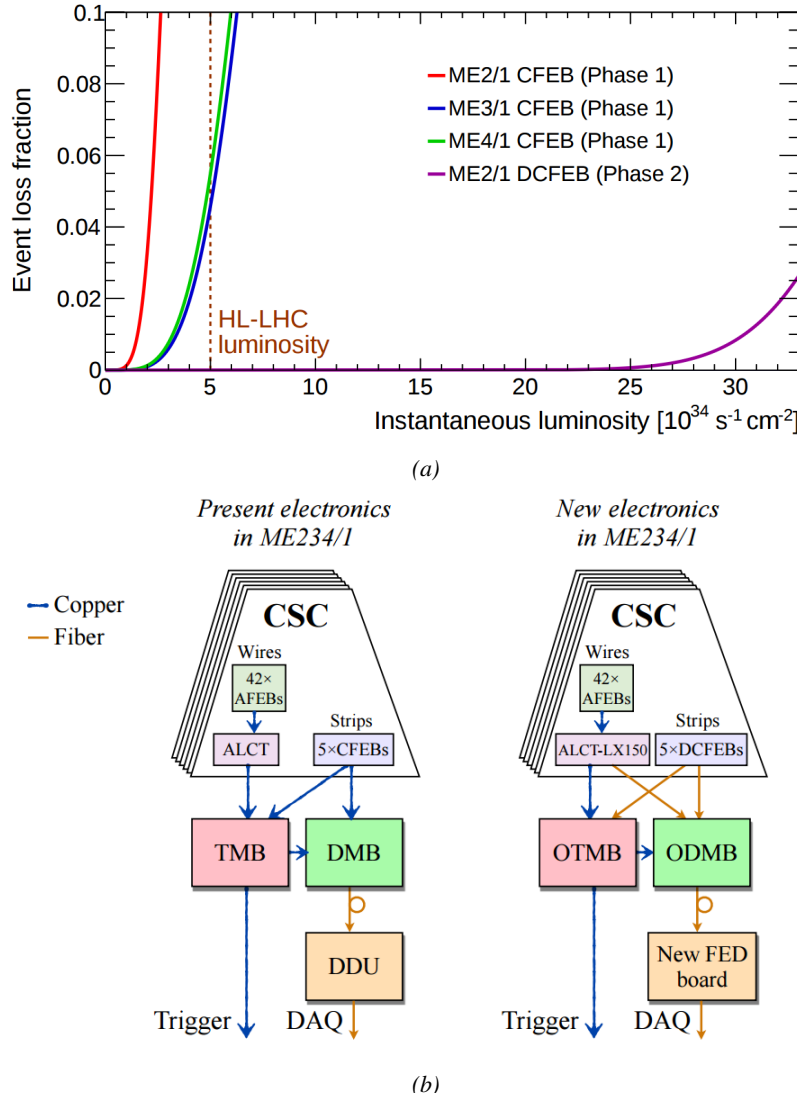


Figure 3.5: Figure 3.5a: The event loss fractions as a function of the instantaneous luminosity is compared for CFEBs (Phase-1) and DCFEBs (Phase-II) at different CSC locations. HL-LHC luminosity is marked with the dashed brown line. Figure 3.5b: Comparison of the current (left) and upgraded (right) CSC data processing. A part of the connections in between ALCTs and DCFEBs, and the trigger mother boards (TMBs) and data acquisition mother boards (DMBs) will be upgraded toward optical data transfer. The detector dependent units (DDUs) used as interface in between CSCs' front-end electronics and the CMS DAQ will be replaced by new FED boards.

The increase of irradiation close to the beam line will affect the background rate seen by the muon detectors in this area and tracking muons will prove to be difficult as this region is not yet equipped with all the detectors that were already foreseen for Phase-I. Improving this situation will come with the increase of hit numbers recorded along the particle track to reduce the ambiguity on muon versus background detection. Moreover, the measurement of small production cross-section and/or decay branching ratio processes, such as the Higgs boson coupling to charge leptons, and in

particular to muons, or the $B_s \rightarrow \mu^+ \mu^-$ decay, is of major interest and specific upgrades in the forward regions of the detector will be required to maximize the physics acceptance to the largest possible solid angle.

To ensure proper trigger performance within the present coverage, the muon system will be completed with new chambers. Figure 3.3 shows the addition of Gas Electron Multiplier (GEM) and improved RPC (iRPC) in the pseudo-rapidity region $1.6 < |\eta| < 2.4$ to complete the redundancy of the already existing CSCs as originally scheduled in the CMS Technical Proposal [26]. A first step into this direction will be taken by installing GEMs on the first endcap disk in position GE1/1 during LS2, during which preparations for the future installation of more GEMs and RPCs will take place by installing the needed services. During the YETS following LS2, iRPCs will be installed on the third and fourth endcap disks in position RE3/1 and RE4/1, and more GEMs will equip the second endcap in position GE2/1 and the inner layer, closest to the HCAL endcap called ME0 during LS3, finally completing the redundant coverage of the muon system and extending it a little by extending the reach to $|\eta| = 2.8$, the redundancy in the region $2.4 < |\eta| < 2.8$ being maintained by the 6 GEM layers contained in each ME0 detector that provide enough tracking points to efficiently reject neutron-induced background.

Nevertheless, the region beyond $|\eta| > 2.8$ and extending to $|\eta| = 5.0$ only is covered by the forward HCAL detectors and lack redundant muon detector coverage. Extensions of the tracker in the context of HL-LHC will increase its coverage up to $|\eta| = 4.0$ but the identification of muons and measurement of their energy with reasonable precision only using the tracker is nearly impossible. Thus, this increased tracker coverage range needs to be put in parallel with a matching muon detector and will open doors to multi-lepton final states in which leptons are likely to have a low transverse momentum and to be found near the beam line.

Finally, as the muon system is composed only of gaseous detectors, strong environmental concerns have risen over the last years as the European directives will restrict the use of fluorine based gas mixtures. Both the CSC and RPC subsystems, using CF_4 , $C_2H_2F_4$, or SF_6 , will need to adapt their working gas in order to strongly reduce the greenhouse potential of the mixtures released into the atmosphere due to gas leaks.

3.3 Forseen upgrades of DTs and CSCs

3.4 New detectors and increased acceptance

RPCs are used by the CMS first level trigger for their good timing performances. Indeed, a very good bunch crossing identification can be obtained with the present CMS RPC system, given their fast response of the order of 1 ns. In order to contribute to the precision of muon momentum measurements, muon chambers should have a spatial resolution less or comparable to the contribution of multiple scattering [21]. Most of the plausible physics is covered only considering muons with $p_T < 100$ GeV thus, in order to match CMS requirements, a spatial resolution of $\mathcal{O}(\text{few mm})$ the proposed new RPC stations, as shown by the simulation in figure 3.6. According to preliminary designs, RE3/1 and RE4/1 readout pitch will be comprised between 3 and 6 mm and 5 η -partitions could be considered.

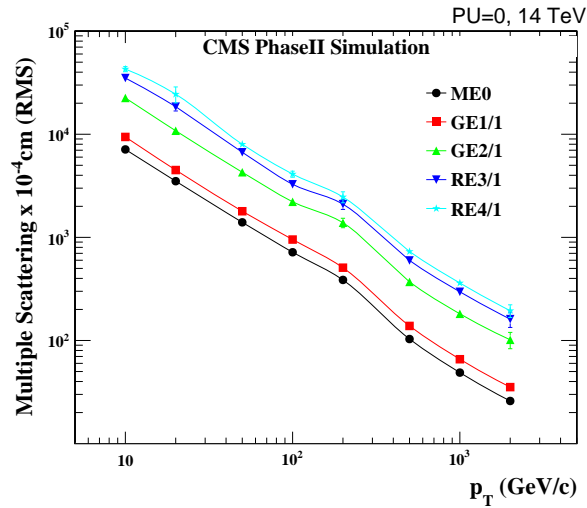


Figure 3.6: RMS of the multiple scattering displacement as a function of muon p_T for the proposed forward muon stations. All of the electromagnetic processes such as bremsstrahlung and magnetic field effect are included in the simulation.

₁₄₀₃ **3.5 Implications of the different upgrades on the Level-1 Trigger**

₁₄₀₄ **3.6 Improvement of physics performance**

4

1405

1406

Physics of Resistive plate chambers

1407 A Resistive Plate Chamber (RPC) is a gaseous detector using the same physical processes described
1408 in Chapter 3. It has been developed in 1981 by Santonico and Cardarelli [27], under the name of
1409 *Resistive Plate Counter*, as an alternative to the local-discharge spark counters proposed in 1978
1410 by Pestov and Fedotovich [28, 29]. Working with spark chambers implied using high-pressure gas
1411 and high mechanical precision which the RPC simplified by formerly using a gas mixture of argon
1412 and butane flowed at atmospheric pressure and a constant and uniform electric field propagated
1413 in between two parallel electrode plates. Moreover, a significant increase in rate capability was
1414 introduced by the use of electrode plate material with high bulk resistivity, preventing the discharge
1415 from growing throughout the whole gas gap. Indeed, the effect of using resistive electrodes is that
1416 the constant electric field is locally canceled out by the development of the discharge, limiting its
1417 growth.

1418 Through its development history, different operating modes [30–32] and new detector designs [33–
1419 35] have been discovered, leading to further improvement of the rate capability of such a detector.
1420 Moreover, the addition of SF_6 into the gas mix improved the stability of operation of the RPC [36,
1421 37].

1422 The low developing costs and easily achievable large detection areas offered by RPCs, as well as
1423 the wide range of possible designs, made them a natural choice to as muon chambers and/or trigger
1424 detectors in multipurpose experiments such as CMS [21] or ATLAS [38], time-of-flight detectors in
1425 ALICE [39], calorimeter with CALICE [40] or even detectors for volcanic muography with ToMu-
1426 Vol [41].

1427 4.1 Principle

1428 RPCs are ionisation detectors composed of two parallel resistive plate electrodes in between which
1429 a constant electric field is set. The space in between the electrodes, referred as *gap*, is filled with a
1430 dense gas that is used to generate primary ionization into the gas volume. The free charge carriers
1431 (electrons and cations) created by the ionization of the gas molecules are then accelerated towards

¹⁴³² the electrodes by the electric field, as shown in Figure 4.1 [42].

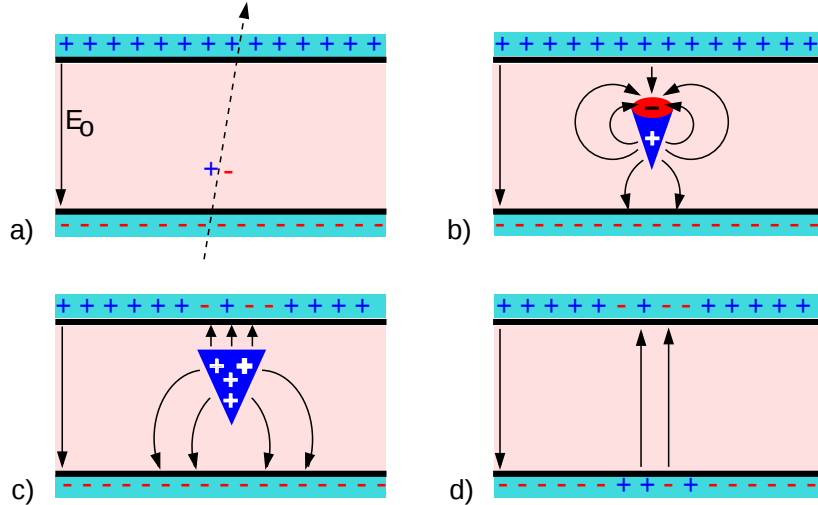


Figure 4.1: Different phases of the avalanche development in the RPC gas volume subjected to a constant electric field E_0 . a) An avalanche is initiated by the primary ionisation caused by the passage of a charged particle through the gas volume. b) Due to its growing size, the avalanche starts to locally influence the electric field. c) The electrons, lighter than the cations reach the anode first. d) The ions reach the cathode. While the charges have not recombined, the electric field in the small region around the avalanche stays affected and locally blind the detector.

¹⁴³³ RPCs being passive detectors, a current on pick-up copper read-out placed outside of the gas
¹⁴³⁴ volume is induced by the charge accumulation during the growth of the avalanche. As a result,
¹⁴³⁵ the time resolution of the detector is substantially increased as the output signal is generated while
¹⁴³⁶ the electrons are still in movement. The advantage of a constant electric field, over multi-wire
¹⁴³⁷ proportional chambers, is that the electrons are being fully accelerated from the moment charge
¹⁴³⁸ carriers are freed and feel the full strength of the electric field that doesn't depend on the distance to
¹⁴³⁹ the readout and that the output signal doesn't need for the electrons to be physically collected.

¹⁴⁴⁰ The typical gas mixture RPCs are operated with is generally composed of 3 gas compounds.

- ¹⁴⁴¹ • Tetrafluoroethane ($C_2F_4H_2$), also referred to as *Freon*, is the principal compound of the RPC
¹⁴⁴² gas mixtures, with a typical fraction above 90%. It is used for it's high effective Townsend
¹⁴⁴³ coefficient and the great average fast charge that allows to operate the detector with a high
¹⁴⁴⁴ threshold with respect to argon, for example, that has similar effective Townsend coefficient
¹⁴⁴⁵ but suffers from a lower fast charge. To operate with similar conditions, argon would require a
¹⁴⁴⁶ higher electric field leading to a higher fraction of streamers, thus limiting the rate capability
¹⁴⁴⁷ of the detector [43].
- ¹⁴⁴⁸ • Isobutane (i- C_4H_{10}), only present in a few percent in the gas mixtures, is used for its UV
¹⁴⁴⁹ quenching properties [44] helping to prevent streamers due to UV photon emission during the
¹⁴⁵⁰ avalanche growth.
- ¹⁴⁵¹ • Sulfur hexafluoride, (SF_6), referred to simply as *SF6*, is used in very little quantities for its
¹⁴⁵² high electronegativity. Excess of electrons are being absorbed by the compound and streamers

1453 are suppressed [37]. Nevertheless, a fraction of SF_6 higher than 1% will not bring any extra
 1454 benefit in terms of streamer cancelation power but will lead to higher operating voltage [36],
 1455 as can be understood through Figure 4.2.

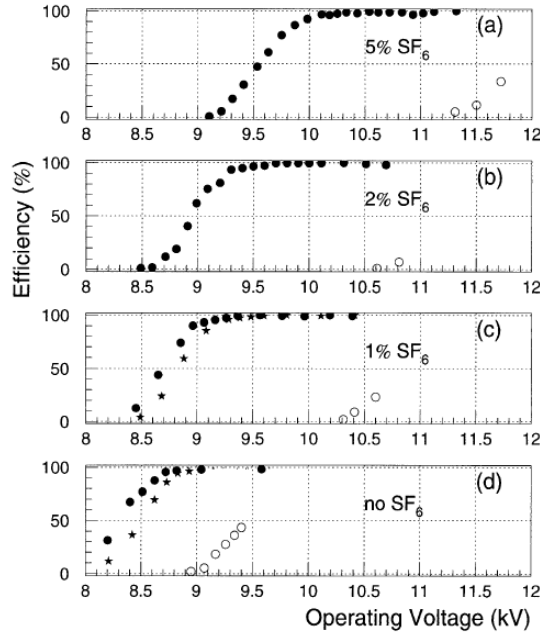


Figure 4.2: Effeciency (circles and stars with 30 mV and 100 mV thresholds respectively) and streamer probability (opened circles) as function of the operating voltatge of a 2 mm single gap HPL RPC flushed with a gas mixture containing (a) 5%, (b) 2%, (c) 1% and (d) no SF_6 [36].

1456 After an avalanche developed in the gas, a time long compared to the development of a discharge
 1457 is needed to recombine the charge carriers in the electrode material due to their resistivity. This
 1458 property has the advantage of affecting the local electric field and avoiding sparks in the detector
 1459 but, on the other hand, the rate capability is intrinsically limited by the time constant τ_{RPC} of the
 1460 detector. Using a quasi-static approximation of Maxwell's equations for weakly conducting media,
 1461 it can be shown that the time constant τ_{RPC} necessary to the charge recombination at the interface
 1462 in between the electrode and the gas volume is given by the Formula 4.1 [45].

$$\tau_{RPC} = \frac{\epsilon_{electrode} + \epsilon_{gas}}{\sigma_{electrode} + \sigma_{gas}} \quad (4.1)$$

1463 A gas can be assimilated to vacuum, leading to $\epsilon_{gas} = \epsilon_0$ and $\sigma_{gas} = 0$, and the electrodes
 1464 permittivity and conductivity can be written as $\epsilon_{electrode} = \epsilon_r \epsilon_0$ and $\sigma_{electrode} = 1/\rho_{electrode}$,
 1465 showing the strong dependence of the time constant to the electrodes resistivity in Formula 4.2.

$$\tau_{RPC} = (\epsilon_r + 1)\epsilon_0 \times \rho_{electrode} \quad (4.2)$$

1466 Very few materials with a low enough resistivity exist in nature. The resistivity targeted to build
 1467 RPCs ranges from 10^9 to $10^{12} \Omega \cdot \text{cm}$. The most common RPC electrode materials are displayed in
 1468 Table 4.1. When the doped glass and ceramics can offer short time constants of the order of 1 ms,

¹⁴⁶⁹ the developing cost of such materials is quite high due to the very low demand. Thus, High-pressure
¹⁴⁷⁰ laminate (HPL) is often the choice for high rate experiments using very large RPC detection areas.
¹⁴⁷¹ Other experiments working at cosmic muon fluxes can safely operate with ordinary float glass.

Material	$\rho_{electrode}$ ($\Omega \cdot \text{cm}$)	ϵ_r	τ_{RPC} (ms)
Float glass	10^{12}	~ 7	~ 700
High-pressure laminate	10^{10} to 10^{12}	~ 6	~ 6 to 600
Doped glass (LR S)	10^9 to 10^{11}	~ 10	~ 1 to 100
Doped ceramics (SiN/SiC)	10^9	~ 8.5	~ 1
Doped ceramics (Ferrite)	10^8 to 10^{12}	~ 20	~ 0.2 to 2000

Table 4.1: Properties of the most used electrode materials for RPCs.

¹⁴⁷² 4.1.1 Electron drift velocity

¹⁴⁷³ Talk about the electron drift velocity and mention the time resolution of RPCs.

¹⁴⁷⁴ 4.2 Rate capability and time resolution of Resistive Plate Chambers

¹⁴⁷⁶ As already previously discussed, the electrode material plays a key role in the max intrinsic rate
¹⁴⁷⁷ capability of RPCs. R&D is being done to develop at always cheaper costs material with lower
¹⁴⁷⁸ resistivity. Nevertheless, the amount of charge released, i.e. the size of the discharge, if reduced
¹⁴⁷⁹ leads to a smaller blind area in the detector, increasing the rate capability of the detector.

¹⁴⁸⁰ 4.2.1 Operation modes

¹⁴⁸¹ RPCs where developed early 1980s. At that time it was using an operating mode now referred to
¹⁴⁸² as *streamer mode*. Streamers are large discharges that develop in between the 2 electrodes enough
¹⁴⁸³ to locally discharge the electrodes. If the electric field inside of the gas volume is strong enough,
¹⁴⁸⁴ with electrons being fast compared to ions, a large and dense cloud of positive ions will develop
¹⁴⁸⁵ nearby the anode and extend toward the cathode while the electrons are being collected, eventually
¹⁴⁸⁶ leading to a streamer discharge due to the increase of field seen at the cathode. the field is then strong
¹⁴⁸⁷ enough so that electrons are pulled out of the cathode. Electrodes, though they are a unique volume
¹⁴⁸⁸ of resistive material, can be assimilated to capacitors. At the moment an electric field is applied in
¹⁴⁸⁹ between their outer surfaces, the charge carriers inside of the volume will start moving leading to
¹⁴⁹⁰ a situation where there is no voltage across the electrodes and a higher density of negative charges,
¹⁴⁹¹ i.e. electrons, on the inner surface of the cathode. Finally, when a streamer discharge occurs, these
¹⁴⁹² electrons are partially released in the gas volume contributing to increase the discharge strength until
¹⁴⁹³ the formation of a conductive plasma, the streamer. This can be understood through Figure 4.3 [30].
¹⁴⁹⁴ Streamer signals are very convenient in terms of read-out as no amplification is required with output
¹⁴⁹⁵ pulses amplitudes of the order of a few tens to few hundreds of mV as can be seen on Figure 4.4.

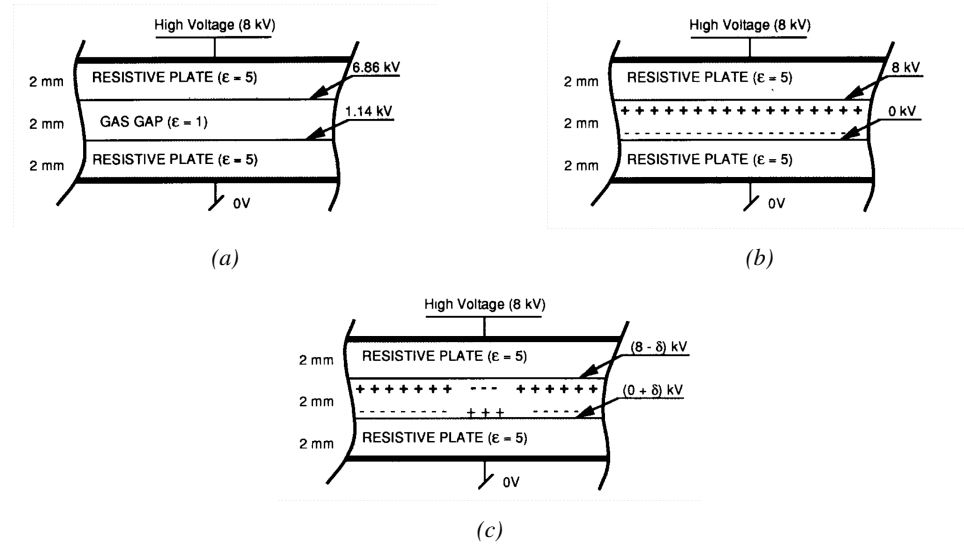


Figure 4.3: Movement of the charge carriers in an RPC. Figure 4.3a: Voltage across an RPC whose electrode have a relative permittivity of 5 at the moment the tension is applied. Figure 4.3b: After the charge carriers moved, the electrodes are charged and there is no voltage drop over the electrodes anymore. The full potential is applied on the gas gap only. Figure 4.3c: The streamer discharge initiated by a charged particle transports electrons and cations towards the anode and cathode respectively.

When the electric field is reduced though, the electronic gain is small until the electrons get close enough to the anode and the positive ion cloud is much smaller. The electric field cannot rise to the point a field emission of electrons on the cathode is possible. The resulting signal is weak, of the order of a few mv as shown on Figure 4.4, and requires amplification. This is the *avalanche mode* of RPC operation.

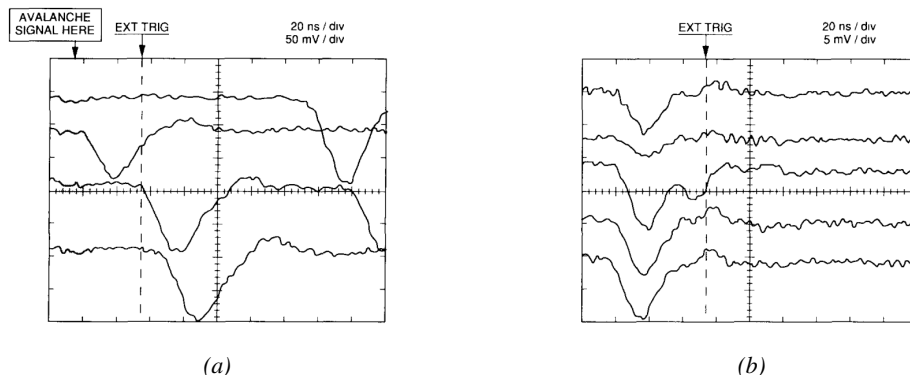


Figure 4.4: Typical oscilloscope pulses in streamer mode (Figure 4.4a) and avalanche mode (Figure 4.4b). In the case of streamer mode, the very small avalanche signal is visible.

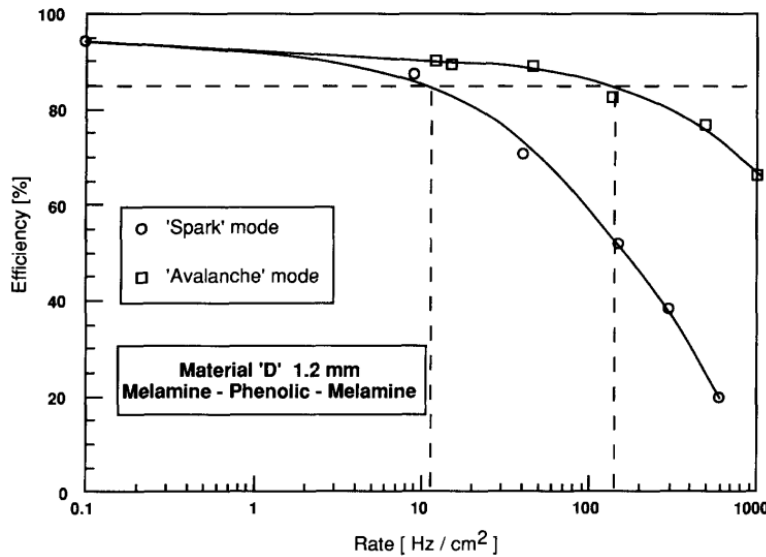


Figure 4.5: Rate capability comparison for the streamer and avalanche mode of operation. An order of magnitude in rate capability for a maximal efficiency drop of 10% is gained by using the avalanche mode over the streamer mode.

This mode offers a higher rate capability by providing smaller discharges that don't affect the electrodes charge and are more locally contained in the gas volume as was demonstrated by Crotty with Figure 4.5 [30]. The detector only stays locally blind the time the charge carriers are recombined and there is no need for electrode recharge which is a long process affecting a large portion of the detector. Another advantage of avalanche signals over streamer is the great time consistency. Figure 4.4 shows very clearly that avalanche signals have a very small time jitter. This is a natural choice for high rate experiments.

4.2.2 Detector designs and performance

Different RPC design have been used and each of them present its own advantages. Historically, the first type of RPC to have been developed is what is referred now to *narrow gap* RPC [27, 46]. After the avalanche mode has been discovered [30], it has been proven that increasing the width of the gas gap lead to higher rate capability, due to lower charge deposition per avalanche, and lower power dissipation [46]. Nevertheless, by increasing the gas gap width, the time resolution of the detector decreases. This is a natural result if the increase of active gas volume in the detector is taken into account. Indeed, for a given threshold, only the small fraction of gas closest to the cathode will provide enough gain to have a detectable signal. In the case of a wider gas volume, the active region is then larger and a larger time jitter is introduced with the variation of starting position of the avalanche, as discussed in [33]. To solve improve both the time resolution and the rate capability, different methods were used trying to get advantages of both narrow and wide gap RPCs.

1520 **4.2.2.1 Double-gap RPC**

1521 Double-gap RPCs are made out of 2 narrow RPC detectors. The 2 RPC gaps are stacked on top of
 1522 each other as shown in Figure 4.6. This detector layout, popularized by the two multipurpose experiments
 1523 CMS [21] and ATLAS [38] at LHC, can be used as an OR system in which each individual
 1524 chamber participates in the output signal. The gain of such a detector is greatly reduced with respect
 1525 to single-gap RPCs with an efficiency plateau reached at lower voltage, as visible on Figure 4.7.

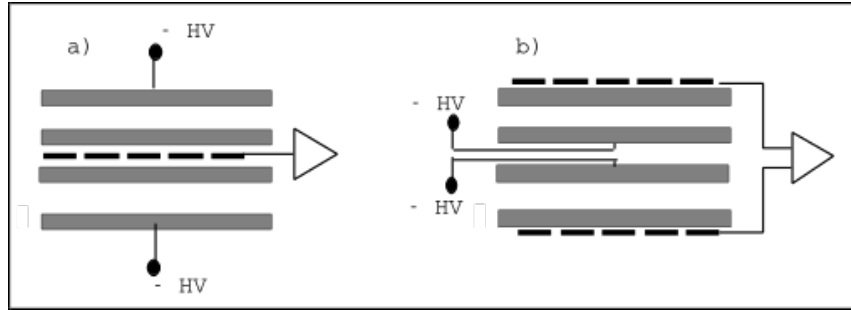


Figure 4.6: Possible double-gap RPC layouts: a) "standard" 1D double-gap RPC, as used in CMS experiment, where the anodes are facing each other and a 1D read-out plane is sandwiched in between them, b) double read-out double-gap RPC as used in ATLAS experiment, where the cathodes are facing each other and 2 read-out planes are used on the outer surfaces. This last layout can offer the possibility to use a 2D reconstruction by using orthogonal read-out planes.

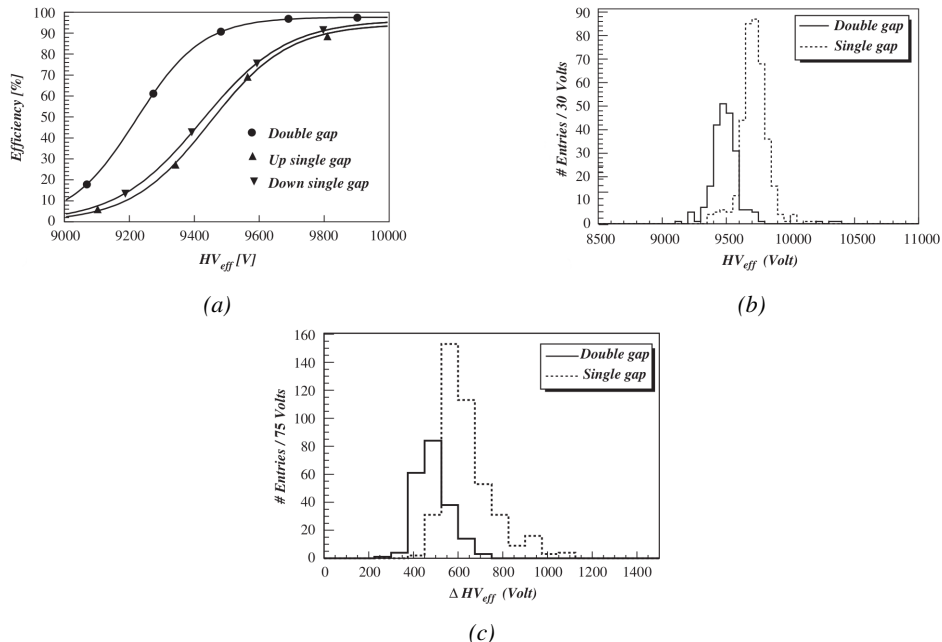


Figure 4.7: Comparison of performance of CMS double and single gap RPCs using cosmic muons [47]. Figure 4.7a: Comparison of efficiency sigmoids. Figure 4.7b: Voltage distribution at 95% of maximum efficiency. Figure 4.7c: $\Delta_{10\%}^{90\%}$ distribution.

4.2.2.2 Multigap RPC (MRPC)

MRPCs are layouts in which floating sub electrode plates are placed into a wide gap RPC to divide the gas volume and create a sum of narrow gaps [33, 34]. The time resolution of such a detector can reach of few tens of ps, with gas gaps of the order of a few hundred μm as shown in Figure 4.8 representing ALICE Time-of-flight (ToF) MRPCs.

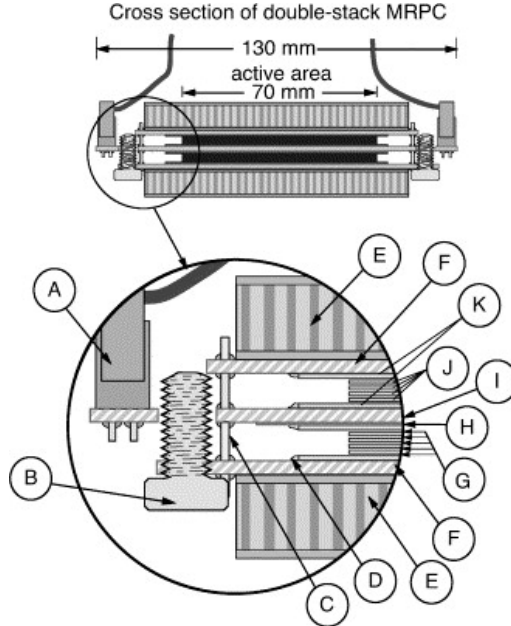


Figure 4.8: Presentation of ALICE MRPC using 250 μm gas gaps, 620 μm outer glass electrodes and 550 μm inner floating electrodes. More details on the labels are given in [48].

Sometimes used as a double multigap RPC, taking advantage of the OR of double gap RPCs, the MRPC is mainly used as ToF detector [48–52] due to its excellent timing properties that allow to perform particle identification as explained by Williams in [53]. The principle of particle identification using ToF is simply the measurement of the velocity of a particle. Indeed, particles are defined by their mass (for the parameter of interest here, their electric charge being measured using the bending angle of the particles traveling through a magnetic field) and this mass can be calculated by measuring the velocity β and momentum of the particle:

$$\beta = \frac{p}{\sqrt{p^2 + m^2}} \quad (4.3)$$

Intuitively, it is trivial to understand that 2 different particles having the same momentum will have a different velocity due to the mass difference and thus a different flight time T_1 and T_2 through the detector and this is used to separate and identify particles. The better the time resolution of the ToF system used, the stronger will the separation be:

$$T = \frac{L}{v} = \frac{L}{c \cdot \beta}, \quad \Delta T = T_1 - T_2 = \frac{L}{c} \left(\sqrt{1 + m_1^2/p^2} - \sqrt{1 + m_2^2/p^2} \right) \cong (m_1^2 - m_2^2) \frac{L}{2cp^2} \quad (4.4)$$

1542 An example of particle identification is given for the case of STAR experiment in Figure 4.9.

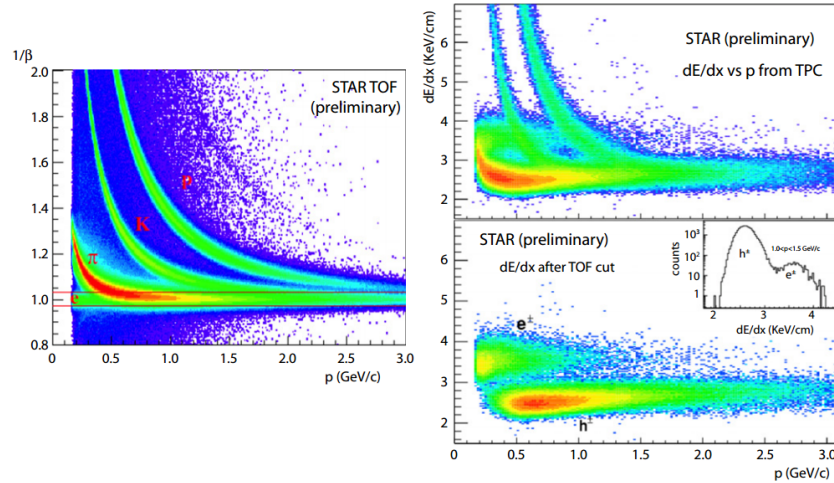


Figure 4.9: Particle identification applied to electrons in the STAR experiment. The identification is performed combining ToF and dE/dx measurements [53].

1543 Another benefice of using such small gas gaps is the strong reduction of the average avalanche
1544 volume and thus of the blind spot on MRPCs leading to an improved rate capability. Multigaps can
1545 sustain backgrounds of several kHz/cm² as demonstrated in Figure 4.10.

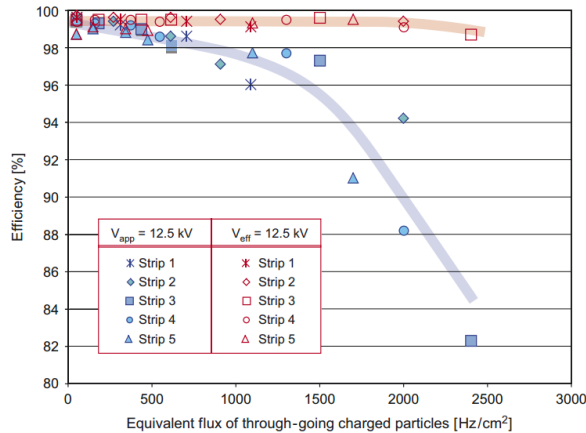


Figure 4.10: Comparison of the detector performance of ALICE ToF MRPC [54] at fixed applied voltage (in blue) and at fixed effective voltage (in red). The effective voltage is kept fixed by increasing the applied voltage accordingly to the current drawn by the detector.

1546 4.2.2.3 Charge distribution and performance limitations

1547 The direct consequence of the different RPC layouts is a variation of intrinsic time resolution of the
1548 RPC as the gap size decreases. An advantage is given to multigaps whose design use sub-millimeter
1549 gas volumes providing very consistent signals.

1550 On the charge spectrum point of view, each layout has its own advantages. When the double-gap
 1551 has the highest induced over drifting charge ratio, as seen in Figure 4.11, the multigap has a charge
 1552 spectrum strongly detached from the origin, as visible in Figure 4.12. A high induced over drifting
 1553 charge ratio means that the double gap can be safely operated at high threshold or that at similar
 1554 threshold it can be operated with a twice smaller drifting charge, meaning a higher rate capability.
 1555 On the other hand, the strong detachment of the charge spectrum from the origin in the MRPC case
 1556 allows to reach a higher efficiency with increasing threshold as most of the induced charge is not low
 1557 due to the convolution of several single gap spectra. The range of stable efficiency increases with
 1558 the number of gap, as presented in Figure 4.13.

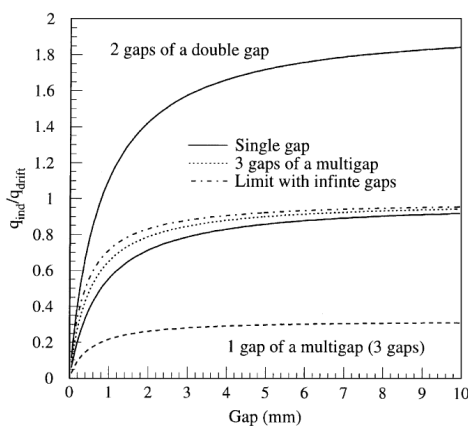


Figure 4.11: Ratio between total induced and drifting charge have been simulated for single gap, double-gap and multigap layouts [55]. The total induced charge for a double-gap RPC is a factor 2 higher than for a multigap.

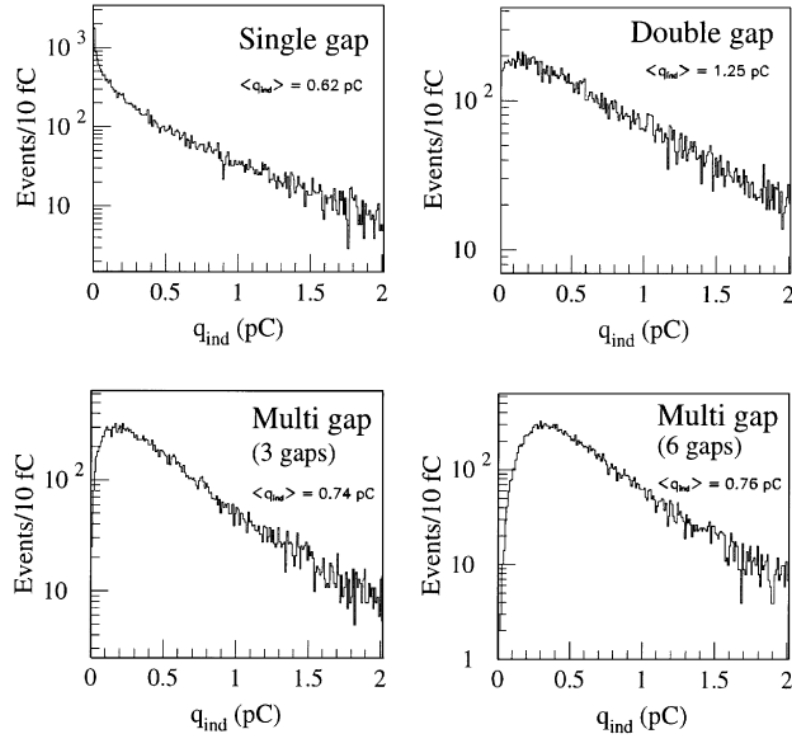


Figure 4.12: Charge spectra have been simulated for single gap, double-gap and multigap layouts [55]. It appears that when single gap shows a decreasing spectrum, double and multigap layouts exhibit a spectrum whose peak is detached from the origin. The detachment gets stronger as the number of gaps increases.

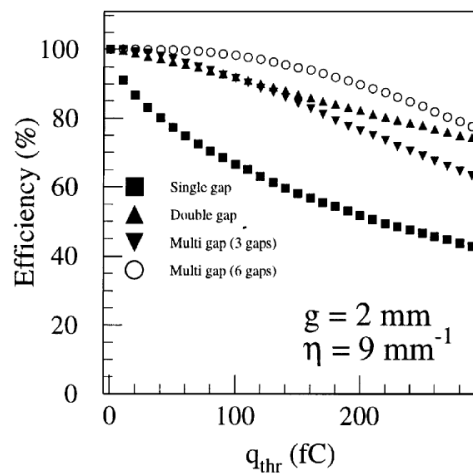


Figure 4.13: The maximal theoretical efficiency is simulated for single gap, double-gap and multigap layouts [55] at a constant gap thickness of 2 mm and using an effective Townsend coefficient of 9 mm^{-1} .

₁₅₅₉ **4.3 Signal formation**

₁₅₆₀ **4.4 Gas transport parameters**

5

1561

1562

1563

Longevity studies and Consolidation of the present CMS RPC subsystem

1564

5.1 Resistive Plate Chambers at CMS

1565

5.1.1 Overview

1566

The Resistive Plate Chambers (RPC) system, located in both barrel and endcap regions, provides a fast, independent muon trigger with a looser p_T threshold over a large portion of the pseudorapidity range ($|\eta| < 1.6$) [add reconstruction].

1568

During High-Luminosity LHC (HL-LHC) operations the expected conditions in terms of background and pile-up will make the identification and correct P_T assignment a challenge for the Muon system. The goal of RPC upgrade is to provide additional hits to the Muon system with precise timing. All these informations will be elaborated by the trigger system in a global way enhancing the performance of the trigger in terms of efficiency and rate control. The RPC Upgrade is based on two projects: an improved Link Board System and the extension of the RPC coverage up to $|\eta| = 2.4$. [FIXME 2.4 or 2.5?]

1570

The Link Board system, that will be described in section xxx, is responsible to process, synchronize and zero-suppress the signals coming from the RPC front end boards. The Link Board components have been produced between 2006 and 2007 and will be subjected to aging and failure in the long term. The upgraded Link Board system will overcome the aging problems described in section xxx and will allow for a more precise timing information to the RPC hits from 25 to 1 ns [ref section xxx].

1572

The extension of the RPC system up to $|\eta| = 2.1$ was already planned in the CMS TDR [ref cmstdr] and staged because of budget limitations and expected background rates higher than the rate capability of the present CMS RPCs in that region. An extensive R&D program has been done in order to develop an improved RPC that fulfills the CMS requirements. Two new RPC layers in the innermost ring of stations 3 and 4 will be added with benefits to the neutron-induced background

1574

1576

1578

1580

1582

1584

1585

1586

1587

1588 reduction and efficiency improvement for both trigger and offline reconstruction.

1589 5.1.2 The present RPC system

1590 The RPC system is organized in 4 stations called RB1 to RB4 in the barrel region, and RE1 to RE4
 1591 in the endcap region. The innermost barrel stations, RB1 and RB2, are instrumented with 2 layers
 1592 of RPCs facing the innermost (RB1in and RB2in) and outermost (RB1out and RB2out) sides of the
 1593 DT chambers. Every chamber is then divided from the read-out point of view into 2 or 3 η partitions
 1594 called “rolls”. The RPC system consist of 480 barrel chambers and 576 endcap chambers. Details
 1595 on the geometry are discussed in the paper [ref to geo paper].

1596 The CMS RPC chamber is a double-gap, operated in avalanche mode to ensure reliable operation
 1597 at high rates. Each RPC gap consists of two 2-mm-thick resistive High-Pressure Laminate (HPL)
 1598 plates separated by a 2-mm-thick gas gap. The outer surface of the HPL plates is coated with a thin
 1599 conductive graphite layer, and a voltage is applied. The RPCs are operated with a 3-component,
 1600 non-flammable gas mixture consisting of 95.2% freon ($C_2H_2F_4$, known as R134a), 4.5% isobutane
 1601 ($i-C_4H_{10}$), and 0.3% sulphur hexafluoride (SF_6) with a relative humidity of 40% - 50%. Readout
 1602 strips are aligned in η between the 2 gas gaps. [\[Add a sentence on FEBs.\]](#)

1603 The discriminated signals coming from the Front End boards feed via twisted cables (10 to 20 m
 1604 long) the Link Board System located in UXC on the balconies around the detector. The Link System
 1605 consist of the 1376 Link Boards (LBs) and the 216 Control Boards (CBs), placed in 108 Link Boxes.
 1606 The Link Box is a custom crate (6U high) with 20 slots (for two CBs and eighteen LBs). The Link
 1607 Box contains custom backplane to which the cables from the chambers are connected, as well as the
 1608 cables providing the LBs and CBs power supply and the cables for the RPC FEBs control with use
 1609 of the I2C protocol (trough the CB). The backplane itself contains only connectors (and no any other
 1610 electronic devices).

1611 The Link Board has 96 input channels (one channel corresponds to one RPC strip). The input
 1612 signals are the ~ 100 ns binary pulses which are synchronous to the RPC hits, but not to the LHC
 1613 clock (which drives the entire CMS electronics). Thus the first step of the FEB signals processing
 1614 is synchronization, i.e. assignment of the signals to the BXes (25 ns periods). Then the data are
 1615 compressed with a simple zero-suppressing algorithm (the input channels are grouped into 8 bit
 1616 partitions, only the partitions with at least one nonzero bit are selected for each BX). Next, the non-
 1617 empty partitions are time-multiplexed i.e. if there are more than one such partition in a given BX,
 1618 they are sent one-by-one in consecutive BXes. The data from 3 neighbouring LBs are concentrated
 1619 by the middle LB which contains the optical transmitter for sending them to the USC over a fiber at
 1620 1.6 Gbps.

1621 The Control Boards provide the communication of the control software with the LBs via the
 1622 FEC/CCU system. The CBs are connected into token rings, each ring consists of 12 CBs of one
 1623 detector tower and a FEC mezzanine board placed on the CCS board located in the VME crate in
 1624 the USC. In total, there are 18 rings in the entire Link System. The CBs also perform automatic
 1625 reloading of the LB's firmware which is needed in order to avoid accumulation of the radiation
 1626 induced SEUs in the LBs firmware.

1627 Both LBs and CB are based on the Xilinx Spartan III FPGAs, the CB additionally contains
 1628 radiation-tolerant (FLASH based) FPGA Actel ProAsicPlus.

1629 The High Voltage power system is located in USC, not exposed to radiation and easily accessible
 1630 for any reparation. A single HV channel powers 2 RPC chambers both in the barrel and endcap
 1631 regions. The Low Voltage boards are located in UXC on the balconies and provide the voltage to the

¹⁶³² front end electronics.

¹⁶³³ 5.1.3 Pulse processing of CMS RPCs

¹⁶³⁴ Signals induced by cosmic particle in the RPC strips are shaped by standard CMS RPC Front-End
¹⁶³⁵ Electronics (FEE) following the scheme of Figure 5.1. On a first stage, analogic signals are amplified
¹⁶³⁶ and then sent to the Constant Fraction Discriminator (CFD) described in Figure 5.2. At the end of
¹⁶³⁷ the chain, 100 ns long pulses are sent in the LVDS output. These output signal are sent on one side to
¹⁶³⁸ a V1190A Time-to-Digital Converter (TDC) module from CAEN and on the other to an OR module
¹⁶³⁹ to count the number of detected signals. Trigger and hit coïncidences are monitored using scalers.
¹⁶⁴⁰ The TDC is used to store the data into ROOT files. These files are thus analysed to understand the
¹⁶⁴¹ detectors performance.

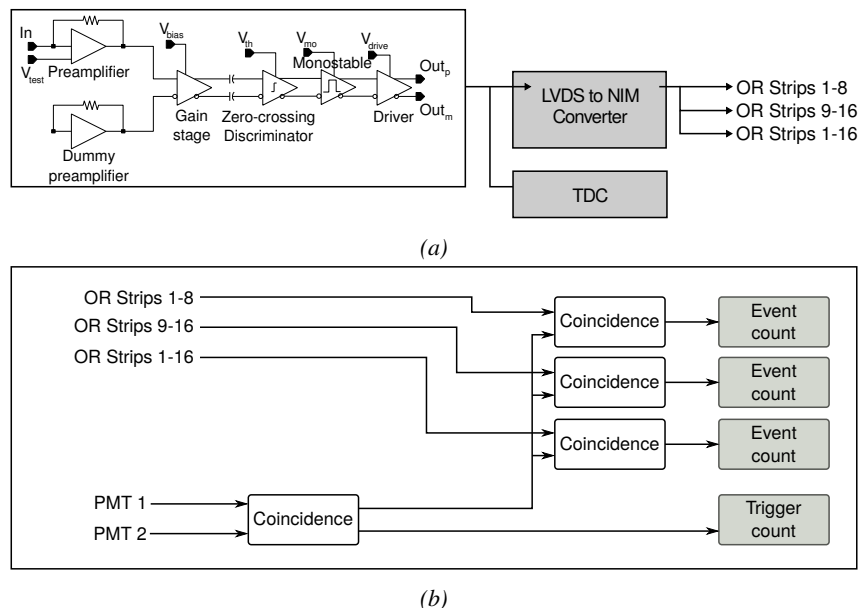


Figure 5.1: Signals from the RPC strips are shaped by the FEE described on Figure 5.1a. Output LVDS signals are then read-out by a TDC module connected to a computer or converted into NIM and sent to scalers. Figure 5.1b describes how these converted signals are put in coincidence with the trigger.

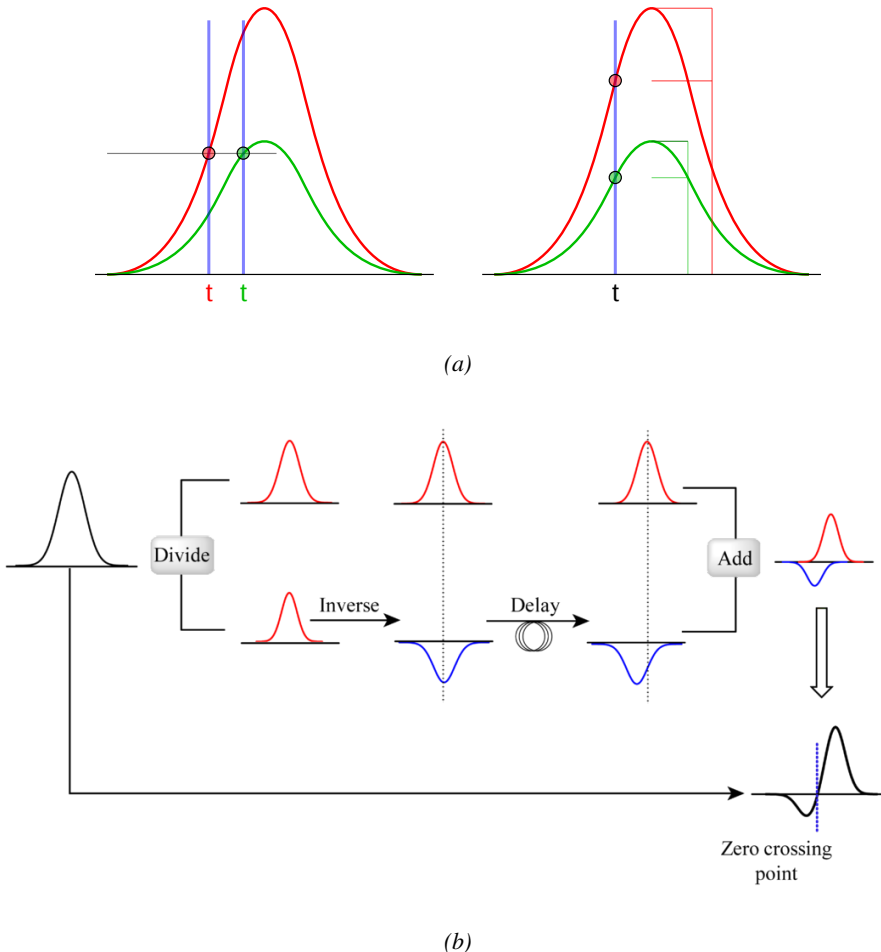


Figure 5.2: Description of the principle of a CFD. A comparison of threshold triggering (left) and constant fraction triggering (right) is shown in Figure 5.2a. Constant fraction triggering is obtained thanks to zero-crossing technique as explained in Figure 5.2b. The signal arriving at the input of the CFD is split into three components. A first one is delayed and connected to the inverting input of a first comparator. A second component is connected to the noninverting input of this first comparator. A third component is connected to the noninverting input of another comparator along with a threshold value connected to the inverting input. Finally, the output of both comparators is fed through an AND gate.

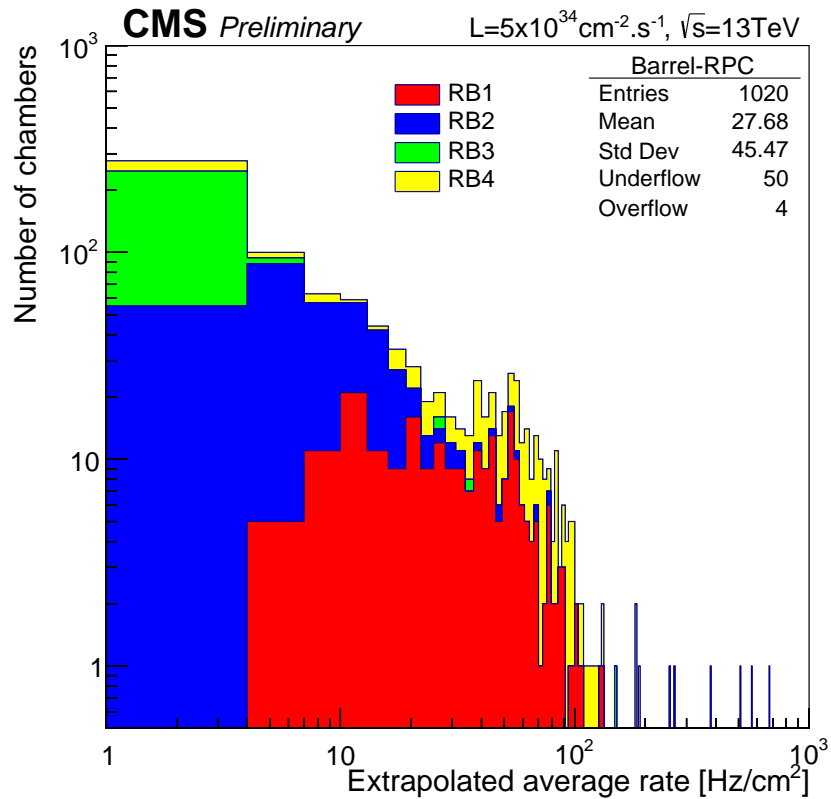
1642 5.2 Testing detectors under extreme conditions

1643 The upgrade from LHC to HL-LHC will increase the peak luminosity from $10^{34} \text{ cm}^{-2} \text{ s}^{-1}$ to reach
 1644 $5 \times 10^{34} \text{ cm}^{-2} \text{ s}^{-1}$, increasing in the same way the total expected background to which the RPC
 1645 system will be subjected to. Composed of low energy gammas and neutrons from $p\text{-}p$ collisions, low
 1646 momentum primary and secondary muons, puch-through hadrons from calorimeters, and particles
 1647 produced in the interaction of the beams with collimators, the background will mostly affect the
 1648 regions of CMS that are the closest to the beam line, i.e. the RPC detectors located in the endcaps.
 1649 [To update.]

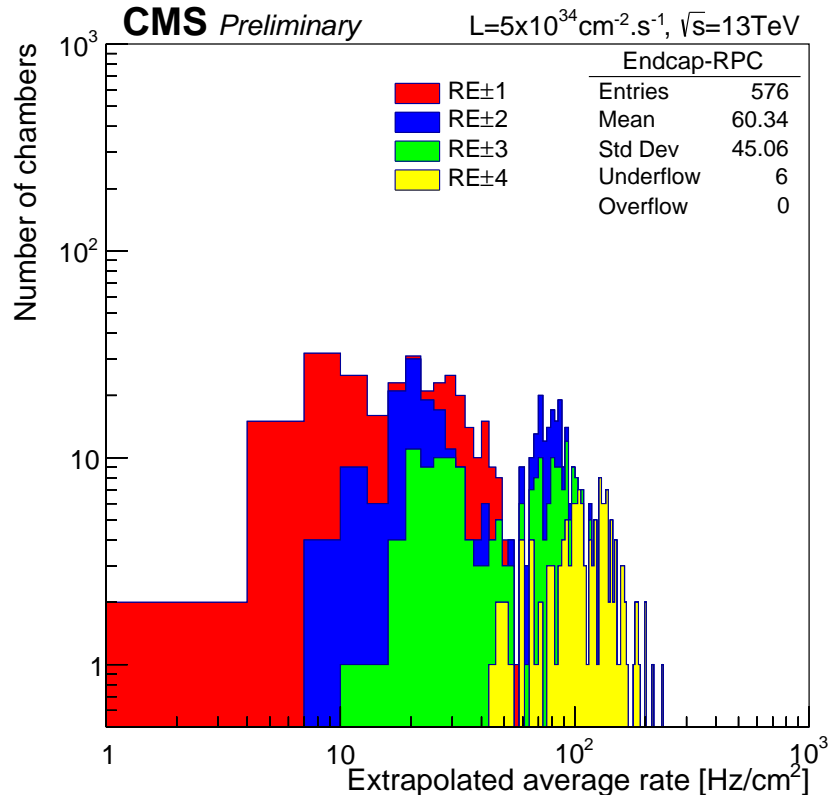
1650

1651 The 2016 data allowed to study the values of the background rate in all RPC system. In Fig-
1652 ure 5.3, the distribution of the chamber background hit rate per unit area is shown at a luminosity
1653 of $5 \times 10^{34} cm^{-2}.s^{-1}$ linearly extrapolating from data collected in 2016 [ref mentioning the linear
1654 dependency of rate vs lumi]. The maximum rate per unit area at HL-LHC conditions is expected to
1655 be of the order of $600 Hz/cm^2$ (including a safety factor 3). Nevertheless, Fluka simulations have
1656 conducted in order to understand the background at HL-LHC conditions. The comparison to the
1657 data has shown, in Figure 5.4, a discrepancy of a factor 2 even though the order of magnitude is
1658 consistent. [Understand mismatch.]

1659



(a)



(b)

Figure 5.3: (5.3a) Extrapolation from 2016 data of single hit rate per unit area in the barrel region. (5.3b) Extrapolation from 2016 data of single hit rate per unit area in the endcap region.

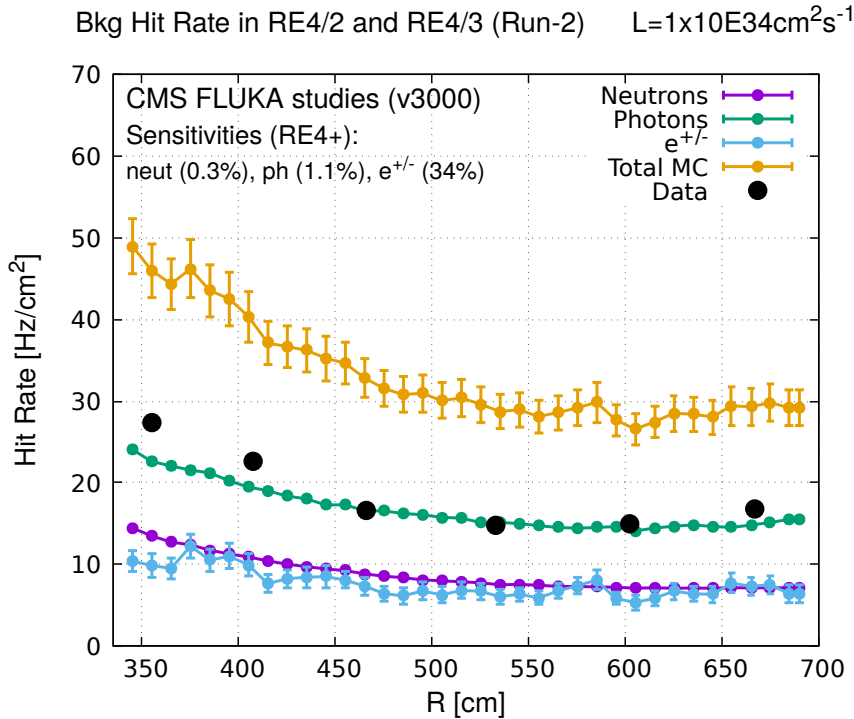


Figure 5.4: Background Fluka simulation compared to 2016 Data at $L = 10^{34} \text{ cm}^{-2} \cdot \text{s}^{-1}$ in the fourth endcap disk region. A mismatch in between simulation and data can be observed. [\[To be understood.\]](#)

In the past, extensive long-term tests were carried out at several gamma and neutron facilities certifying the detector performance. Both full size and small prototype RPCs have been irradiated with photons up to an integrated charge of $\sim 0.05 \text{ C}/\text{cm}^2$ and $\sim 0.4 \text{ C}/\text{cm}^2$, respectively [56, 57]. During Run-I, the RPC system provided stable operation and excellent performance and did not show any aging effects for integrated charge of the order of $0.01 \text{ C}/\text{cm}^2$. Projections on currents from 2016 Data, has allowed to determine that the total integrated charge, by the end of HL-LHC, would be of the order of $1 \text{ C}/\text{cm}^2$ (including a safety factor 3). [\[Corresponding figure needed.\]](#)

1667

1668 5.2.1 The Gamma Irradiation Facilities

1669 5.2.1.1 GIF

1670 Located in the SPS West Area at the downstream end of the X5 test beam, the Gamma Irradiation
 1671 Facility (GIF) was a test area in which particle detectors were exposed to a particle beam in presence
 1672 of an adjustable gamma background [58]. Its goal was to reproduce background conditions these
 1673 detectors would suffer in their operating environment at LHC. GIF layout is shown in Figure 5.5.
 1674 Gamma photons are produced by a strong ^{137}Cs source installed in the upstream part of the zone
 1675 inside a lead container. The source container includes a collimator, designed to irradiate a $6 \times 6 \text{ m}^2$
 1676 area at 5 m maximum to the source. A thin lens-shaped lead filter helps providing with a uniform
 1677 outcoming flux in a vertical plane, orthogonal to the beam direction. The principal collimator hole
 1678 provides a pyramidal aperture of $74^\circ \times 74^\circ$ solid angle and provides a photon flux in a pyramidal vol-

ume along the beam axis. The photon rate is controled by further lead filters allowing the maximum rate to be limited and to vary within a range of four orders of magnitude. Particle detectors under test are then placed within the pyramidal volume in front of the source, perpendicularly to the beam line in order to profit from the homogeneous photon flux. Adjusting the background flux of photons can then be done by using the filters and choosing the position of the detectors with respect to the source.

1684

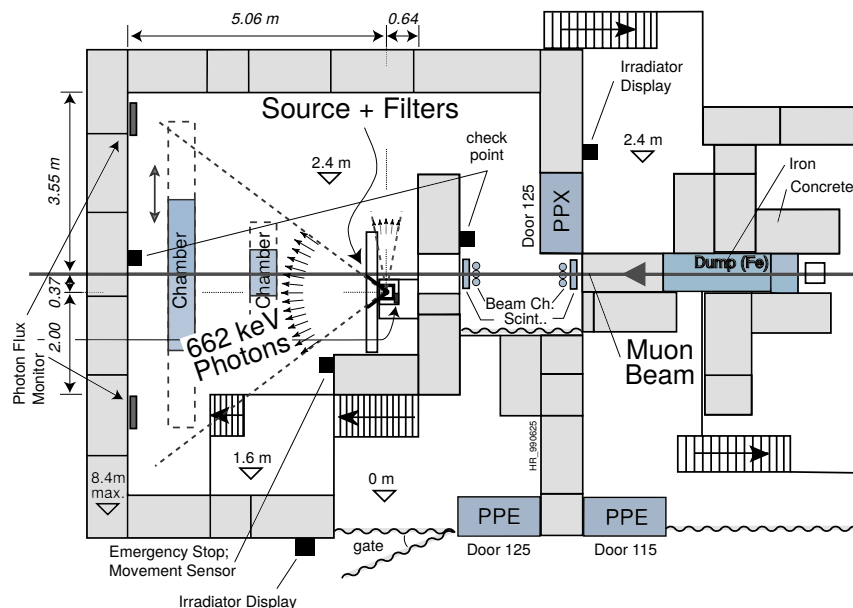


Figure 5.5: Layout of the test beam zone called X5c GIF at CERN. Photons from the radioactive source produce a sustained high rate of random hits over the whole area. The zone is surrounded by 8 m high and 80 cm thick concrete walls. Access is possible through three entry points. Two access doors for personnel and one large gate for material. A crane allows installation of heavy equipment in the area.

As described on Figure 5.6, the ^{137}Cs source emits a 662 keV photon in 85% of the decays. An activity of 740 GBq was measured on the 5th March 1997. To estimate the strength of the flux in 2014, it is necessary to consider the nuclear decay through time assiciated to the Cesium source whose half-life is well known ($t_{1/2} = (30.05 \pm 0.08)$ y). The GIF tests where done in between the 20th and the 31st of August 2014, i.e. at a time $t = (17.47 \pm 0.02)$ y resulting in an attenuation of the activity from 740 GBq in 1997 to 494 GBq in 2014.

1691

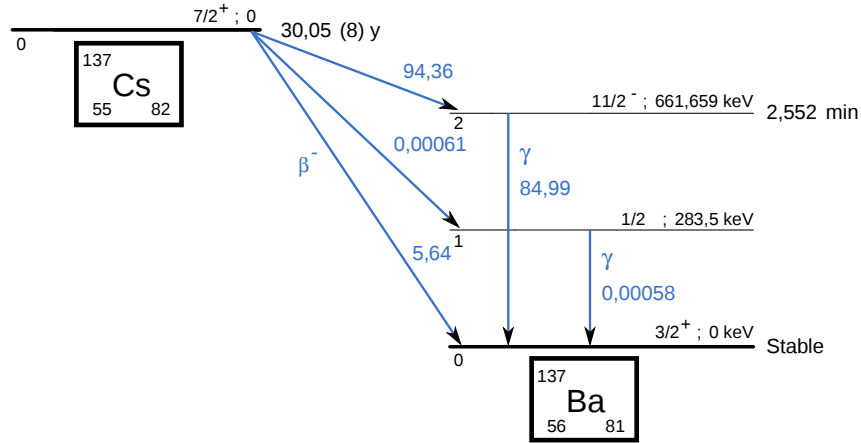


Figure 5.6: ^{137}Cs decays by β^- emission to the ground state of ^{137}Ba ($BR = 5.64\%$) and via the 662 keV isomeric level of ^{137}Ba ($BR = 94.36\%$) whose half-life is 2.55 min.

5.2.1.2 GIF++

The new Gamma Irradiation Facility (GIF++), located in the SPS North Area at the downstream end of the H4 test beam, has replaced its predecessor during LS1 and has been operational since spring 2015 [59]. Like GIF, GIF++ features a ^{137}Cs source of 662 keV gamma photons, their fluence being controlled with a set of filters of various attenuation factors. The source provides two separated large irradiation areas for testing several full-size muon detectors with continuous homogeneous irradiation, as presented in Figure 5.7.

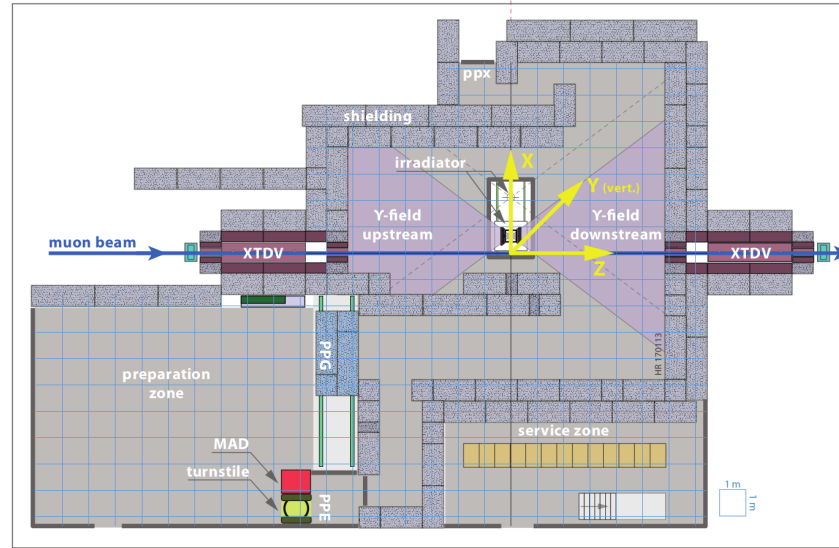


Figure 5.7: Floor plan of the GIF++ facility. When the facility downstream of the GIF++ takes electron beam, a beam pipe is installed along the beam line (z -axis). The irradiator can be displaced laterally (its center moves from $x = 0.65 \text{ m}$ to 2.15 m), to increase the distance to the beam pipe.

1700 The source activity was measured to be about 13.5 TBq in March 2016. The photon flux being
 1701 far greater than HL-LHC expectations, GIF++ provides an excellent facility for accelerated aging
 1702 tests of muon detectors.

1703

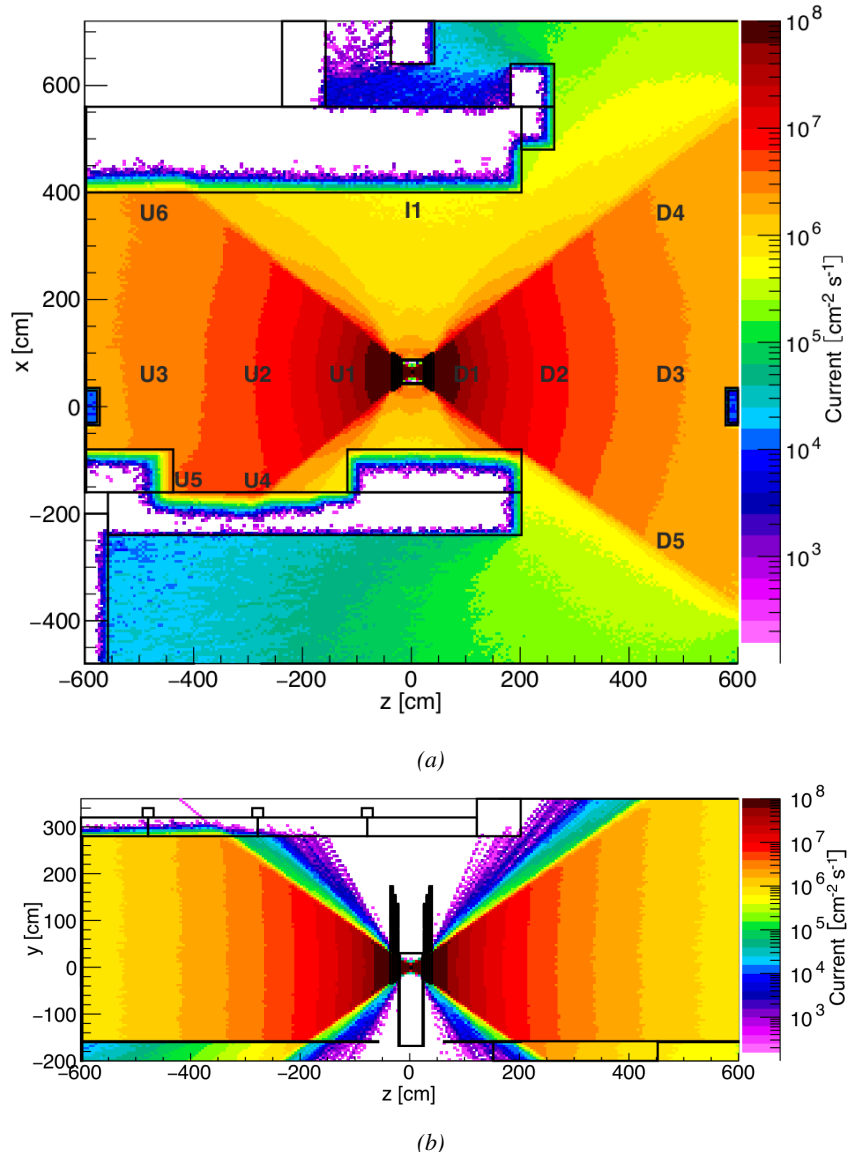


Figure 5.8: Simulated unattenuated current of photons in the xz plane (Figure 5.8a) and yz plane (Figure 5.8b) through the source at $x = 0.65 \text{ m}$ and $y = 0 \text{ m}$. With angular correction filters, the current of 662 keV photons is made uniform in xy planes.

1704 The source is situated in the muon beam line with the muon beam being available a few times a
 1705 year. The H4 beam, composed of muons with a momentum of about 150 GeV/c, passes through the
 1706 GIF++ zone and is used to study the performance of the detectors. Its flux is of 104 particles/ s cm^2

1707 focused in an area similar to $10 \times 10 \text{ cm}^2$. Therefore, with properly adjusted filters, one can imitate
 1708 the HL-LHC background and study the performance of muon detectors with their trigger/readout
 1709 electronics in HL-LHC environment.

1710

1711 5.3 Preliminary tests at GIF

1712 5.3.1 Resistive Plate Chamber test setup

1713 During summer 2014, preliminary tests have been conducted in the GIF area on a newly produced
 1714 RE4/2 chamber labelled RE-4-2-BARC-161. This chamber has been placed into a trolley covered
 1715 with a tent. The position of the RPC inside the tent and of the tent related to the source is described
 1716 in Figure 5.9. To test this CMS RPC, three different absorber settings were used. First of all,
 1717 measurements were done with fully opened source. Then, to complete this preliminary study, the
 1718 gamma flux has been attenuated from a factor 2 and a factor 5. The expected gamma flux at the level
 1719 of our detector will be discussed in subsection ??.

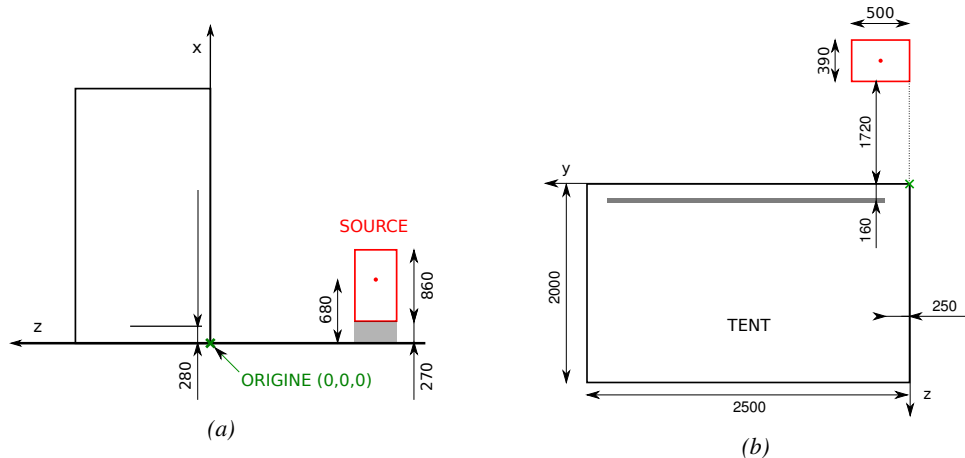


Figure 5.9: Description of the RPC setup. Dimensions are given in mm. A tent containing RPCs is placed at 1720 mm from the source container. The source is situated in the center of the container. RE-4-2-BARC-161 chamber is 160 mm inside the tent. This way, the distance between the source and the chambers plan is 2060 mm. Figure 5.9a provides a side view of the setup in the xz plane while Figure 5.9b shows a top view in the yz plane.



Figure 5.10: RE-4-2-BARC-I61 chamber is inside the tent as described in Figure 5.9. In the top right, the two scintillators used as trigger can be seen. This trigger system has an inclination of 10° relative to horizontal and is placed above half-partition B2 of the RPCs. PMT electronics are shielded thanks to lead blocks placed in order to protect them without stopping photons from going through the scintillators and the chamber.

1720 At the time of the tests, the beam not being operationnal anymore, a trigger composed of 2 plastic
 1721 scintillators has been placed in front of the setup with an inclination of 10 deg with respect to the
 1722 detector plane in order to look at cosmic muons. Using this particular trigger layout, shown on Fig-
 1723 ure 5.10, leads to a cosmic muon hit distribution into the chamber similar to the one in Figure 5.11.
 1724 Measured without gamma irradiation, two peaks can be seen on the profil of partition B, centered
 1725 on strips 52 and 59. Section ?? will help us understand that these two peaks are due respectively to
 1726 forward and backward coming cosmic particles where forward coming particles are first detected by
 1727 the scintillators and then the RPC while the backward coming muons are first detected in the RPC.

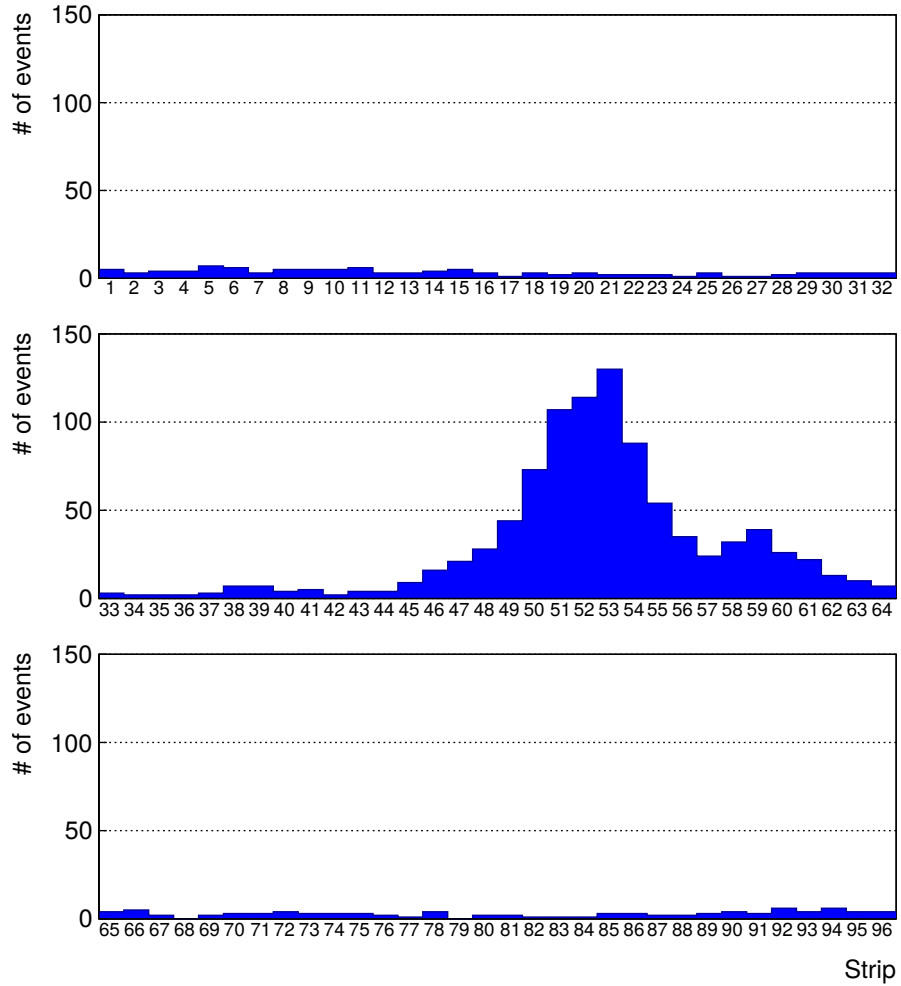


Figure 5.11: Hit distributions over all 3 partitions of RE-4-2-BARC-161 chamber is showed on these plots. Top, middle and bottom figures respectively correspond to partitions A, B, and C. These plots show that some events still occur in other half-partitions than B2, which corresponds to strips 49 to 64, in front of which the trigger is placed, contributing to the inefficiency of detection of cosmic muons. In the case of partitions A and C, the very low amount of data can be interpreted as noise. On the other hand, it is clear that a little portion of muons reach the half-partition B1, corresponding to strips 33 to 48.

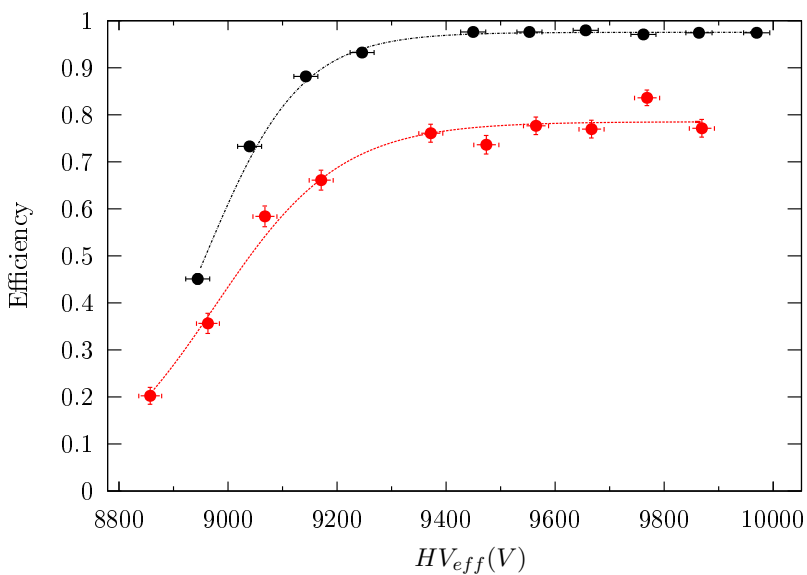
1728 5.3.2 Data Acquisition

1729 5.3.3 Geometrical acceptance of the setup layout to cosmic muons

1730 In order to profit from a constant gamma irradiation, the detectors inside of the GIF bunker need
 1731 to be placed in a plane orthogonal to the beam line. The muon beam that used to be available was
 1732 meant to test the performance of detectors under test. This beam not being active anymore, another
 1733 solution to test detector performance had to be used. Thus, it has been decided to use cosmic muons
 1734 detected through a telescope composed of two scintillators. Lead blocks were used as shielding to

1735 protect the photomultipliers from gammas as can be seen from Figure 5.10.

1736 An inclination has been given to the cosmic telescope to maximize the muon flux. A good com-
 1737 promise had to be found between good enough muon flux and narrow enough hit distribution to
 1738 be sure to contain all the events into only one half partitions as required from the limited available
 1739 readout hardware. Nevertheless, a consequence of the misplaced trigger, that can be seen as a loss
 1740 of events in half-partition B1 in Figure 5.11, is an inefficiency. Nevertheless, the inefficiency of ap-
 1741 proximately 20 % highlighted in Figure 5.12 by comparing the performance of chamber BARC-161
 1742 in 904 and at GIF without irradiation seems too important to be explained only by the geometri-
 1743 cal acceptance of the setup itself. Simulations have been conducted to show how the setup brings
 1744 inefficiency.



1745 *Figure 5.12: Results are derived from data taken on half-partition B2 only. On the 18th of June 2014, data
 1746 has been taken on chamber RE-2-BARC-161 at building 904 (Prevessin Site) with cosmic muons providing us a
 1747 reference efficiency plateau of $(97.54 \pm 0.15)\%$ represented by a black curve. A similar measurement has been
 1748 done at GIF on the 21st of July with the same chamber giving a plateau of $(78.52 \pm 0.94)\%$ represented by a
 1749 red curve.*

1745 5.3.3.1 Description of the simulation layout

1746 The layout of GIF setup has been reproduced and incorporated into a Monte Carlo (MC) simulation
 1747 to study the influence of the disposition of the telescope on the final distribution measured by the
 1748 RPC. A 3D view of the simulated layout is given into Figure 5.13. Muons are generated randomly
 1749 in a horizontal plane located at a height corresponding to the lowest point of the PMTs. This way,
 1750 the needed size of the plane in order to simulate events happening at very big azimuthal angles (i.e.
 1751 $\theta \approx \pi$) can be kept relatively small. The muon flux is designed to follow the usual $\cos^2\theta$ distribution
 1752 for cosmic particle. The goal of the simulation is to look at muons that pass through the muon
 1753 telescope composed of the two scintillators and define their distribution onto the RPC plane. During
 1754 the reconstruction, the RPC plane is then divided into its strips and each muon track is assigned to a
 1755 strip.

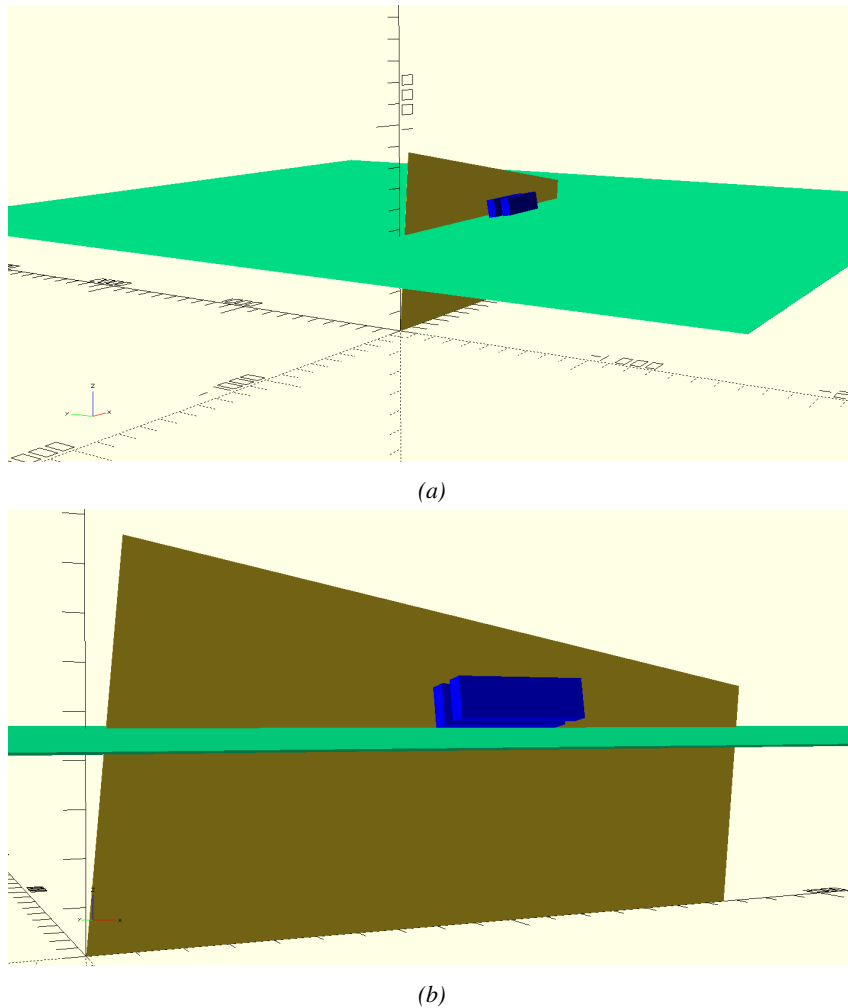


Figure 5.13: Representation of the layout used for the simulations of the test setup. The RPC is represented as a yellow trapezoid while the two scintillators as blue cuboids looking at the sky. A green plane corresponds to the muon generation plane within the simulation. Figure 5.9a shows a global view of the simulated setup. Figure 5.9b shows a zoomed view that allows to see the 2 scintillators as well as the full RPC plane.

1756 In order to further refine the quality of the simulation and understand deeper the results the
 1757 dependance of the distribution has been studied for a range of telescope inclinations. Moreover,
 1758 the threshold applied on the PMT signals has been included into the simulation in the form of a
 1759 cut. In the approximation of uniform scintillators, it has been considered that the threshold can be
 1760 understood as the minimum distance particles need to travel through the scintillating material to give
 1761 a strong enough signal. Particles that travel a distance smaller than the set "threshold" are thus not
 1762 detected by the telescope and cannot trigger the data taking. Finally, the FEE threshold also has
 1763 been considered in a similar way. The mean momentum of horizontal cosmic rays is higher than
 1764 those of vertical ones but the stopping power of matter for momenta ranging from 1 GeV to 1 TeV
 1765 stays comparable. It is then possible to assume that the mean number of primary e^- /ion pairs per
 1766 unit length will stay similar and thus, depending on the applied discriminator threshold, muons with

1767 the shortest path through the gas volume will deposit less charge and induce a smaller signal on the
 1768 pick-up strips that could eventually not be detected. These two thresholds also restrain the overall
 1769 geometrical acceptance of the system.

1770 **5.3.3.2 Simulation procedure**

1771 The simulation software has been designed using C++ and the output data is saved into ROOT
 1772 histograms. Simulations start for a threshold T_{scint} varying in a range from 0 to 45 mm in steps
 1773 of 5 mm, where $T_{scint} = 0$ mm corresponds to the case where there isn't any threshold apply on
 1774 the input signal while $T_{scint} = 45$ mm, which is the scintillator thickness, is the case where muons
 1775 cannot arrive orthogonally onto the scintillator surface. For a given T_{scint} , a set of RPC thresholds
 1776 are considered. The RPC threshold, T_{RPC} varies from 2 mm, the thickness of the gas volume, to
 1777 3 mm in steps of 0.25 mm. For each $(T_{scint}; T_{RPC})$ pair, $N_\mu = 10^8$ muons are randomly generated
 1778 inside the muon plane described in the previous paragraph with an azimuthal angle θ chosen to follow
 1779 a $\cos^2\theta$ distribution.

1780 Planes are associated to each surface of the scintillators. Knowing muon position into the muon
 1781 plane and its direction allows us, by assuming that muons travel in a straight line, to compute the
 1782 intersection of the muon track with these planes. Applying conditions to the limits of the surfaces
 1783 of the scintillator faces then gives us an answer to whether or not the muon passed through the
 1784 scintillators. In the case the muon has indeed passed through the telescope, the path through each
 1785 scintillator is computed and muons whose path was shorter than T_{scint} are rejected and are thus
 1786 considered as having not interacted with the setup.

1787 On the contrary, if the muon is labeled as good, its position within the RPC plane is computed
 1788 and the corresponding strip, determined by geometrical tests in the case the distance through the
 1789 gas volume was enough not to be rejected because of T_{RPC} , gets a hit and several histograms
 1790 are filled in order to keep track of the generation point on the muon plane, the intersection points
 1791 of the reconstructed muons within the telescope, or on the RPC plane, the path traveled through
 1792 each individual scintillator or the gas volume, as well as other histograms. Moreover, muons fill
 1793 different histograms whether they are forward or backward coming muons. They are discriminated
 1794 according to their direction components. When a muon is generated, an (x, y, z) position is assigned
 1795 into the muon plane as well as a $(\theta; \phi)$ pair that gives us the direction it's coming from. This way,
 1796 muons satisfying the condition $0 \leq \phi < \pi$ are designated as backward coming muons while muons
 1797 satisfying $\pi \leq \phi < 2\pi$ as forward coming muons.

1798 This simulation is then repeated for different telescope inclinations ranging in between 4 and 20°
 1799 and varying in steps of 2°. Due to this inclination and to the vertical position of the detector under
 1800 test, the muon distribution reconstructed in the detector plane is asymmetrical. The choice as been
 1801 made to chose a skew distribution formula to fit the data built as the multiplication of gaussian and
 1802 sigmoidal curves together. A typical gaussian formula is given as 5.1 and has three free parameters
 1803 as A_g , its amplitude, \bar{x} , its mean value and σ , its root mean square. Sigmoidal curves as given by
 1804 formula 5.2 are functions converging to 0 and A_s as x diverges. The inflection point is given as x_i
 1805 and λ is proportional to the slope at $x = x_i$. In the limit where $\lambda \rightarrow \infty$, the sigmoid becomes a
 1806 step function.

$$g(x) = A_g e^{-\frac{(x-\bar{x})^2}{2\sigma^2}} \quad (5.1)$$

$$s(x) = \frac{A_s}{1 + e^{-\lambda(x-x_i)}} \quad (5.2)$$

¹⁸⁰⁷ Finally, a possible representation of a skew distribution is given by formula 5.3 and is the product
¹⁸⁰⁸ of 5.1 and 5.2. Naturally, here $A_{sk} = A_g \times A_s$ and represents the theoretical maximum in the limit
¹⁸⁰⁹ where the skew tends to a gaussian function.

$$sk(x) = g(x) \times s(x) = A_{sk} \frac{e^{\frac{-(x-\bar{x})^2}{2\sigma^2}}}{1 + e^{-\lambda(x-x_i)}} \quad (5.3)$$

¹⁸¹⁰ 5.3.3.3 Results

¹⁸¹¹ Influence of T_{scint} on the muon distribution

¹⁸¹² Influence of T_{RPC} on the muon distribution

¹⁸¹³ Influence of the telescope inclination on the muon distribution

¹⁸¹⁴ Comparison to data taken at GIF without irradiation

¹⁸¹⁵ 5.3.4 Photon flux at GIF

¹⁸¹⁶ 5.3.4.1 Expectations from simulations

¹⁸¹⁷ In order to understand and evaluate the γ flux in the GIF area, simulations had been conducted in
¹⁸¹⁸ 1999 and published by S. Agosteo et al [58]. Table 5.1 presented in this article gives us the γ flux
¹⁸¹⁹ for different distances D to the source. This simulation was done using GEANT and a Monte Carlo
¹⁸²⁰ N-Particle (MCNP) transport code, and the flux F is given in number of γ per unit area and unit time
¹⁸²¹ along with the estimated error from these packages expressed in %.

Nominal ABS	Photon flux F [$s^{-1}cm^{-2}$]			
	at $D = 50$ cm	at $D = 155$ cm	at $D = 300$ cm	at $D = 400$ cm
1	$0.12 \cdot 10^8 \pm 0.2\%$	$0.14 \cdot 10^7 \pm 0.5\%$	$0.45 \cdot 10^6 \pm 0.5\%$	$0.28 \cdot 10^6 \pm 0.5\%$
2	$0.68 \cdot 10^7 \pm 0.3\%$	$0.80 \cdot 10^6 \pm 0.8\%$	$0.25 \cdot 10^6 \pm 0.8\%$	$0.16 \cdot 10^6 \pm 0.6\%$
5	$0.31 \cdot 10^7 \pm 0.4\%$	$0.36 \cdot 10^6 \pm 1.2\%$	$0.11 \cdot 10^6 \pm 1.2\%$	$0.70 \cdot 10^5 \pm 0.9\%$

Table 5.1: Total photon flux ($E\gamma \leq 662$ keV) with statistical error predicted considering a ^{137}Cs activity of 740 GBq at different values of the distance D to the source along the x -axis of irradiation field [58].

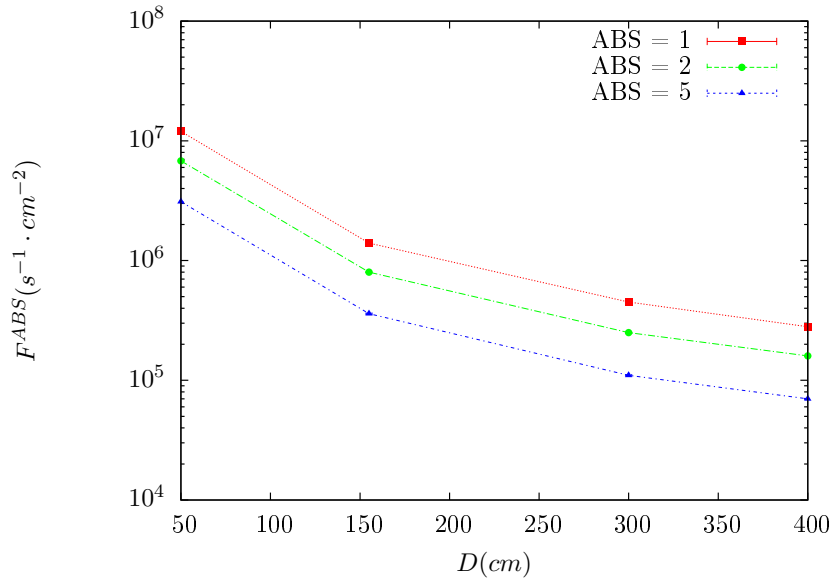


Figure 5.14: γ flux $F(D)$ is plot using values from table 5.1. As expected, the plot shows similar attenuation behaviours with increasing distance for each absorption factors.

The simulation doesn't directly provides us with an estimated flux at the level of our RPC. First of all, it is needed to extract the value of the flux from the available data contained in the original paper and then to estimate the flux in 2014 at the time the experimentation took place. Figure 5.14 that contains the data from Table 5.1. In the case of a pointlike source emitting isotropic and homogeneous gamma radiations, the gamma flux F at a distance D to the source with respect to a reference point situated at D_0 where a known flux F_0 is measured will be expressed like in Equation 5.4, assuming that the flux decreases as $1/D^2$, where c is a fitting factor.

$$F^{ABS} = F_0^{ABS} \times \left(\frac{cD_0}{D} \right)^2 \quad (5.4)$$

By rewriting Equation 5.4, it comes that :

$$c = \frac{D}{D_0} \sqrt{\frac{F^{ABS}}{F_0^{ABS}}} \quad (5.5)$$

$$\Delta c = \frac{c}{2} \left(\frac{\Delta F^{ABS}}{F^{ABS}} + \frac{\Delta F_0^{ABS}}{F_0^{ABS}} \right) \quad (5.6)$$

Finally, using Equation 5.5 and the data in Table 5.1 with $D_0 = 50$ cm as reference point, we can build Table 5.2. It is interesting to note that c for each value of D doesn't depend on the absorption factor.

Nominal ABS	Correction factor c		
	at $D = 155$ cm	at $D = 300$ cm	at $D = 400$ cm
1	$1.059 \pm 0.70\%$	$1.162 \pm 0.70\%$	$1.222 \pm 0.70\%$
2	$1.063 \pm 1.10\%$	$1.150 \pm 1.10\%$	$1.227 \pm 0.90\%$
5	$1.056 \pm 1.60\%$	$1.130 \pm 1.60\%$	$1.202 \pm 1.30\%$

Table 5.2: Correction factor c is computed thanks to formulae 5.5 taking as reference $D_0 = 50$ cm and the associated flux F_0^{ABS} for each absorption factor available in table 5.1.

1833 For the range of D/D_0 values available, it is possible to use a simple linear fit to get the evolution
 1834 of c . The linear fit will then use only 2 free parameters, a and b , as written in Equation 5.7. This gives
 1835 us the results showed in Figure 5.15. Figure 5.15b confirms that using only a linear fit to extract c is
 1836 enough as the evolution of the rate that can be obtained superimposes well on the simulation points.

$$c \left(\frac{D}{D_0} \right) = a \frac{D}{D_0} + b \quad (5.7)$$

$$F^{ABS} = F_0^{ABS} \left(a + \frac{bD_0}{D} \right)^2 \quad (5.8)$$

$$\Delta F^{ABS} = F^{ABS} \left[\frac{\Delta F_0^{ABS}}{F_0^{ABS}} + 2 \frac{\Delta a + \Delta b \frac{D_0}{D}}{a + \frac{bD_0}{D}} \right] \quad (5.9)$$

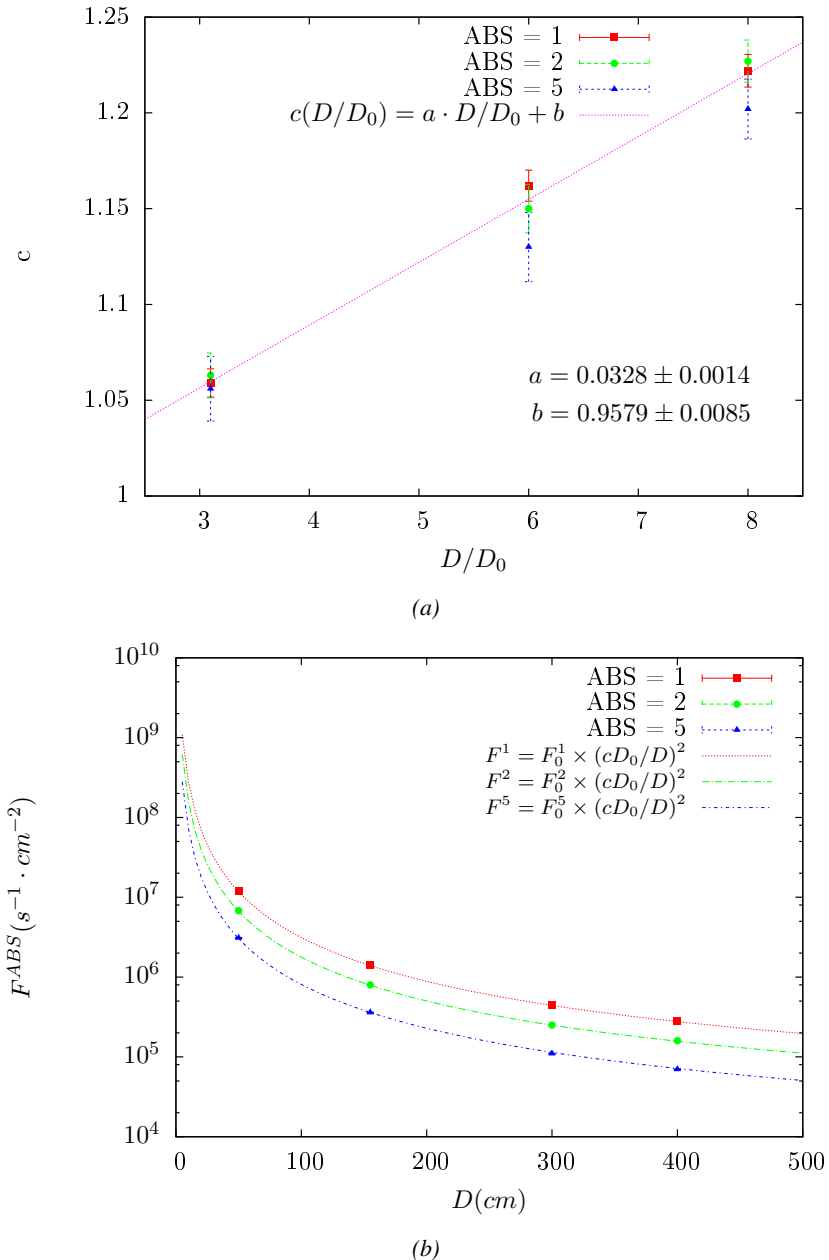


Figure 5.15: Figure 5.15a shows the linear approximation fit done via formulae 5.7 on data from table 5.2. Figure 5.15b shows a comparison of this model with the simulated flux using a and b given in figure 5.15a in formulae 5.4 and the reference value $D_0 = 50\text{cm}$ and the associated flux for each absorption factor F_0^{ABS} from table 5.1

In the case of the 2014 GIF tests, the RPC plane is located at a distance $D = 206\text{ cm}$ to the source.
 Moreover, to estimate the strength of the flux in 2014, it is necessary to consider the nuclear decay through time associated to the Cesium source whose half-life is well known ($t_{1/2} = (30.05 \pm 0.08)\text{ y}$).
 The very first source activity measurement has been done on the 5th of March 1997 while the GIF

1841 tests where done in between the 20th and the 31st of August 2014, i.e. at a time $t = (17.47 \pm 0.02)$ y
 1842 resulting in an attenuation of the activity from 740 GBq in 1997 to 494 GBq in 2014. All the needed
 1843 information to extrapolate the flux through our detector in 2014 has now been assembled, leading
 1844 to the Table 5.3. It is interesting to note that for a common RPC sensitivity to γ of $2 \cdot 10^{-3}$, the
 1845 order of magnitude of the estimated hit rate per unit area is of the order of the kHz for the fully
 1846 opened source. Moreover, taking profit of the two working absorbers, it will be possible to scan
 1847 background rates at 0 Hz, ~ 300 Hz as well as ~ 600 Hz. Without source, a good estimate of the
 1848 intrinsic performance will be available. Then at 300 Hz, the goal will be to show that the detectors
 1849 fulfill the performance certification of CMS RPCs. Then a first idea of the performance of the
 1850 detectors at higher background will be provided with absorption factors 2 (~ 600 Hz) and 1 (no
 1851 absorption). *[Here I will also put a reference to the plot showing the estimated background rate at
 1852 the level of RE3/1 in the case of HL-LHC but this one being in another chapter, I will do it later.]*

Nominal ABS	Photon flux F [$s^{-1}cm^{-2}$]			Hit rate/unit area [$Hz cm^{-2}$] at $D^{2014} = 206$ cm
	at $D_0^{1997} = 50$ cm	at $D^{1997} = 206$ cm	at $D^{2014} = 206$ cm	
1	$0.12 \cdot 10^8 \pm 0.2\%$	$0.84 \cdot 10^6 \pm 0.3\%$	$0.56 \cdot 10^6 \pm 0.3\%$	1129 ± 32
2	$0.68 \cdot 10^7 \pm 0.3\%$	$0.48 \cdot 10^6 \pm 0.3\%$	$0.32 \cdot 10^6 \pm 0.3\%$	640 ± 19
5	$0.31 \cdot 10^7 \pm 0.4\%$	$0.22 \cdot 10^6 \pm 0.3\%$	$0.15 \cdot 10^6 \pm 0.3\%$	292 ± 9

Table 5.3: The data at D_0 in 1997 is taken from [58]. In a second step, using Equations 5.8 and 5.9, the flux at D can be estimated in 1997. Then, taking into account the attenuation of the source activity, the flux at D can be estimated at the time of the tests in GIF in 2014. Finally, assuming a sensitivity of the RPC to γ $s = 2 \cdot 10^{-3}$, an estimation of the hit rate per unit area is obtained.

1853 **5.3.4.2 Dose measurements**

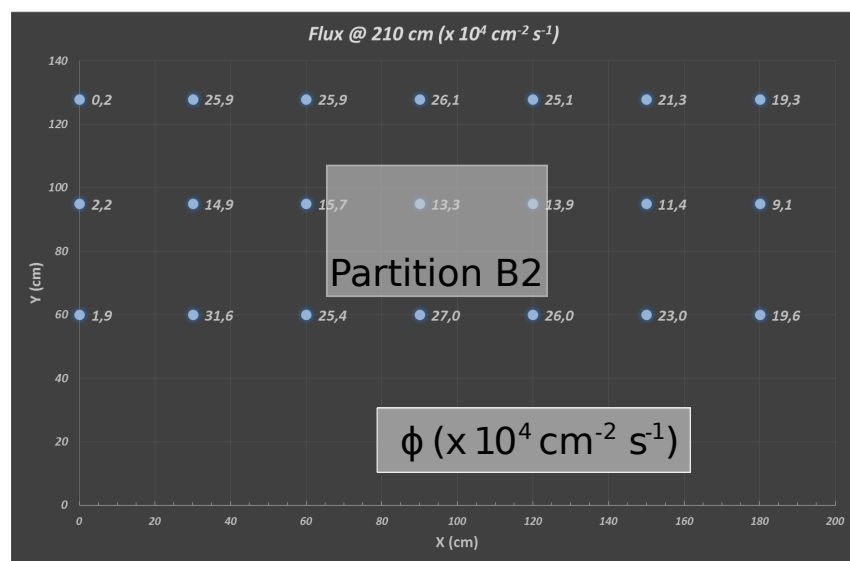


Figure 5.16: Dose measurements has been done in a plane corresponding to the tents front side. This plan is 1900 mm away from the source. As explained in the first chapter, a lens-shaped lead filter provides a uniform photon flux in the vertical plan orthogonal to the beam direction. If the second line of measured fluxes is not taken into account because of lower values due to experimental equipments in the way between the source and the tent, the uniformity of the flux is well showed by the results.

¹⁸⁵⁴ **5.3.5 Results and discussions**

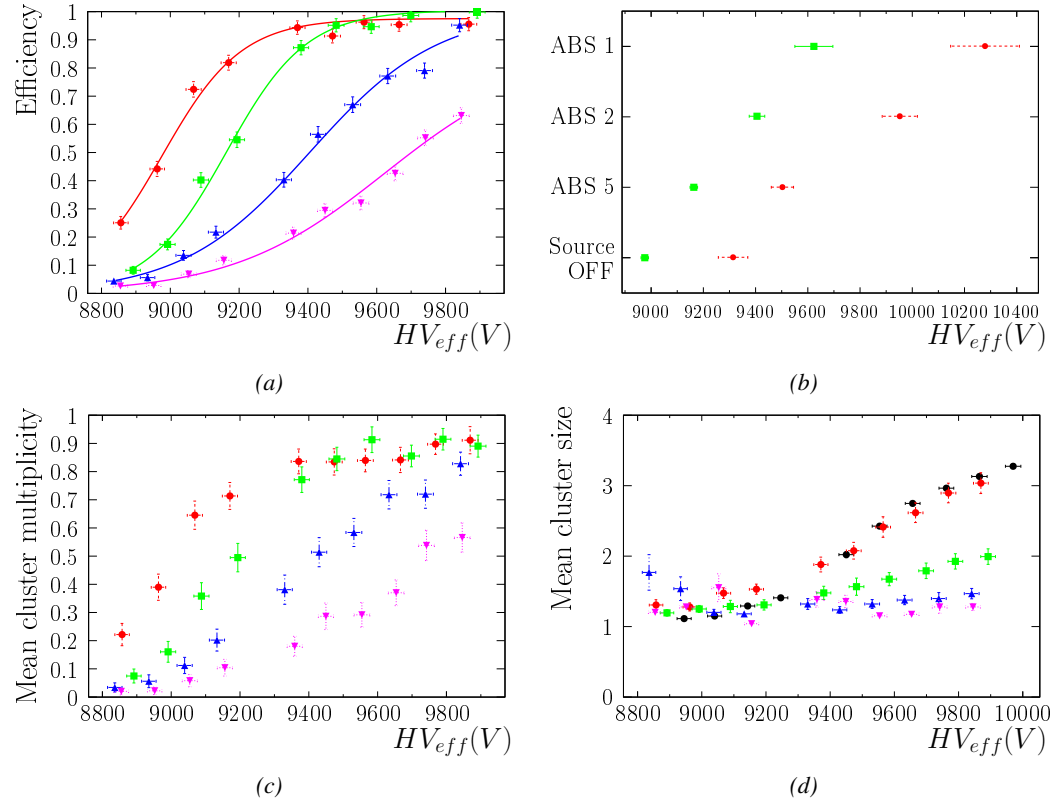


Figure 5.17

¹⁸⁵⁵ 5.4 Longevity tests at GIF++

¹⁸⁵⁶ Longevity studies imply a monitoring of the performance of the detectors probed using a high inten-
¹⁸⁵⁷ sity muon beam in a irradiated environment by periodically measuring their rate capability, the dark
¹⁸⁵⁸ current running through them and the bulk resistivity of the Bakelite composing their electrodes.
¹⁸⁵⁹ GIF++, with its very intense ^{137}Cs source, provides the perfect environment to perform such kind
¹⁸⁶⁰ of tests. Assuming a maximum acceleration factor of 3, it is expected to accumulate the equivalent
¹⁸⁶¹ charge in 1.7 years.

¹⁸⁶² As the maximum background is found in the endcap, the choice naturally was made to focus the
¹⁸⁶³ GIF++ longevity studies on endcap chambers. Most of the RPC system was installed in 2007. Nev-
¹⁸⁶⁴ ertheless, the large chambers in the fourth endcap (RE4/2 and RE4/3) have been installed during
¹⁸⁶⁵ LS1 in 2014. The Bakelite of these two different productions having different properties, four spare
¹⁸⁶⁶ chambers of the present system were selected, two RE2,3/2 spares and two RE4/2 spares. Having
¹⁸⁶⁷ two chambers of each type allows to always keep one of them non irradiated as reference, the per-
¹⁸⁶⁸ formance evolution of the irradiated chamber being then compared through time to the performance
¹⁸⁶⁹ of the non irradiated one.

¹⁸⁷⁰ The performance of the detectors under different level of irradiation is measured periodically dur-
¹⁸⁷¹ ing dedicated test beam periods using the H4 muon beam. In between these test beam periods, the
¹⁸⁷² two RE2,3/2 and RE4/2 chambers selected for this study are irradiated by the ^{137}Cs source in order
¹⁸⁷³ to accumulate charge and the gamma background is monitored, as well as the currents. The two
¹⁸⁷⁴ remaining chambers are kept non-irradiated as reference detectors. Due to the limited gas flow in
¹⁸⁷⁵ GIF++, the RE4 chamber remained non-irradiated until end of November 2016 where a new mass
¹⁸⁷⁶ flow controller has been installed allowing for bigger volumes of gas to flow in the system.

¹⁸⁷⁷ Figures 5.18 and 5.19 give us for different test beam periods, and thus for increasing integrated
¹⁸⁷⁸ charge through time, a comparison of the maximum efficiency, obtained using a sigmoid-like func-
¹⁸⁷⁹ tion, and of the working point of both irradiated and non irradiated chambers [47]. No aging is yet
¹⁸⁸⁰ to see from this data, the shifts in γ rate per unit area in between irradiated and non irradiated detec-
¹⁸⁸¹ tors and RE2 and RE4 types being easily explained by a difference of sensitivity due to the various
¹⁸⁸² Bakelite resistivities of the HPL electrodes used for the electrode production.

¹⁸⁸³ Collecting performance data at each test beam period allows us to extrapolate the maximum effi-
¹⁸⁸⁴ ciency for a background hit rate of $300\text{ Hz}/\text{cm}^2$ corresponding to the expected HL-LHC conditions.
¹⁸⁸⁵ Aging effects could emerge from a loss of efficiency with increasing integrated charge over time,
¹⁸⁸⁶ thus Figure 5.20 helps us understand such degradation of the performance of irradiated detectors in
¹⁸⁸⁷ comparison with non irradiated ones. The final answer for an eventual loss of efficiency is given in
¹⁸⁸⁸ Figure 5.21 by comparing for both irradiated and non irradiated detectors the efficiency sigmoids
¹⁸⁸⁹ before and after the longevity study. Moreover, to complete the performance information, the Bake-
¹⁸⁹⁰ lite resistivity is regularly measured thanks to Ag scans (Figure 5.22) and the noise rate is monitored
¹⁸⁹¹ weekly during irradiation periods (Figure 5.23). At the end of 2016, no signs of aging were observed
¹⁸⁹² and further investigation is needed to get closer to the final integrated charge requirements proposed
¹⁸⁹³ for the longevity study of the present CMS RPC sub-system.

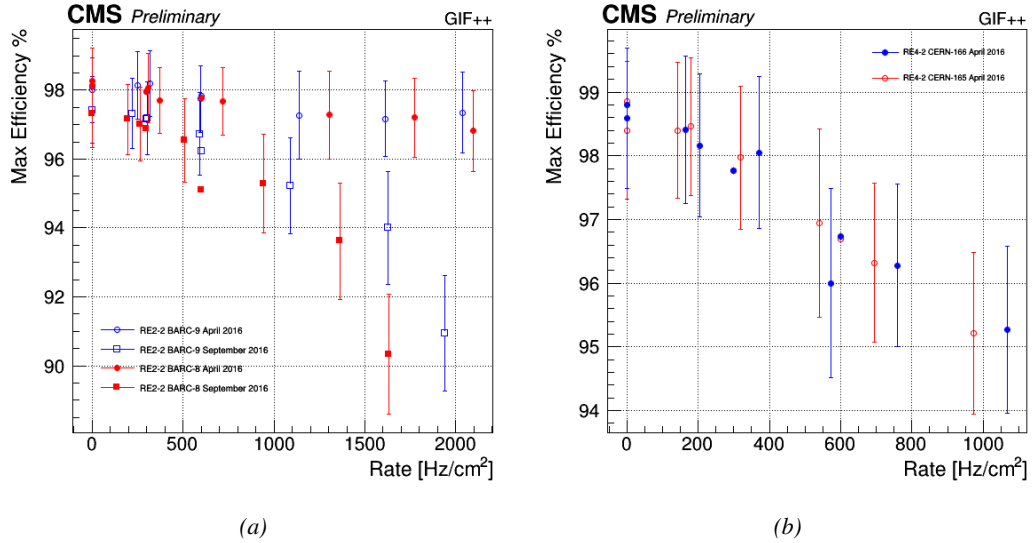


Figure 5.18: Evolution of the maximum efficiency for RE2 (5.18a) and RE4 (5.18b) chambers with increasing extrapolated γ rate per unit area at working point. Both irradiated (blue) and non irradiated (red) chambers are shown.

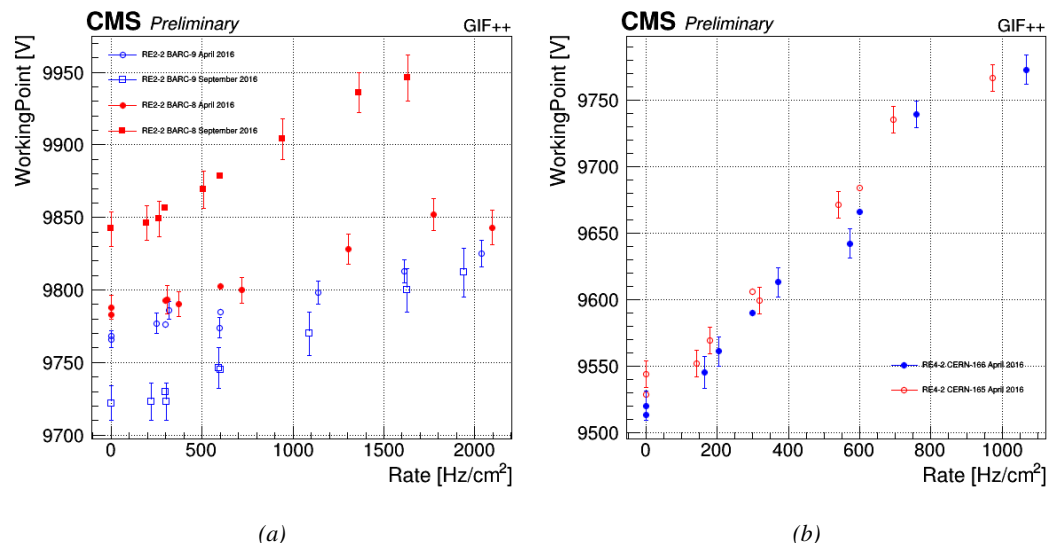


Figure 5.19: Evolution of the working point for RE2 (5.19a) and RE4 (5.19b) with increasing extrapolated γ rate per unit area at working point. Both irradiated (blue) and non irradiated (red) chambers are shown.

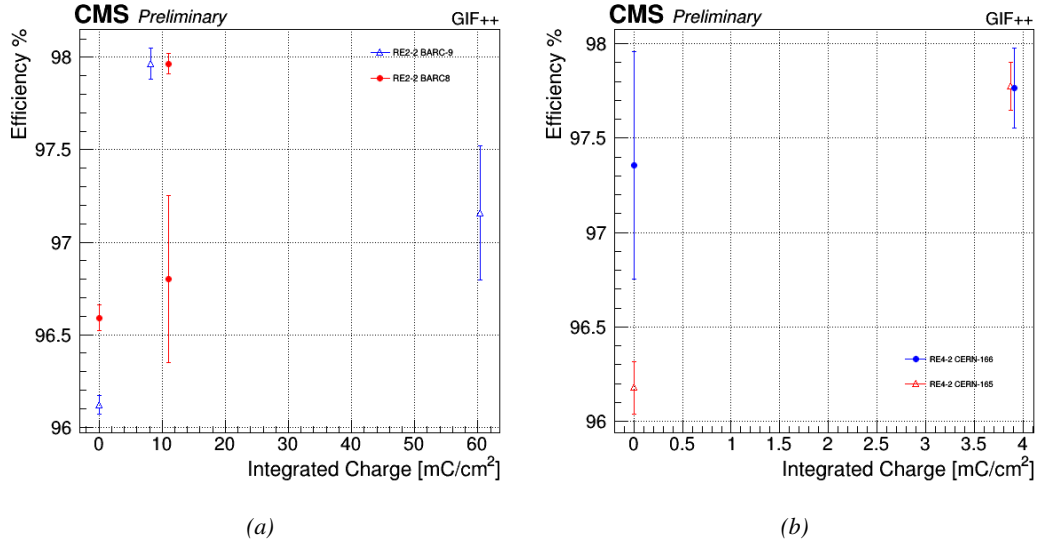


Figure 5.20: Evolution of the maximum efficiency at HL-LHC conditions, i.e. a background hit rate per unit area of 300 Hz/cm², with increasing integrated charge for RE2 (5.20a) and RE4 (5.20b) detectors. Both irradiated (blue) and non irradiated (red) chambers are shown. The integrated charge for non irradiated detectors is recorded during test beam periods and stays small with respect to the charge accumulated in irradiated chambers.

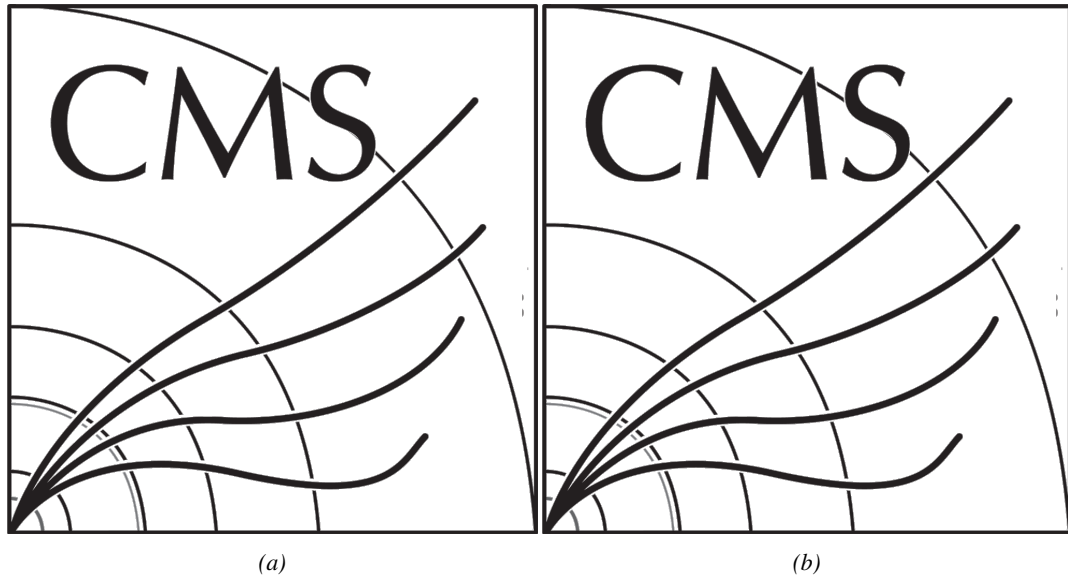


Figure 5.21: Comparison of the efficiency sigmoid before (triangles) and after (circles) irradiation for RE2 (5.21a) and RE4 (5.21b) detectors. Both irradiated (blue) and non irradiated (red) chambers are shown.

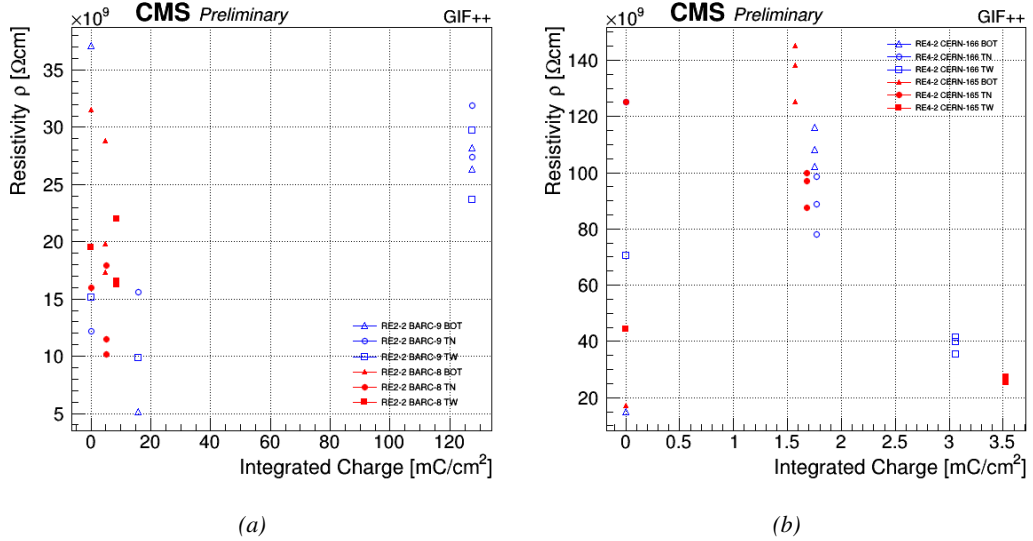


Figure 5.22: Evolution of the Bakelite resistivity for RE2 (5.22a) and RE4 (5.22b) detectors. Both irradiated (blue) and non-irradiated (red) chambers are shown.

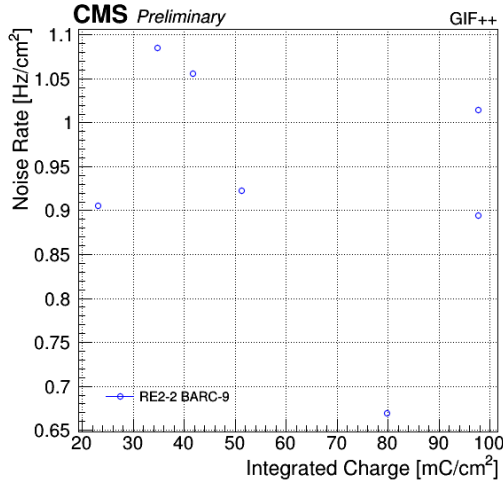


Figure 5.23: Evolution of the noise rate per unit area for the irradiated chamber RE2-2-BARC-9 only.

5.4.1 Description of the Data Acquisition

For the longevity studies, four spare chambers of the present system are used. Two spare RPCs of the RE2,3 stations as well as two spare RPCs from the new RE4 stations have been mounted in a Trolley. Six RE4 gaps are also placed in the trolley. The trolley is placed inside the Gif++ in the upstream region of the bunker, taking the cesium source as a reference. The trolley is oriented for the detection surface of the chambers to be orthogonal to the beam line. The system can be moved along the orthogonal plane in order to have the beam in all η -partitions. For the aging the trolley is

1902 moved outside the beam line and is placed in a distance of 5.2 m to the source, which irradiates the
 1903 bunker using an attenuation filter of 2.2 which corresponds to a fluence of 10^7 gamma/cm^2 .

1904 During GIF++ operation, the data collected can be divided into different categories as several
 1905 parameters are monitored in addition to the usual RPC performance data. On one hand, to know
 1906 the performance of a chamber, it is need to measure its efficiency and to know the background
 1907 conditions in which it is operated. To do this, the hit signals from the chamber are recorded and
 1908 stored in a ROOT file via a Data Acquisition (DAQ) software. On the other hand, it is also very
 1909 important to monitor parameters such as environmental pressure and temperature, gas temperature
 1910 and humidity, RPC HV, LV, and currents, or even source and beam status. This is done through the
 1911 GIF++ web Detector Control Software (DCS) that stores this information in a database.

1912 Two different types of tests are conducted on RPCs via the DAQ. Indeed, the performance of the
 1913 detectors is measured periodically during dedicated test beam periods using the H4 muon beam. In
 1914 between these test beam periods, when the beam is not available, the chambers are irradiated by the
 1915 ^{137}Cs in order to accumulate deposited charge and the gamma background is measured.

1916 RPCs under test are connected through LVDS cables to V1190A Time-to-Digital Converter
 1917 (TDC) modules manufactured by CAEN. These modules, located in the rack area outside of the
 1918 bunker, get the logic signals sent by the chambers and save them into their buffers. Due to the
 1919 limited size of the buffers, the collected data is regularly erased and replaced. A trigger signal is
 1920 needed for the TDC modules to send the useful data to the DAQ computer via a V1718 CAEN USB
 1921 communication module.

1922 In the case of performance test, the trigger signal used for data acquisition is generated by the
 1923 coincidence of three scintillators. A first one is placed upstream outside of the bunker, a second one
 1924 is placed downstream outside of the bunker, while a third one is placed in front of the trolley, close by
 1925 the chambers. Every time a trigger is sent to the TDCs, i.e. every time a muon is detected, knowing
 1926 the time delay in between the trigger and the RPC signals, signals located in the right time window
 1927 are extracted from the buffers and saved for later analysis. Signals are taken in a time window of
 1928 400 ns centered on the muon peak (here we could show a time spectrum). On the other hand, in the
 1929 case of background rate measurement, the trigger signal needs to be "random" not to measure muons
 1930 but to look at gamma background. A trigger pulse is continuously generated at a rate of 300 Hz using
 1931 a dual timer. To integrate an as great as possible time, all signals contained within a time window of
 1932 10us prior to the random trigger signal are extracted form the buffers and saved for further analysis
 1933 (here another time spectrum to illustrate could be useful, maybe even place both spectrum together
 1934 as a single Figure).

1935 The signals sent to the TDCs correspond to hit collections in the RPCs. When a particle hits
 1936 a RPC, it induce a signal in the pickup strips of the RPC readout. If this signal is higher than the
 1937 detection threshold, a LVDS signal is sent to the TDCs. The data is then organised into 4 branches
 1938 keeping track of the event number, the hit multiplicity for the whole setup, and the time and channel
 1939 profile of the hits in the TDCs.

1940 **5.4.2 RPC current, environmental and operation parameter monitoring**

1941 In order to take into account the variation of pressure and temperature between different data taking
 1942 periods the applied voltage is corrected following the relationship :

$$1943 HV_{eff} = HV_{app} \times \left(0.2 + 0.8 \cdot \frac{P_0}{P} \times \frac{T}{T_0} \right) \quad (5.10)$$

¹⁹⁴³ where T_0 (=293 K) and P_0 (=990 mbar) are the reference values.

¹⁹⁴⁴ **5.4.3 Measurement procedure**

¹⁹⁴⁵ Insert a short description of the online tools (DAQ, DCS, DQM).

¹⁹⁴⁶ Insert a short description of the offline tools : tracking and efficiency algorithm.

¹⁹⁴⁷ Identify long term aging effects we are monitoring the rates per strip.

¹⁹⁴⁸ **5.4.4 Longevity studies results**

6

1949

1950

Investigation on high rate RPCs

1951 **6.1 Rate limitations and ageing of RPCs**

1952 **6.1.1 Low resistivity electrodes**

1953 **6.1.2 Low noise front-end electronics**

1954 **6.2 Construction of prototypes**

1955 **6.3 Results and discussions**

7

1956

1957

Conclusions and outlooks

¹⁹⁵⁸ **7.1 Conclusions**

¹⁹⁵⁹ **7.2 Outlooks**

A

1960

1961

1962

A data acquisition software for CAEN VME TDCs

1963 Certifying detectors in the perspective of HL-LHC required to develop tools for the GIF++ experiment.
1964 Among them was the C++ Data Acquisition (DAQ) software that allows to make the communications
1965 in between a computer and TDC modules in order to retrieve the RPC data [60]. In this
1966 appendix, details about this software, as of how the software was written, how it functions and how
1967 it can be exported to another similar setup, will be given.

1968 A.1 GIF++ DAQ file tree

1969 GIF++ DAQ source code is fully available on github at https://github.com/afagot/GIF_DAQ. The software requires 3 non-optional dependencies:

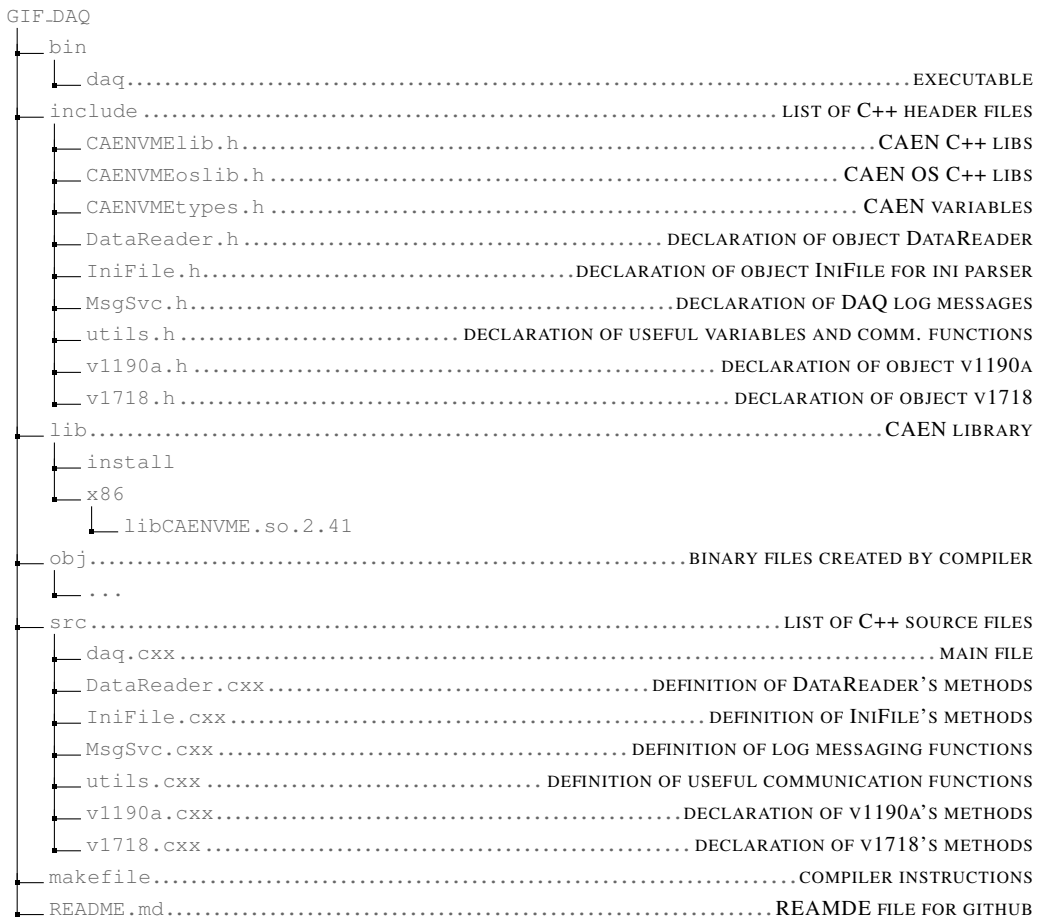
- 1971 • CAEN USB Driver, to mount the VME hardware,
- 1972 • CAEN VME Library, to communicate with the VME hardware, and
- 1973 • ROOT, to organize the collected data into a TTree.

1974 The CAEN VME library will not be packaged by distributions and will need to be installed man-
1975 ually. To compile the GIF++ DAQ project via a terminal, from the DAQ folder use the command:

1976 `make`

1978 The source code tree is provided below along with comments to give an overview of the files' con-
1979 tent. The different objects created for this project (`v1718`, `v1190a`, `IniFile` & `DataReader`) will be
1980 described in details in the following sections.

1981



1982 A.2 Usage of the DAQ

1983 GIF++ DAQ, as used in GIF++, is not a standalone software. Indeed, the system being more complexe,
 1984 the DAQ only is a sub-layer of the software architecture developped to control and monitor
 1985 the RPCs that are placed into the bunker for performance study in an irradiated environment. The top
 1986 layer of GIF++ is a Web Detector Control System (webDCS) application. The DAQ is only called
 1987 by the webDCS when data needs to be acquired. The webDCS operates the DAQ through command
 1988 line. To start the DAQ, the webDCS calls:

1989
 1990 bin/daq /path/to/the/log/file/in/the/output/data/folder

1991 where /path/to/the/log/file/in/the/output/data/folder is the only argument required. This
 1992 log file is important for the webDCS as this file contains all the content of the communication of the
 1993 webDCS and the different systems monitored by the webDCS. Its content is constantly displayed
 1994 during data taking for the users to be able to follow the operations. The communication messages
 1995 are normally sent to the webDCS log file via the functions declared in file MsgSvc.h, typically
 1996 MSG_INFO(string message).

1997

A.3 Description of the readout setup

The CMS RPC setup at GIF++ counts 5 V1190A Time-to-Digital Converter (TDC) manufactured by CAEN [61]. V1190A are VME units accepting 128 independent Multi-Hit/Multi-Event TDC channels whose signals are treated by 4 100 ps high performance TDC chips developed by CERN / ECP-MIC Division. The communication between the computer and the TDCs to transfer data is done via a V1718 VME master module also manufactured by CAEN and operated from a USB port [62]. These VME modules are all hosted into a 6U VME 6021 powered crate manufactured by W-Ie-Ne-R than can accomodate up to 21 VME bus cards [63]. These 3 components of the DAQ setup are shown in Figure A.1.

2007

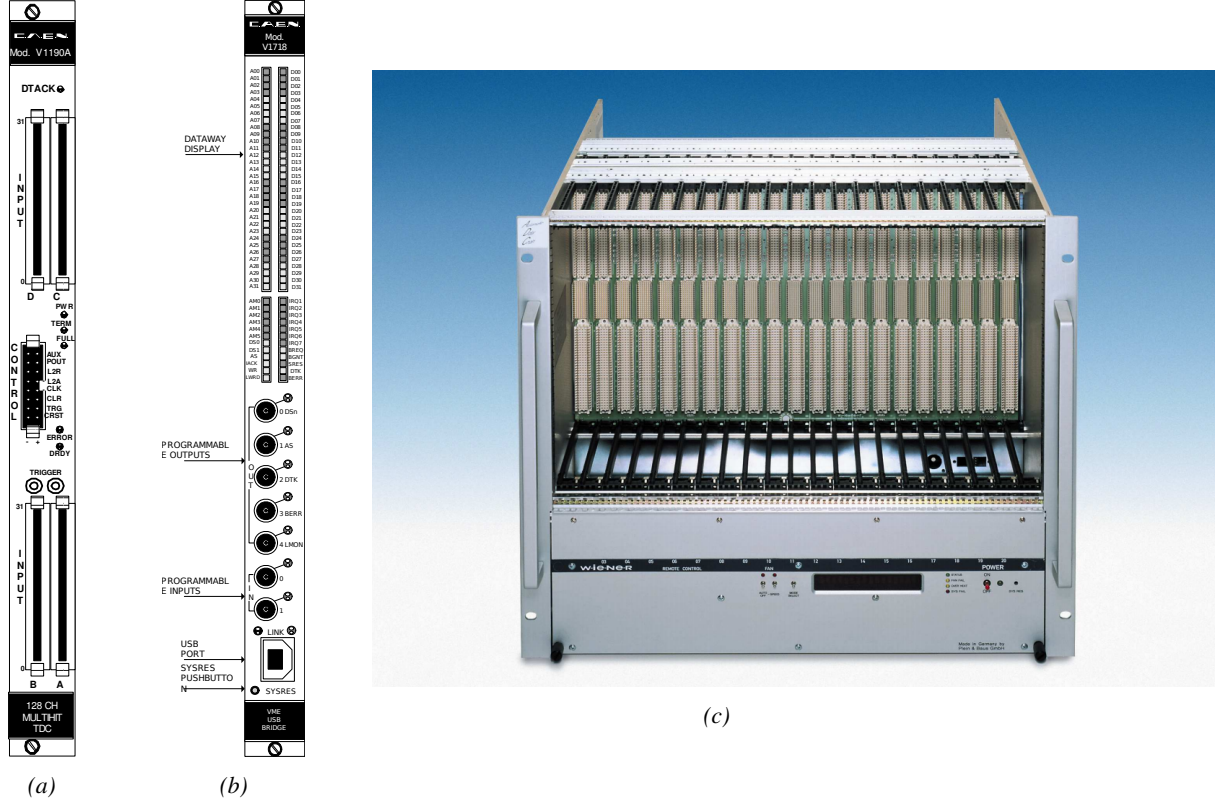


Figure A.1: (A.1a) View of the front panel of a V1190A TDC module [61]. (A.1b) View of the front panel of a V1718 Bridge module [62]. (A.1c) View of the front panel of a 6U 6021 VME crate [63].

2008

A.4 Data read-out

To efficiently perform a data readout algorithm, C++ objects to handle the VME modules (TDCs and VME bridge) have been created along with objects to store data and read the configuration file

2011 that comes as an input of the DAQ software.

2012

2013 A.4.1 V1190A TDCs

2014 The DAQ used at GIF takes profit of the *Trigger Matching Mode* offered by V1190A modules.
 2015 This setting is enabled through the method `v1190a::SetTrigMatching (int ntdcs)` where `ntdcs`
 2016 is the total number of TDCs in the setup this setting needs to be enabled for (Source Code A.1). A
 2017 trigger matching is performed in between a trigger time tag, a trigger signal sent into the TRIGGER
 2018 input of the TDC visible on Figure A.1a, and the channel time measurements, signals recorded from
 2019 the detectors under test in our case. Control over this data acquisition mode, explained through
 2020 Figure A.2, is offered via 4 programmable parameters:

- 2021 • **match window:** the matching between a trigger and a hit is done within a programmable time
 2022 window. This is set via the method

2023 `void v1190a::SetTrigWindowWidth(Uint windowHeight, int ntdcs)`

- 2024 • **window offset:** temporal distance between the trigger tag and the start of the trigger matching
 2025 window. This is set via the method

2026 `void v1190a::SetTrigWindowWidth(Uint windowHeight, int ntdcs)`

- 2027 • **extra search margin:** an extended time window is used to ensure that all matching hits are
 2028 found. This is set via the method

2029 `void v1190a::SetTrigSearchMargin(Uint searchMargin, int ntdcs)`

- 2030 • **reject margin:** older hits are automatically rejected to prevent buffer overflows and to speed
 2031 up the search time. This is set via the method

2032 `void v1190a::SetTrigRejectionMargin(Uint rejectMargin, int ntdcs)`

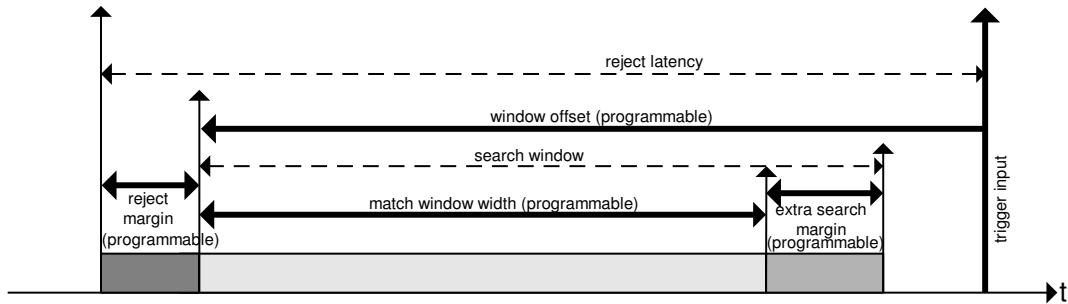


Figure A.2: Module V1190A Trigger Matching Mode timing diagram [61].

2033 Each of these 4 parameters are given in number of clocks, 1 clock being 25 ns long. It is easy to
 2034 understand at this level that there are 3 possible functioning settings:

- 2035 • **1:** the match window is entirely contained after the trigger signal,

- 2036 • **2:** the match window overlaps the trigger signal, or

- 2037 • **3:** the match window is entirely contained before the trigger signal as displayed on Figure A.2.

2038 In both the first and second cases, the sum of the window width and of the offset can be set to
2039 a maximum of 40 clocks, which corresponds to 1 μ s. Evidently, the offset can be negative, allowing
2040 for a longer match window, with the constraint of having the window ending at most 1 μ s after the
2041 trigger signal. In the third case, the maximum negative offset allowed is of 2048 clocks (12 bit) cor-
2042 responding to 51.2 μ s, the match window being strictly smaller than the offset. In the case of GIF++,
2043 the choice has been made to use this last setting by delaying the trigger signal. During the studies
2044 performed in GIF++, both the efficiency of the RPCs, probed using a muon beam, and the noise or
2045 gamma background rate are monitored. The extra search and reject margins are left unused.
2046 To probe the efficiency of RPC detectors, the trigger time tag is provided by the coïncidence of
2047 scintillators when a bunch of muons passes through GIF++ area is used to trigger the data acquisi-
2048 tion. For this measurement, it is useful to reduce the match window width only to contain the muon
2049 information. Indeed, the delay in between a trigger signal and the detection of the corresponding
2050 muon in the RPC being very contant (typically a few tens of ns due to jitter and cable length), the
2051 muon signals are very localised in time. Thus, due to a delay of approximalety 325 ns in between
2052 the muons and the trigger, the settings where chosen to have a window width of 24 clocks (600 ns)
2053 centered on the muon peak thanks to a negative offset of 29 clocks (725 ns).
2054 On the otherhand, monitoring the rates don't require for the DAQ to look at a specific time window.
2055 It is important to integrate enough time to have a robust measurement of the rate as the number of
2056 hits per time unit. The triggerring signal is provided by a pulse generator at a frequency of 300 Hz
2057 to ensure that the data taking occurs in a random way, with respect to beam physics, to probe only
2058 the irradiation spectrum on the detectors. The match window is set to 400 clocks (10 μ s) and the
2059 negative offset to 401 clocks as it needs to exceed the value of the match window.

```

2060
class v1190a
{
    private :
        long             Handle;
        vector<Data32>   Address;
        CVDataWidth      DataWidth;
        CVAddressModifier AddressModifier;

    public:

        v1190a(long handle, IniFile *inifile, int ntdcs);
        ~v1190a();
        Data16 write_op_reg(Data32 address, int code, string error);
        Data16 read_op_reg(Data32 address, string error);
        void Reset(int ntdcs);
        void Clear(int ntdcs);
        void TestWR(Data16 value,int ntdcs);
        void CheckTDCStatus(int ntdcs);
        void CheckCommunication(int ntdcs);
        void SetTDCTestMode(Data16 mode,int ntdcs);
        void SetTrigMatching(int ntdcs);
        void SetTrigTimeSubtraction(Data16 mode,int ntdcs);
        void SetTrigWindowWidth(Uint windowHeight,int ntdcs);
        void SetTrigWindowOffset(Uint windowOffset,int ntdcs);
        void SetTrigSearchMargin(Uint searchMargin,int ntdcs);
        void SetTrigRejectionMargin(Uint rejectMargin,int ntdcs);
        void GetTrigConfiguration(int ntdcs);
        void SetTrigConfiguration(IniFile *inifile,int ntdcs);
        void SetTDCDetectionMode(Data16 mode,int ntdcs);
        void SetTDCResolution(Data16 lsb,int ntdcs);
        void SetTDCDeadTime(Data16 time,int ntdcs);
        void SetTDCHeadTrailer(Data16 mode,int ntdcs);
        void SetTDCEventSize(Data16 size,int ntdcs);
        void SwitchChannels(IniFile *inifile,int ntdcs);
        void SetIRQ(Data32 level, Data32 count,int ntdcs);
        void SetBlockTransferMode(Data16 mode,int ntdcs);
        void Set(IniFile *inifile,int ntdcs);
        void CheckStatus(CVErrorCodes status) const;
        int ReadBlockD32(Uint tdc, const Data16 address,
                         Data32 *data, const Uint words, bool ignore_berr);
        Uint Read(RAWData *DataList,int ntdcs);
};

2061

```

2062 *Source Code A.1: Description of C++ object v1190a.*

2063 The v1190a object, defined in the DAQ software as in Source Code A.1, offers the possibility to
 2064 concatenate all TDCs in the readout setup into a single object containing a list of hardware addresses
 2065 (addresses to access the TDCs' buffer through the VME crate) and each constructor and method acts
 2066 on the list of TDCs.
 2067

2068 A.4.2 DataReader

2069 Enabled thanks to v1190a::SetBlockTransferMode(Data16 mode, int ntdcs), the data transfer
 2070 is done via Block Transfer (BLT). Using BLT allows to tranfer a fixed number of events called a
 2071 *block*. This is used together with an Almost Full Level (AFL) of the TDCs' output buffers, defined

2072 through `v1190a::SetIRQ(Data32 level, Data32 count, int ntdcs)`. This AFL gives the maximum amount of 32735 words (16 bits, corresponding to the depth of a TDC output buffer) that can
 2073 written in a buffer before an Interrupt Request (IRQ) is generated and seen by the VME Bridge,
 2074 stopping the data acquisition to transfer the content of each TDC buffers before resuming. For each
 2075 trigger, 6 words or more are written into the TDC buffer:

- 2077 • a **global header** providing information of the event number since the beginning of the data
 acquisition,
- 2079 • a **TDC header**,
- 2080 • the **TDC data** (*if any*), 1 for each hit recorded during the event, providing the channel and the
 time stamp associated to the hit,
- 2082 • a **TDC error** providing error flags,
- 2083 • a **TDC trailer**,
- 2084 • a **global trigger time tag** that provides the absolute trigger time relatively to the last reset,
 and
- 2086 • a **global trailer** providing the total word count in the event.

2087 As previously described in Section ??, CMS RPC FEEs provide us with 100 ns long LVDS out-
 2088 put signals that are injected into the TDCs' input. Any avalanche signal that gives a signal above the
 2089 FEEs threshold is thus recorded by the TDCs as a hit within the match window. Each hit is assigned
 2090 to a specific TDC channel with a time stamp, with a precision of 100 ps. The reference time, $t_0 = 0$,
 2091 is provided by the beginning of the match window. Thus for each trigger, coming from a scintillator
 2092 coincidence or the pulse generator, a list of hits is stored into the TDCs' buffers and will then be
 2093 transferred into a ROOT Tree.

2094 When the BLT is used, it is easy to understand that the maximum number of words that have
 2095 been set as ALF will not be a finite number of events or, at least, the number of events that would
 2096 be recorded into the TDC buffers will not be a multiple of the block size. In the last BLT cycle to
 2097 transfer data, the number of events to transfer will most probably be lower than the block size. In that
 2098 case, the TDC can add fillers at the end of the block but this option requires to send more data to the
 2099 computer and is thus a little slower. Another solution is to finish the transfer after the last event by
 2100 sending a bus error that states that the BLT reached the last event in the pile. This method has been
 2101 chosen in GIF++.

2103 Due to irradiation, an event in GIF++ can count up to 300 words per TDC. A limit of 4096 words
 2104 (12 bits) has been set to generate IRQ which represent from 14 to almost 700 events depending on
 2105 the average of hits collected per event. Then the block size has been set to 100 events with enabled
 2106 bus errors. When an AFL is reached for one of the TDCs, the VME bridge stops the acquisition by
 2107 sending a BUSY signal.

2109

2110 The data is then transferred one TDC at a time into a structure called `RAWData` (Source Code A.2).

```
2111
2112     struct RAWData{
2113         vector<int>           *EventList;
2114         vector<int>           *NHitsList;
2115         vector<int>           *QFlagList;
2116         vector<vector<int>>   *Channellist;
2117         vector<vector<float>>  *TimeStampList;
2118     };
```

2113 *Source Code A.2: Description of data holding C++ structure `RAWData`.*

2114 In order to organize the data transfer and the data storage, an object called `DataReader` was
2115 created (Source Code A.3). On one hand, it has `v1718` and `v1190a` objects as private members for
2116 communication purposes, such as VME modules settings via the configuration file `*iniFile` or data
2117 read-out through `v1190a::Read()` and on the other hand, it contains the structure `RAWData` that allows
2118 to organise the data in vectors reproducing the tree structure of a ROOT file.

```
2119
2120     class DataReader
2121     {
2122         private:
2123             bool      StopFlag;
2124             IniFile *iniFile;
2125             Data32   MaxTriggers;
2126             v1718   *VME;
2127             int       nTDCs;
2128             v1190a  *TDCs;
2129             RAWData TDCData;
2130
2131         public:
2132             DataReader();
2133             virtual ~DataReader();
2134             void      SetIniFile(string inifilename);
2135             void      SetMaxTriggers();
2136             Data32   GetMaxTriggers();
2137             void      SetVME();
2138             void      SetTDC();
2139             int       GetQFlag(Uint it);
2140             void      Init(string inifilename);
2141             void      FlushBuffer();
2142             void      Update();
2143             string   GetFileName();
2144             void      WriteRunRegistry(string filename);
2145             void      Run();
2146     };
```

2121 *Source Code A.3: Description of C++ object `DataReader`.*

2122 Each event is transferred from `TDCData` and saved into branches of a ROOT `TTree` as 3 integers
2123 that represent the event ID (`EventCount`), the number of hits read from the TDCs (`nHits`), and the
2124 quality flag that provides information for any problem in the data transfer (`qflag`), and 2 lists of
2125 `nHits` elements containing the fired TDC channels (`TDCCh`) and their respective time stamps (`TDCTS`),
2126 as presented in Source Code A.4. The ROOT file file is named using information contained into
2127 the configuration file, presented in section A.5.2. The needed information is extracted using method
2128 `DataReader::GetFileName()` and allow to build the output filename format `ScanXXXXXX_HVX_DAQ.root`

2129 where ScanXXXXXX is a 6 digit number representing the scan number into GIFT++ database and HVX
 2130 the HV step within the scan that can be more than a single digit. An example of ROOT data file is
 2131 provided with Figure A.3.

```
2132
2133     RAWData TDCData;
2134     TFile *outputFile = new TFile(outputFileName.c_str(),"recreate");
2135     TTree *RAWDataTree = new TTree("RAWData","RAWData");

2136     int          EventCount = -9;
2137     int          nHits    = -8;
2138     int          qflag    = -7;
2139     vector<int>   TDCCh;
2140     vector<float> TDCTS;

2141     RAWDataTree->Branch("EventNumber",&EventCount, "EventNumber/I");
2142     RAWDataTree->Branch("number_of_hits",&nHits, "number_of_hits/I");
2143     RAWDataTree->Branch("Quality_flag",&qflag, "Quality_flag/I");
2144     RAWDataTree->Branch("TDC_channel",&TDCCh);
2145     RAWDataTree->Branch("TDC_TimeStamp",&TDCTS);

2146 //...
2147 //Here read the TDC data using v1190a::Read() and place it into
2148 //TDCData for as long as you didn't collect the requested amount
2149 //of data.
2150 //...
2151
2152     for(Uint i=0; i<TDCData.EventList->size(); i++){
2153         EventCount = TDCData.EventList->at(i);
2154         nHits    = TDCData.NHitsList->at(i);
2155         qflag    = TDCData.QFlagList->at(i);
2156         TDCCh   = TDCData.ChannelList->at(i);
2157         TDCTS   = TDCData.TimeStampList->at(i);
2158         RAWDataTree->Fill();
2159     }
```

2154 *Source Code A.4: Highlight of the data transfer and organisation within DataReader::Run() after the data has been collected into TDCData.*

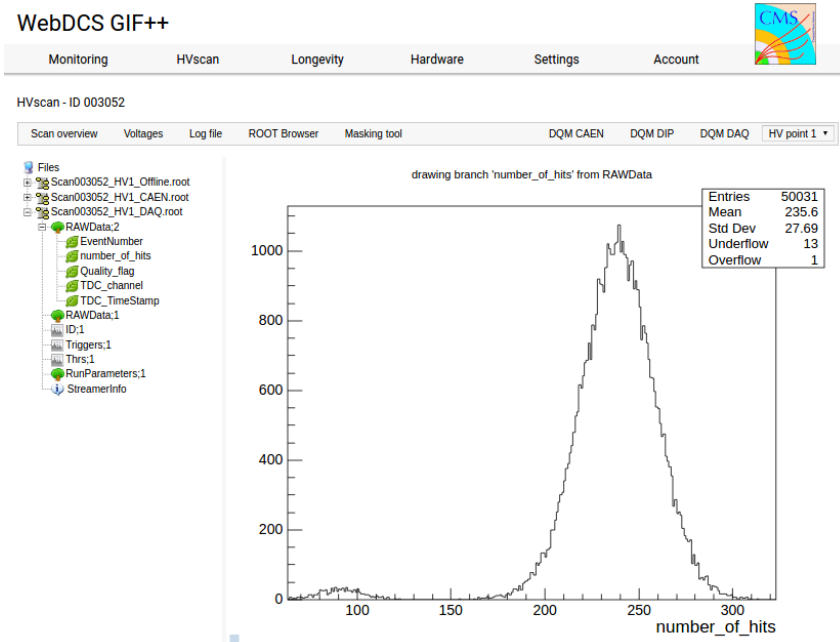


Figure A.3: Structure of the ROOT output file generated by the DAQ. The 5 branches (EventNumber, number_of_hits, Quality_flag, TDC_channel and TDC_TimeStamp) are visible on the left panel of the ROOT browser. On the right panel is visible the histogram corresponding to the variable nHits. In this specific example, there were approximately 50k events recorded to measure the gamma irradiation rate on the detectors. Each event is stored as a single entry in the TTree.

2135 A.4.3 Data quality flag

2136 Among the parameters that are recorded for each event, the quality flag, defined in Source Code A.5,
 2137 is determined on the fly by checking the data recorded by every single TDC. From method `v1190a::Read()`,
 2138 it can be understood that the content of each TDC buffer is readout one TDC at a time. Entries are
 2139 created in the data list for the first TDC and then, when the second buffer is readout, events corre-
 2140 sponding to entries that have already been created to store data for the previous TDC are added to
 2141 the existing list element. On the contrary, when an event entry has not been yet created in the data
 2142 list, a new entry is created.

```
2143
  typedef enum _QualityFlag {
    GOOD      = 1,
    CORRUPTED = 0
} QualityFlag;
```

2145 *Source Code A.5: Definition of the quality flag `enum`.*

2146 It is possible that each TDC buffer contains a different number of events. In cases where the first
 2147 element in the buffer list is an event for corresponds to a new entry, the difference in between the
 2148 entry from the buffer and the last entry in the data list is recorded and checked. If it is greater than 1,
 2149 what should never be the case, the quality flag is set to CORRUPTED for this TDC and an empty entry
 2150 is created in the place of the missing ones. Missing entries are believe to be the result of a bad hold

2151 on the TDC buffers at the moment of the readout. Indeed, the software hold is effective only on 1
 2152 TDC at a time and no solution as been found yet to completely block the writting in the buffers when
 2153 an IRQ is received.

2154 At the end of each BLT cycle, the ID of the last entry stored for each TDC buffer is not recorded.
 2155 When starting the next cycle, if the first entry in the pile corresponds to an event already existing
 2156 in the list, the readout will start from this list element and will not be able to check the difference
 2157 in between this entry's ID and the one of the last entry that was recorded for this TDC buffer in
 2158 the previous cycle. In the case events were missing, the flag stays at its initial value of 0, which is
 2159 similar to CORRUPTED and it is assumed that then this TDC will not contribute to `number_of_hits`,
 2160 `TDC_channel` or `TDC_TimeStamp`.

2161 Finally, since there will be 1 `RAWData` entry per TDC for each event (meaning `nTDCs` entries,
 2162 referring to `DataReader` private attribute), the individual flags of each TDC will be added together.
 2163 The final format is an integer composed `nTDCs` digits where each digit is the flag of a specific TDC.
 2164 This is constructed using powers of 10 like follows:

```
2165     TDC 0: QFlag = 100 × _QualityFlag
2166     TDC 1: QFlag = 101 × _QualityFlag
2167     ...
2168     TDC N: QFlag = 10N × _QualityFlag
```

2169 and the final flag to be with N digits:

2170 QFlag = n....3210

2171 each digit being 1 or 0. Below is given an example with a 4 TDCs setup.

2172 If all TDCs were good : QFlag = 1111,

2173 but if TDC 2 was corrupted : QFlag = 1011.

2174 When data taking is over and the data contained in the dynamical `RAWData` structure is transferred
 2175 to the ROOT file, all the 0s are changed into 2s by calling the method `DataReader::GetQFlag()`.
 2176 This will help translating the flag without knowing the number of TDCs beforehand. Indeed, a flag
 2177 111 could be due to a 3 TDC setup with 3 good individual TDC flags or to a more than 3 TDC setup
 2178 with TDCs those ID is greater than 2 being CORRUPTED, thus giving a 0.

2179 The quality flag has been introduced quite late, in October 2017 only, to the list of GIFT++ DAQ
 2180 parameters to be recorded into the output ROOT file. Before this addition, the missing data, corrupting
 2181 the quality for the offline analysis, was contributing to artificially fill data with lower multiplicity.
 2182 Looking at `TBranch number_of_hits` provides an information about the data of the full GIFT++
 2183 setup. When a TDC is not able to transfer data for a specific event, the effect is a reduction of the
 2184 total number of hits recorded in the full setup, this is what can be seen from Figure A.4. After offline
 2185 reconstruction detector by detector, the effect of missing events can be seen in the artificially filled
 2186 bin at multiplicity 0 shown in Figure A.5. Nonetheless, for data with high irradiation levels, as it is
 2187 the case for Figure A.5a, discarding the fake multiplicity 0 data can be done easily during the offline
 2188 analysis. At lower radiation, the missing events contribution becomes more problematic as the multi-
 2189 tiplicity distribution overlaps the multiplicity 0 and that in the same time the proportion of missing

2190 events decreases. Attempts to fit the distribution with a Poisson or skew distribution function were
 2191 not conclusive and this very problem has been at the origin of the quality flag that allows to give a
 2192 non ambiguous information about each event quality.

2193

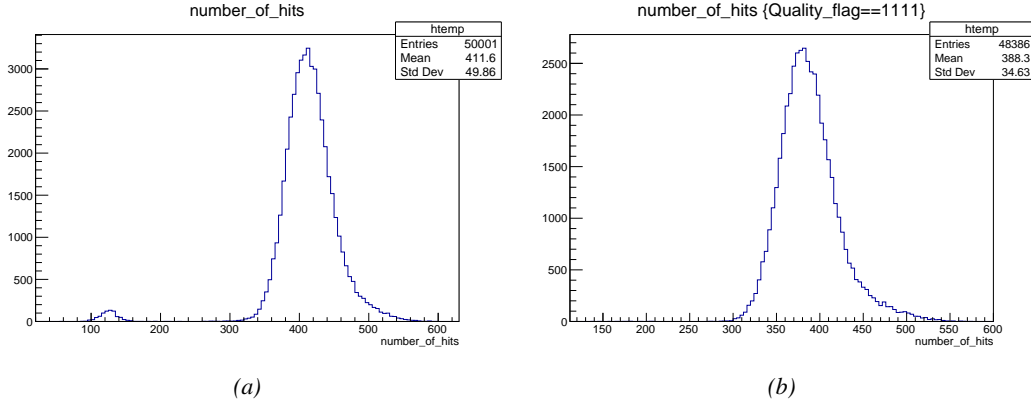


Figure A.4: The effect of the quality flag is explained by presenting the content of TBranch `number_of_hits` of a data file without `Quality_flag` in Figure A.4a and the content of the same TBranch for data corresponding to a `Quality_flag` where all TDCs were labelled as `GOOD` in Figure A.4b taken with similar conditions. It can be noted that the number of entries in Figure A.4b is slightly lower than in Figure A.4a due to the excluded events.

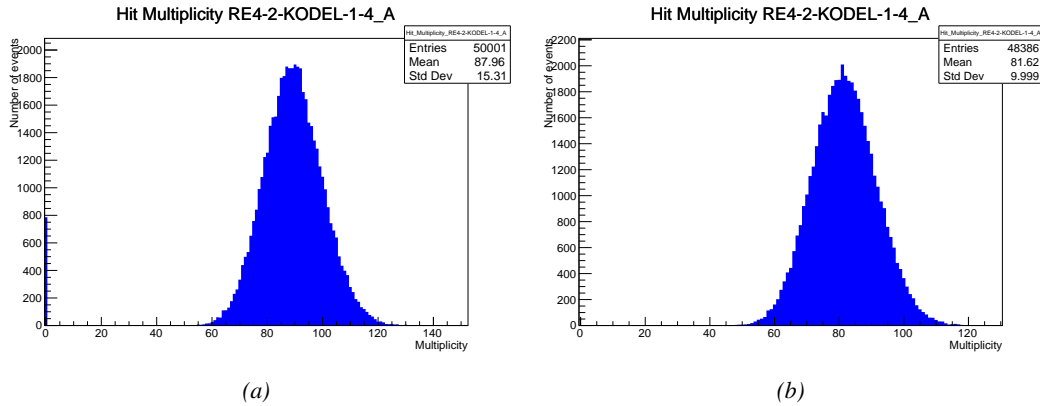


Figure A.5: Using the same data as previously showed in Figure A.4, the effect of the quality flag is explained by presenting the reconstructed hit multiplicity of a data file without `Quality_flag` in Figure A.5a and the reconstructed content of the same RPC partition for data corresponding to a `Quality_flag` where all TDCs were labelled as `GOOD` in Figure A.5b taken with similar conditions. The artificial high content of bin 0 is completely suppressed.

2194

A.5 Communications

2195 To ensure data readout and dialog in between the machine and the TDCs or in between the webDCS
 2196 and the DAQ, different communication solutions were used. First of all, it is important to have a

2197 module to allow the communication in between the TDCs and the computer from which the DAQ
 2198 operates. When this communication is effective, shifters using the webDCS to control data taking
 2199 can thus send instructions to the DAQ.

2200

2201 A.5.1 V1718 USB Bridge

2202 In the previous section, the data transfer has been discussed. The importance of the `v1718` object
 2203 (Source Code A.6), used as private member of `DataReader`, was not explicated. VME master
 2204 modules are used for communication purposes as they host the USB port that connects the pow-
 2205 ered crate buffer to the computer where the DAQ is installed. From the source code point of view,
 2206 this object is used to control the communication status, by reading the returned error codes with
 2207 `v1718::CheckStatus()`, or to check for IRQs coming from the TDCs through `v1718::CheckIRQ()`.
 2208 Finally, to ensure that triggers are blocked at the hardware level, a NIM pulse is sent out of one of the
 2209 5 programmable outputs (`v1718::SendBUSY()`) to the VETO of the coincidence module where the
 2210 trigger signals originate from. As long as this signal is ON, no trigger can reach the TDCs anymore.
 2211

```
2212 class v1718{
2213     private:
2214         int             Handle;
2215         Data32          Data;           // Data
2216         CVIRQLevels    Level;         // Interrupt level
2217         CVAddressModifier AM;          // Addressing Mode
2218         CVDataWidth     DataSize;       // Data Format
2219         Data32          BaseAddress;   // Base Address
2220
2221     public:
2222         v1718(IniFile *inifile);
2223         ~v1718();
2224         long            GetHandle(void) const;
2225         int             SetData(Data16 data);
2226         Data16          GetData(void);
2227         int             SetLevel(CVIRQLevels level);
2228         CVIRQLevels    GetLevel(void);
2229         int             SetAM(CVAddressModifier am);
2230         CVAddressModifier GetAM(void);
2231         int             SetDatasize(CVDataWidth datasize);
2232         CVDataWidth     GetDataSize(void);
2233         int             SetBaseAddress(Data16 baseaddress);
2234         Data16          GetBaseAddress(void);
2235         void            CheckStatus(CVErrorCodes status) const;
2236         void            CheckIRQ();
2237         void            SetPulsers();
2238         void            SendBUSY(BusyLevel level);
2239     };
2240 }
```

2213 *Source Code A.6: Description of C++ object v1718.*

2214 A.5.2 Configuration file

2215 The DAQ software takes as input a configuration file written using INI standard [64]. This file is
 2216 partly filled with the information provided by the shifters when starting data acquisition using the
 2217 webDCS, as shown by Figure A.6. This information is written in section [`General`] and will later

2218 be stored in the ROOT file that contains the DAQ data as can be seen from Figure A.3. Indeed,
 2219 another `TTree` called `RunParameters` as well as the 2 histograms `ID`, containing the scan number,
 2220 start and stop time stamps, and `Triggers`, containing the number of triggers requested by the shifter,
 2221 are available in the data files. Moreover, `ScanID` and `HV` are then used to construct the file name
 2222 thanks to the method `DataReader::GetFileName()`.

Chamber	RE2-2-NPD-BARC-8	RE4-2-CERN-106	RE2-3-NPD-BARC-9	RE4-2-CERN-105	RE4-2-KODEL-1-4	Max triggers
HV _{eff} 1	8600	8500	8600	8500	6500	
HV _{eff} 2	8700	8600	8700	8600	6600	
HV _{eff} 3	8800	8700	8800	8700	6700	
HV _{eff} 4	8900	8800	8900	8800	6800	
HV _{eff} 5	9000	8900	9000	8900	6900	
HV _{eff} 6	9100	9000	9100	9000	7000	
HV _{eff} 7	9200	9100	9200	9100	7100	
HV _{eff} 8	9300	9200	9300	9200	7200	
HV _{eff} 9	9400	9300	9400	9300	7300	
HV _{eff} 10	9500	9400	9500	9400	7400	

Figure A.6: WebDCS DAQ scan page. On this page, shifters need to choose the type of scan (Rate, Efficiency or Noise Reference scan), the gamma source configuration at the moment of data taking, the beam configuration, and the trigger mode. These information will be stored in the DAQ ROOT output. Are also given the minimal measurement time and waiting time after ramping up of the detectors is over before starting the data acquisition. Then, the list of HV points to scan and the number of triggers for each run of the scan are given in the table underneath.

2223 The rest of the information is written beforehand in the configuration file template, as explicated
 2224 in Source Code A.7, and contains the hardware addresses to the different VME modules in the
 2225 setup as well as settings for the TDCs. As the TDC settings available in the configuration file are not
 2226 supposed to be modified, an improvement would be to remove them from the configuration file and
 2227 to hardcode them inside of the DAQ code itself or to place them into a different INI file that would
 2228 host only the TDC settings to lower the probability for a bad manipulation of the configuration file
 2229 that can be modified from one of webDCS' menus.

2230

```

[General]
TdcS=4
ScanID=$scanid
HV=$HV
RunType=$runtype
MaxTriggers=$maxtriggers
Beam=$beam
[VMEInterface]
Type=V1718
BaseAddress=0xFF0000
Name=VmeInterface
[TDC0]
Type=V1190A
BaseAddress=0x00000000
Name=Tdc0
StatusA00-15=1
StatusA16-31=1
StatusB00-15=1
StatusB16-31=1
StatusC00-15=1
StatusC16-31=1
StatusD00-15=1
StatusD16-31=1
[TDC1]
Type=V1190A
BaseAddress=0x11110000
Name=Tdc1
StatusA00-15=1
StatusA16-31=1
StatusB00-15=1
StatusB16-31=1
StatusC00-15=1
StatusC16-31=1
StatusD00-15=1
StatusD16-31=1
2231
[TDC2]
Type=V1190A
BaseAddress=0x22220000
Name=Tdc2
StatusA00-15=1
StatusA16-31=1
StatusB00-15=1
StatusB16-31=1
StatusC00-15=1
StatusC16-31=1
StatusD00-15=1
StatusD16-31=1
[TDC3]
Type=V1190A
BaseAddress=0x44440000
Name=Tdc3
StatusA00-15=1
StatusA16-31=1
StatusB00-15=1
StatusB16-31=1
StatusC00-15=1
StatusC16-31=1
StatusD00-15=1
StatusD16-31=1
[TDCSettings]
TriggerExtraSearchMargin=0
TriggerRejectMargin=0
TriggerTimeSubtraction=0b1
TdcDetectionMode=0b01
TdcResolution=0b10
TdcDeadTime=0b00
TdcHeadTrailer=0b1
TdcEventSize=0b1001
TdcTestMode=0b0
BLTMode=1

```

Source Code A.7: INI configuration file template for 4 TDCs. In section [General], the number of TDCs is explicitated and information about the ongoing run is given. Then, there are sections for each and every VME modules. There buffer addresses are given and for the TDCs, the list of channels to enable is given. Finally, in section [TDCSettings], a part of the TDC settings are given.

2232 In order to retrieve the information of the configuration file, the object `IniFile` has been developed
 2233 to provide an INI parser, presented in Source Code A.8. It contains private methods returning a
 2234 boolean to check the type of line written in the file, whether a comment, a group header or a key line
 2235 (`IniFile::CheckIfComment()`, `IniFile::CheckIfGroup()` and `IniFile::CheckIfToken()`). The
 2236 key may sometimes be referred to as *token* in the source code. Moreover, the private element
 2237 `FileData` is a map of `const string` to `string` that allows to store the data contained inside the
 2238 configuration file via the public method `IniFile::GetFileData()` following the formatting (see
 2239 method `IniFile::Read()`):

```
2241
2242     string group, token, value;
2243     // Get the field values for the 3 strings.
2244     // Then concatenate group and token together as a single string
2245     // with a dot separation.
2246     token = group + "." + token;
2247     FileData[token] = value;
```

2243 More methods have been written to translate the different keys into the right variable format
 2244 when used by the DAQ. For example, to get a `float` value out of the configuration file data, knowing
 2245 the group and the key needed, the method `IniFile::floatType()` can be used. It takes 3 arguments
 2246 being the group name and key name (both `string`), and a default `float` value used as exception in
 2247 the case the expected combination of group and key cannot be found in the configuration file. This
 2248 default value is then used and the DAQ continues on working after sending an alert in the log file for
 2249 further debugging.

```

2250
typedef map< const string, string > IniFileData;

class IniFile{
private:
    bool      CheckIfComment(string line);
    bool      CheckIfGroup(string line, string& group);
    bool      CheckIfToken(string line, string& key, string& value);
    string    FileName;
    IniFileData FileData;
    int       Error;

public:
    IniFile();
    IniFile(string filename);
    virtual ~IniFile();

    // Basic file operations
    void      SetFileName(string filename);
    int       Read();
    int       Write();
    IniFileData GetFileData();

    // Data readout methods
    Data32    addressType (string groupname, string keyname, Data32
2251    defaultValue);
    long      intType     (string groupname, string keyname, long
    defaultValue);
    long long  longType   (string groupname, string keyname, long long
    defaultValue );
    string    stringType  (string groupname, string keyname, string
    defaultValue );
    float     floatType   (string groupname, string keyname, float
    defaultValue );

    // Error methods
    string    GetErrorMsg();
};

}

```

2252 *Source Code A.8: Description of C++ object `IniFile` used as a parser for INI file format.*

2253 A.5.3 WebDCS/DAQ intercommunication

2254 When shifters send instructions to the DAQ via the configuration file, it is the webDCS itself that
 2255 gives the start command to the DAQ and then the 2 softwares use inter-process communication
 2256 through file to synchronise themselves. This communication file is represented by the variable `const`
 2257 `string __runstatuspath`.

2258 On one side, the webDCS sends commands or status that are readout by the DAQ:

- 2259 ● INIT, status sent when launching a scan and read via function `CtrlRunStatus(...)`,
- 2260 ● START, command to start data taking and read via function `CheckSTART()`,
- 2261 ● STOP, command to stop data taking at the end of the scan and read via function `CheckSTOP()`,
 2262 and
- 2263 ● KILL, command to kill data taking sent by user and read via function `CheckKILL()`

and on the other, the DAQ sends status that are controled by the webDCS:

- 2265 ● `DAQ_RDY`, sent with `SendDAQReady()` to signify that the DAQ is ready to receive commands
2266 from the webDCS,
- 2267 ● `RUNNING`, sent with `SendDAQRunning()` to signify that the DAQ is taking data,
- 2268 ● `DAQ_ERR`, sent with `SendDAQError()` to signify that the DAQ didn't receive the expected com-
2269 mand from the webDCS or that the launch command didn't have the right number of argu-
2270 ments,
- 2271 ● `RD_ERR`, sent when the DAQ wasn't able to read the communication file, and
- 2272 ● `WR_ERR`, sent when the DAQ wasn't able to write into the communication file.

2273 **A.5.4 Example of inter-process communication cycle**

2274 Under normal conditions, the webDCS and the DAQ processes exchange commands and status via
2275 the file hosted at the address `__runstatuspath`, as explained in subsection A.5.3. An example of
2276 cycle is given in Table A.1. In this example, the steps 3 to 5 are repeated as long as the webDCS tells
2277 the DAQ to take data. A data taking cycle is the equivalent as what is called a *Scan* in GIFT++ jargon,
2278 referring to a set a runs with several HV steps. Each repetition of steps 3 to 5 is then equivalent to a
2279 single *Run*.

2280 At any moment during the data taking, for any reason, the shifter can decide that the data taking
2281 needs to be stopped before it reached the end of the scheduled cycle. Thus at any moment on the
2282 cycle, the content of the inter-process communication file will be changed to `KILL` and the DAQ will
2283 shut down right away. The DAQ checks for `KILL` signals every 5s after the TDCs configuration is
2284 over. So far, the function `CheckKILL()` has been used only inside of the data taking loop of method
2285 `DataReader::Run()` and thus, if the shifter decides to KILL the data taking during the TDC con-
2286 figuration phase or the HV ramping in between 2 HV steps, the DAQ will not be stopped smoothly
2287 and a *force kill* command will be sent to stop the DAQ process that is still awake on the computer.
2288 Improvements can be brought on this part of the software to make sure that the DAQ can safely
2289 shutdown at any moment.

2292 **A.6 Software export**

2293 In section A.2 was discussed the fact that the DAQ as written in its last version is not a standalone
2294 software. It is possible to make it a standalone program that could be adapted to any VME setup
2295 using V1190A and V1718 modules by creating a GUI for the software or by printing the log mes-
2296 sages that are normally printed in the webDCS through the log file, directly into the terminal. This
2297 method was used by the DAQ up to version 3.0 moment where the webDCS was completed. Also, it
2298 is possible to check branches of DAQ v2.X to have example of communication through a terminal.

2299 DAQ v2.X is nonetheless limited in it's possibilities and requires a lot of offline manual interven-
2300 tions from the users. Indeed, there is no communication of the software with the detectors' power
2302 supply system that would allow for a user a predefine a list of voltages to operate the detectors at

step	actions of webDCS	status of DAQ	<code>__runstatuspath</code>
1	launch DAQ ramp voltages ramping over wait for currents stabilization	readout of IniFile configuration of TDCs	INIT
2		configuration done send DAQ ready wait for START signal	DAQ_RDY
3	waiting time over send START		START
4	wait for run to end monitor DAQ run status	data taking ongoing check for KILL signal	RUNNING
5		run over send DAQ_RDY wait for next DCS signal	DAQ_RDY
6	ramp voltages ramping over wait for currents stabilization		DAQ_RDY
3	waiting time over send START		START
4	wait for run to end monitor DAQ run status	update IniFile information data taking ongoing check for KILL signal	RUNNING
5		run over send DAQ_RDY wait for next DCS signal	DAQ_RDY
7	send command STOP	DAQ shuts down	STOP

Table A.1: Inter-process communication cycles in between the webDCS and the DAQ through file string signals.

2303 and loop over to take data without any further manual intervention. In v2.X, the data is taken for a
2304 single detector setting and at the end of each run, the softwares asks the user if he intends on taking
2305 more runs. If so, the software invites the user to set the operating voltages accordingly to what is
2306 necessary and to manual update the configuration file in consequence. This working mode can be a
2307 very first approach before an evolution and has been successfully used by colleagues from different
2308 collaborations.

2309
2310 For a more robust operation, it is recommended to develop a GUI or a web application to inter-
2311 face the DAQ. Moreover, to limit the amount of manual interventions, and thus the probability to
2312 make mistakes, it is also recommended to add an extra feature into the DAQ by installing the HV
2313 Wrapper library provided by CAEN of which an example of use in a similar DAQ software devel-
2314 opped by a master student of UGent, and called TinyDAQ, is provided on UGent's github. Then, this
2315 HV Wrapper will help you communicating with and give instructions to a CAEN HV powered crate
2316 and can be added into the DAQ at the same level where the communication with the user was made
2317 in DAQ v2.X. In case you are using another kind of power system for your detectors, it is stringly
2318 adviced to use HV modules or crates that can be remotely controled via a using C++ libraries.

2319

B

2320

2321

Details on the offline analysis package

2322 The data collected in GIF++ thanks to the DAQ described in Appendix A is difficult to interpret by
2323 a human user that doesn't have a clear idea of the raw data architecture of the ROOT data files. In
2324 order to render the data human readable, a C++ offline analysis tool was designed to provide users
2325 with detector by detector histograms that give a clear overview of the parameters monitored during
2326 the data acquisition [65]. In this appendix, details about this software in the context of GIF++, as of
2327 how the software was written and how it functions will be given.

2328 B.1 GIF++ Offline Analysis file tree

2329 GIF++ Offline Analysis source code is fully available on github at https://github.com/aafagot/GIF_OfflineAnalysis. The software requires ROOT as non-optionnal dependency
2330 as it takes ROOT files in input and write an output ROOT file containing histograms. To compile the
2331 GIF++ Offline Analysis project is compiled with cmake. To compile, first a build/ directory must
2332 be created to compile from there:
2333

```
2334 mkdir build
2335 cd build
2336 cmake ..
2337 make
2338 make install
```

2336 To clean the directory and create a new build directory, the bash script cleandir.sh can be used:

```
2337
2338 ./cleandir.sh
```

2339 The source code tree is provided below along with comments to give an overview of the files' con-
2340 tent. The different objects created for this project (`Infrastructure`, `Trolley`, `RPC`, `Mapping`, `RPCHit`,
2341 `RPCCluster` and `Inifile`) will be described in details in the following sections.

2342

```

GIF_OfflineAnalysis
├── bin
│   └── offlineanalysis ..... EXECUTABLE
├── build..... CMAKE COMPILATION DIRECTORY
└── ...
    ├── include..... LIST OF C++ HEADER FILES
    │   ├── Cluster.h..... DECLARATION OF OBJECT RPCCLUSTER
    │   ├── Current.h..... DECLARATION OF GETCURRENT ANALYSIS MACRO
    │   ├── GIFTrolley.h..... DECLARATION OF OBJECT TROLLEY
    │   ├── Infrastructure.h..... DECLARATION OF OBJECT INFRASTRUCTURE
    │   ├── IniFile.h..... DECLARATION OF OBJECT INI FILE FORINI PARSER
    │   ├── Mapping.h..... DECLARATION OF OBJECT MAPPING
    │   ├── MsgSvc.h..... DECLARATION OF OFFLINE LOG MESSAGES
    │   ├── OfflineAnalysis.h..... DECLARATION OF DATA ANALYSIS MACRO
    │   ├── RPCTracker.h..... DECLARATION OF OBJECT RPC
    │   ├── RPCHit.h..... DECLARATION OF OBJECT RPCHIT
    │   ├── types.h..... DEFINITION OF USEFUL VARIABLE TYPES
    │   └── utils.h..... DECLARATION OF USEFUL FUNCTIONS
    ├── obj..... BINARY FILES CREATED BY COMPILER
    └── ...
        ├── src..... LIST OF C++ SOURCE FILES
        │   ├── Cluster.cc..... DEFINITION OF OBJECT RPCCLUSTER
        │   ├── Current.cc..... DEFINITION OF GETCURRENT ANALYSIS MACRO
        │   ├── GIFTrolley.cc..... DEFINITION OF OBJECT TROLLEY
        │   ├── Infrastructure.cc..... DEFINITION OF OBJECT INFRASTRUCTURE
        │   ├── IniFile.cc..... DEFINITION OF OBJECT INI FILE FORINI PARSER
        │   ├── main.cc..... MAIN FILE
        │   ├── Mapping.cc..... DEFINITION OF OBJECT MAPPING
        │   ├── MsgSvc.cc..... DEFINITION OF OFFLINE LOG MESSAGES
        │   ├── OfflineAnalysis.cc..... DEFINITION OF DATA ANALYSIS MACRO
        │   ├── RPCTracker.cc..... DEFINITION OF OBJECT RPC
        │   ├── RPCHit.cc..... DEFINITION OF OBJECT RPCHIT
        │   └── utils.cc..... DEFINITION OF USEFUL FUNCTIONS
        ├── cleandir.sh..... BASH SCRIPT TO CLEAN BUILD DIRECTORY
        ├── CMakeLists.txt..... SET OF INSTRUCTIONS FOR CMAKE
        ├── config.h.in..... DEFINITION OF VERSION NUMBER
        └── README.md..... README FILE FOR GITHUB

```

2343

B.2 Usage of the Offline Analysis

2344

In order to use the Offline Analysis tool, it is necessary to know the Scan number and the HV Step of the run that needs to be analysed. This information needs to be written in the following format:

2346

2347

```
Scan00XXXX_HVY
```

2348

where XXXX is the scan ID and Y is the high voltage step (in case of a high voltage scan, data will be taken for several HV steps). This format corresponds to the base name of data files in the database

2349

2350 of the Gif++ webDCS. Usually, the offline analysis tool is automatically called by the webDCS at
 2351 the end of data taking or by a user from the webDCS panel if an update of the tool was brought.
 2352 Nonetheless, an expert can locally launch the analysis for tests on the Gif++ computer, or a user can
 2353 get the code on its local machine from github and download data from the webDCS for its own anal-
 2354 ysis. To launch the code, the following command can be used from the `GIF_OfflineAnalysis` folder:

2355

```
2356 bin/offlineanalysis /path/to/Scan00XXXX_HVY
```

2357 where, `/path/to/Scan00XXXX_HVY` refers to the local data files. Then, the offline tool will by itself
 2358 take care of finding all available ROOT data files present in the folder, as listed below:

2359

- `Scan00XXXX_HVY_DAQ.root` containing the TDC data as described in Appendix ?? (events, hit
 2360 and timestamp lists), and
- `Scan00XXXX_HVY_CAEN.root` containing the CAEN mainframe data recorded by the monitor-
 2362 ing tool webDCS during data taking (HVs and currents of every HV channels). This file is
 2363 created independently of the DAQ.

2364 **B.2.1 Output of the offline tool**

2365 **B.2.1.1 ROOT file**

2366 The analysis gives in output ROOT datafiles that are saved into the data folder and called using the
 2367 naming convention `Scan00XXXX_HVY_Offline.root`. Inside those, a list of `TH1` histograms can be
 2368 found. Its size will vary as a function of the number of detectors in the setup as each set of histograms
 2369 is produced detector by detector. For each partition of each chamber, can be found:

2370

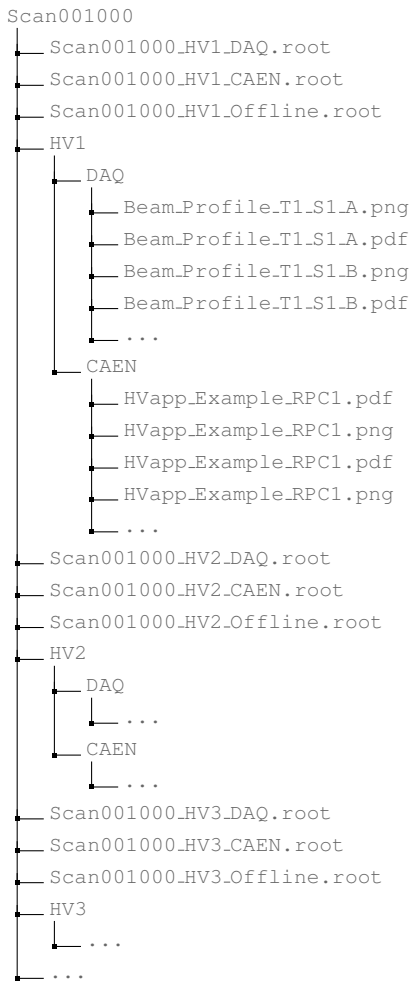
- `Time_Profile_Tt_Sc_p` shows the time profile of all recorded events (number of events per
 2371 time bin),
- `Hit_Profile_Tt_Sc_p` shows the hit profile of all recorded events (number of events per chan-
 2373 nel),
- `Hit_Multiplicity_Tt_Sc_p` shows the hit multiplicity (number of hits per event) of all recorded
 2375 events (number of occurrences per multiplicity bin),
- `Strip_Mean_Noise_Tt_Sc_p` shows noise/gamma rate per unit area for each strip in a se-
 2377 lected time range. After filters are applied on `Time_Profile_Tt_Sc_p`, the filtered version
 2378 of `Hit_Profile_Tt_Sc_p` is normalised to the total integrated time and active detection area
 2379 of a single channel,
- `Strip_Activity_Tt_Sc_p` shows noise/gamma activity for each strip (normalised version of
 2381 previous histogram - strip activity = strip rate / average partition rate),
- `Strip_Homogeneity_Tt_Sc_p` shows the *homogeneity* of a given partition ($\text{homogeneity} = \exp(-\text{strip rates standard deviation(strip rates in partition/average partition rate)})$),
- `mask_Strip_Mean_Noise_Tt_Sc_p` shows noise/gamma rate per unit area for each masked
 2385 strip in a selected time range. Offline, the user can control the noise/gamma rate and decide to
 2386 mask the strips that are judged to be noisy or dead. This is done via the *Masking Tool* provided
 2387 by the webDCS,

- 2388 ● `mask_Strip_Activity_Tt_Sc_p` shows noise/gamma activity per unit area for each masked
2389 strip with respect to the average rate of active strips,
- 2390 ● `NoiseCSize_H_Tt_Sc_p` shows noise/gamma cluster size, a cluster being constructed out of
2391 adjacent strips giving a signal at the *same time* (hits within a time window of 25 ns),
- 2392 ● `NoiseCMult_H_Tt_Sc_p` shows noise/gamma cluster multiplicity (number of reconstructed
2393 clusters per event),
- 2394 ● `Chip_Mean_Noise_Tt_Sc_p` shows the same information than `Strip_Mean_Noise_Tt_Scp` us-
2395 ing a different binning (1 chip corresponds to 8 strips),
- 2396 ● `Chip_Activity_Tt_Sc_p` shows the same information than `Strip_Activity_Tt_Scp` using
2397 chip binning,
- 2398 ● `Chip_Homogeneity_Tt_Sc_p` shows the homogeneity of a given partition using chip binning,
- 2399 ● `Beam_Profile_Tt_Sc_p` shows the estimated beam profile when taking efficiency scan. This
2400 is obtained by filtering `Time_Profile_Tt_Sc_p` to only consider the muon peak where the
2401 noise/gamma background has been subtracted. The resulting hit profile corresponds to the
2402 beam profile on the detector channels,
- 2403 ● `L0_Efficiency_Tt_Sc_p` shows the level 0 efficiency that was estimated **without** muon track-
2404 ing,
- 2405 ● `MuonCSize_H_Tt_Sc_p` shows the level 0 muon cluster size that was estimated **without** muon
2406 tracking, and
- 2407 ● `MuonCMult_H_Tt_Sc_p` shows the level 0 muon cluster multiplicity that was estimated **without**
2408 muon tracking.

2409 In the histogram labels, t stands for the trolley number (1 or 3), c for the chamber slot label in
2410 trolley t and p for the partition label (A, B, C or D depending on the chamber layout) as explained
2411 in Chapter 5.4.

2412 In the context of GIF++, an extra script called by the webDCS is called to extract the histograms
2413 from the ROOT files. The histograms are then stored in PNG and PDF formats into the correspond-
2414 ing folder (a single folder per HV step, so per ROOT file). the goal is to then display the histograms
2415 on the Data Quality Monitoring (DQM) page of the webDCS in order for the users to control the
2416 quality of the data taking at the end of data taking. An example of histogram organisation is given
2417 below:

2418
2419



2420 *Here can put some screens from the webDCS to show the DQM and the plots available to users.*
 2421

2422 **B.2.1.2 CSV files**

2423 Moreover, up to 3 CSV files can be created depending on which ones of the 3 input files were in the
 2424 data folder:

- 2425 ● `Offline-Corrupted.csv` , is used to keep track of the amount of data that was corrupted and
 2426 removed from old data format files that don't contain any data quality flag.
- 2427 ● `Offline-Current.csv` , contains the summary of the currents and voltages applied on each
 2428 RPC HV channel.
- 2429 ● `Offline-L0-EffC1.csv` , is used to write the efficiencies, cluster size and cluster multiplicity
 2430 of efficiency runs. Note that `L0` refers here to *Level 0* and means that the results of efficiency and
 2431 clusterization are a first approximation calculated without performing any muon tracking in

2432 between the different detectors. This offline tool provides the user with a preliminar calculation
 2433 of the efficiency and of the muon event parameters. Another analysis software especially
 2434 dedicated to muon tracking is called on selected data to retrieve the results of efficiency and
 2435 muon clusterization using a tracking algorithm to discriminate noise or gamma from muons
 2436 as muons are the only particles that pass through the full setup, leaving hits than can be used
 2437 to reconstruct their tracks.

- 2438 ● `Offline-Rate.csv`, is used to write the noise or gamma rates measured in the detector readout
 2439 partitions.

2440 Note that these 4 CSV files are created along with their *headers* (`Offline-[...]-Header.csv`
 2441 containing the names of each data columns) and are automatically merged together when the offline
 2442 analysis tool is called from the webDCS, contrary to the case where the tool is runned locally from
 2443 the terminal as the merging bash script is then not called. Thus, the resulting files, used to make
 2444 official plots, are:

- 2445 ● `Corrupted.csv`,
 2446 ● `Current.csv`,
 2447 ● `L0-EffCl.csv`.
 2448 ● `Rate.csv`.

2449 **B.3 Analysis inputs and information handling**

2450 The usage of the Offline Analysis tool as well as its output have been presented in the previous section.
 2451 It is now important to dig further and start looking at the source code and the inputs necessary
 2452 for the tool to work. Indeed, other than the raw ROOT data files that are analysed, more information
 2453 needs to be imported inside of the program to perform the analysis such as the description of the
 2454 setup inside of GIFT++ at the time of data taking (number of trolleys, of RPCs, dimensions of the
 2455 detectors, etc...) or the mapping that links the TDC channels to the coresponding RPC channels in
 2456 order to translate the TDC information into human readable data. 2 files are used to transmit all this
 2457 information:
 2458

- 2459 ● `Dimensions.ini`, that provides the necessary setup and RPC information, and
 2460 ● `ChannelsMapping.csv`, that gives the link between the TDC and RPC channels as well as the
 2461 *mask* for each channel (masked or not?).

2462 **B.3.1 Dimensions file and InFile parser**

2463 This input file, present in every data folder, allows the analysis tool to know of the number of active
 2464 trolleys, the number of active RPCs in those trolleys, and the details about each RPCs such as
 2465 the number of RPC gaps, the number of pseudo-rapidity partitions (for CMS-like prototypes), the
 2466 number of strips per partion or the dimensions. To do so, there are 3 types of groups in the INI file
 2467 architecture. A first general group, appearing only once at the head of the document, gives information
 2468 about the number of active trolleys as well as their IDs, as presented in Source Code B.1. For

2469 each active trolley, a group similar to Source Code B.2 can be found containing information about
 2470 the number of active detectors in the trolley and their IDs. Each trolley group as a `Tt` name format,
 2471 where `t` is the trolley ID. Finally, for each detector stored in slots of an active trolley, there is a group
 2472 providing information about their names and dimensions, as shown in Source Code B.3. Each slot
 2473 group as a `TtSs` name format, where `s` is the slot ID of trolley `t` where the active RPC is hosted.

```
2474 [General]
2475 nTrolleys=2
  TrolleysID=13
```

2476 *Source Code B.1: Example of `[General]` group as might be found in `Dimensions.ini`. In Gif++, only 2 trolleys are available to hold RPCs and place them inside of the bunker for irradiation. The IDs of the trolleys are written in a single string as "13" and then read character by character by the program.*

```
2477 [T1]
  nSlots=4
  SlotsID=1234
```

2478 *Source Code B.2: Example of trolley group as might be found in `Dimensions.ini`. In this example, the file tells that there are 4 detectors placed in the holding slots of the trolley `T1` and that their IDs, written as a single string variable, are 1, 2, 3 and 4.*

```
2479 [T1S1]
  Name=RE2-2-NPD-BARC-8
  Partitions=3
  Gaps=3
  Gap1=BOT
  Gap2=TN
  Gap3=TW
  AreaGap1=11694.25
  AreaGap2=6432
  AreaGap3=4582.82
  Strips=32
  ActiveArea-A=157.8
  ActiveArea-B=121.69
  ActiveArea-C=93.03
```

2480 *Source Code B.3: Example of slot group as might be found in `Dimensions.ini`. In this example, the file provides information about a detector named `RE2-2-NPD-BARC-8`, having 3 pseudo-rapidity readout partitions and stored in slot `S1` of trolley `T1`. This is a CMS RE2-2 type of detector. This information will then be used for example to compute the rate per unit area calculation.*

2481 This information is readout and stored in a C++ object called `IniFile`, that parses the information
 2482 in the INI input file and stores it into a local buffer for later use. This INI parser is the exact same
 2483 one that was previously developed for the Gif++ DAQ and described in Appendix A.5.2.

2484 B.3.2 TDC to RPC link file and Mapping

2485 The same way the INI dimension file information is stored using `map`, the channel mapping and mask
 2486 information is stored and accessed through `map`. First of all, the mapping CSV file is organised into
 2487 3 columns separated by tabulations (and not by commas, as expected for CSV files as it is easier using
 2488 streams to read tab or space separated data using C++):

2489

2490 `RPC_channel` `TDC_channel` `mask`

2491 using as formatting for each field:

2492 `TSCCC` `TCCC` `M`

2494 `TSCCC` is a 5-digit integer where `T` is the trolley ID, `s` the slot ID in which the RPC is held insite
 2495 the trolley `T` and `ccc` is the RPC channel number, or *strip* number, that can take values up to
 2496 3-digits depending on the detector,

2497 `TCCC` is a 4 digit integer where `T` is the TDC ID, `ccc` is the TDC channel number that can take values
 2498 in between 0 and 127, and

2499 `M` is a 1-digit integer indicating if the channel should be considered (`M = 1`) or discarded (`M = 0`)
 2500 during analysis.

2501 This mapping and masking information is readout and stored thanks to the object `Mapping`, pre-
 2502 sented in Source Code B.4. Similarly to `IniFile` objects, this class has private methods. The first
 2503 one, `Mapping::CheckIfNewLine()` is used to find the newline character '`\n`' or return character
 2504 '`\r`' (depending on which kind of operating system interacted with the file). This is used for the
 2505 simple reason that the masking information has been introduced only during the year 2017 but the
 2506 channel mapping files exist since 2015 and the very beginning of data taking at GIF++. This means
 2507 that in the older data folders, before the upgrade, the channel mapping file only had 2 columns, the
 2508 RPC channel and the TDC channel. For compatibility reasons, this method helps controling the
 2509 character following the readout of the 2 first fields of a line. In case any end of line character is
 2510 found, no mask information is present in the file and the default `M = 1` is used. On the contrary, if
 2511 the next character was a tabulation or a space, the mask information is present.

2512 Once the 3 fields have been readout, the second private method `Mapping::CheckIfTDCCh()` is
 2513 used to control that the TDC channel is an existing TDC channel. Finally, the information is stored
 2514 into 3 different maps (`Link`, `ReverseLink` and `Mask`) thanks to the public method `Mapping::Read()`.
 2515 `Link` allows to get the RPC channel by knowing the TDC channel while `ReverseLink` does the op-
 2516 posite by returning the TDC channel by knowing the RPC channel. Finally, `Mask` returns the mask
 2517 associated to a given RPC channel.

```

2518 typedef map<Uint,Uint> MappingData;

2519 class Mapping {
2520     private:
2521         bool          CheckIfNewLine(char next);
2522         bool          CheckIfTDCCh(Uint channel);
2523         string        FileName;
2524         MappingData  Link;
2525         MappingData  ReverseLink;
2526         MappingData  Mask;
2527         int           Error;
2528
2529     public:
2530         Mapping();
2531         Mapping(string baseName);
2532         ~Mapping();
2533
2534         void SetFileName(const string filename);
2535         int  Read();
2536         Uint GetLink(Uint tdcchannel);
2537         Uint GetReverse(Uint rpcchannel);
2538         Uint GetMask(Uint rpcchannel);
2539     };

```

2520 *Source Code B.4: Description of C++ object Mapping used as a parser for the channel mapping and mask file.*

2521 B.4 Description of GIF++ setup within the Offline Analysis tool

2522 In the previous section, the tool input files have been discussed. The dimension file information is
 2523 stored in a map hosted by the `IniFile` object. But this information is then used to create a series of
 2524 new objects that helps defining the GIF++ infrastructure directly into the Offline Analysis. Indeed,
 2525 from the `RPC`, to the more general `Infrastructure`, every element of the GIF++ infrastrucutre is
 2526 recreated for each data analysis based on the information provided in input. All this information
 2527 about the infrastructure will be used to assign each hit signal to a specific strip channel of a specific
 2528 detector, and having a specific active area. This way, rate per unit area calculation is possible.
 2529

2530 B.4.1 RPC objects

2531 `RPC` objects have been developped to represent physical active detectors in GIF++ at the moment
 2532 of data taking. Thus, there are as many `RPC` objects created during the analysis than there were
 2533 active RPCs tested during a run. Each `RPC` hosts the information present in the corresponding INI
 2534 slot group, as shown in B.3, and organises it using a similar architecture. This can be seen from
 2535 Source Code B.5.

2536 To make the object more compact, the lists of gap labels, of gap active areas and strip active
 2537 areas are stored into `vector` dynamical containers. `RPC` objects are always contructed thanks to the
 2538 dimension file information stored into the `IniFILE` and their ID, using the format `TtSs`. Using the
 2539 `RPC` ID, the constructor calls the methods of `IniFILE` to initialise the `RPC`. The other constructors
 2540 are not used but exist in case of need. Finally, some getters have been written to access the different
 2541 private parameters storing the detector information.

```

2542 class RPC{
2543     private:
2544         string      name;           //RPC name as in webDCS database
2545         Uint        nGaps;          //Number of gaps in the RPC
2546         Uint        nPartitions;    //Number of partitions in the RPC
2547         Uint        nStrips;        //Number of strips per partition
2548         vector<string> gaps;       //List of gap labels (BOT, TOP, etc...)
2549         vector<float>  gapGeo;        //List of gap active areas
2550         vector<float>  stripGeo;      //List of strip active areas
2551
2552     public:
2553         RPC();
2554         RPC(string ID, IniFile* geofile);
2555         RPC(const RPC& other);
2556         ~RPC();
2557         RPC& operator=(const RPC& other);
2558
2559         string GetName();
2560         Uint GetNGaps();
2561         Uint GetNPartitions();
2562         Uint GetNStrips();
2563         string GetGap(Uint g);
2564         float GetGapGeo(Uint g);
2565         float GetStripGeo(Uint p);
2566     };

```

2544 *Source Code B.5: Description of C++ objects RPC that describe each active detectors used during data taking.*

2545 B.4.2 Trolley objects

2546 Trolley objects have been developped to represent physical active trolleys in GIFT++ at the moment
2547 of data taking. Thus, there are as many trolley objects created during the analysis than there were
2548 active trolleys hosting tested RPCs during a run. Each Trolley hosts the information present in the
2549 corresponding INI trolley group, as shown in B.2, and organises it using a similar architecture. In
2550 addition to the information hosted in the INI file, these object have a dynamical container of RPC
2551 objects, representing the active detectors the active trolley was hosting at the time of data taking.
2552 This can been seen from Source Code B.6.

2553 Trolley objects are always contructed thanks to the dimension file information stored into the
2554 IniFILE and their ID, using the format Tt. Using the Trolley ID, the constructor calls the methods
2555 of IniFILE to initialise the Trolley. Retrieving the information of the RPC IDs via SlotsID, a new
2556 RPC is constructed and added to the container RPCs for each character in the ID string. The other
2557 constructors are not used but exist in case of need. Finally, some getters have been written to access
2558 the different private parameters storing the trolley and detectors information.

```

2559
class Trolley{
    private:
        Uint          nSlots; //Number of active RPCs in the considered trolley
        string        SlotsID; //Active RPC IDs written into a string
        vector<RPC*> RPCs;   //List of active RPCs

    public:
        //Constructors, destructor and operator =
        Trolley();
        Trolley(string ID, IniFile* geofile);
        Trolley(const Trolley& other);
        ~Trolley();
        Trolley& operator=(const Trolley& other);

        //Get GIFTrolley members
        Uint  GetNSlots();
        string GetSlotsID();
        Uint   GetSlotID(Uint s);

        //Manage RPC list
        RPC*  GetRPC(Uint r);
        void  DeleteRPC(Uint r);

        //Methods to get members of RPC objects stored in RPCs
        string GetName(Uint r);
        Uint   GetNGaps(Uint r);
        Uint   GetNPartitions(Uint r);
        Uint   GetNStrips(Uint r);
        string GetGap(Uint r, Uint g);
        float  GetGapGeo(Uint r, Uint g);
        float  GetStripGeo(Uint r, Uint p);
    };

```

Source Code B.6: Description of C++ objects `Trolley` that describe each active trolley used during data taking.

2562 B.4.3 Infrastructure object

2563 The `Infrastructure` object has been developped to represent the GIFT++ bunker area dedicated to
 2564 CMS RPC experiments. With this very specific object, all the information about the CMS RPC
 2565 setup within GIFT++ at the moment of data taking is stored. It hosts the information present in the
 2566 corresponding INI general group, as shown in B.1, and organises it using a similar architecture. In
 2567 addition to the information hosted in the INI file, this object have a dynamical container of `Trolley`
 2568 objects, representing the active tolleys in GIFT++ area. This can be seen from Source Code B.7.

2569 The `Infrastructure` object is always contructed thanks to the dimension file information stored
 2570 into the `IniFILE`. Retrieving the information of the trolley IDs via `TrolleysID`, a new `Trolley` is
 2571 constructed and added to the container `Trolleys` for each character in the ID `string`. By extension,
 2572 it is easy to understand that the process described in Section B.4.2 for the construction of RPCs
 2573 takes place when a trolley is constructed. The other constructors are not used but exist in case of
 2574 need. Finally, some getters have been written to access the different private parameters storing the
 2575 infrastructure, tolleys and detectors information.

```

2576
class Infrastructure {
    private:
        Uint             nTrolleys;   //Number of active Trolleys in the run
        string          TrolleysID;  //Active trolley IDs written into a string
        vector<Trolley*> Trolleys;  //List of active Trolleys (struct)

    public:
        //Constructors and destructor
        Infrastructure();
        Infrastructure(IniFile* geofile);
        Infrastructure(const Infrastructure& other);
        ~Infrastructure();
        Infrastructure& operator=(const Infrastructure& other);

        //Get Infrastructure members
        Uint  GetNTrolleys();
        string GetTrolleysID();
        Uint   GetTrolleyID(Uint t);

2577
        //Manage Trolleys
        Trolley* GetTrolley(Uint t);
        void     DeleteTrolley(Uint t);

        //Methods to get members of GIFTrolley objects stored in Trolleys
        Uint  GetNSlots(Uint t);
        string GetSlotsID(Uint t);
        Uint   GetSlotID(Uint t, Uint s);
        RPC*  GetRPC(Uint t, Uint r);

        //Methods to get members of RPC objects stored in RPCs
        string GetName(Uint t, Uint r);
        Uint   GetNGaps(Uint t, Uint r);
        Uint   GetNPartitions(Uint t, Uint r);
        Uint   GetNStrips(Uint t, Uint r);
        string GetGap(Uint t, Uint r, Uint g);
        float  GetGapGeo(Uint t, Uint r, Uint g);
        float  GetStripGeo(Uint t, Uint r, Uint p);
};


```

Source Code B.7: Description of C++ object *Infrastructure* that contains the full information about CMS RPC experiment in GIF++.

2579 B.5 Handeling of data

2580 As discussed in Appendix A.4.2, the raw data as a `TTree` architecture where every entry is related to
 2581 a trigger signal provided by a muon or a random pulse, whether the goal of the data taking was to
 2582 measure the performance of the detector or the noise/gamma background respectively. Each of these
 2583 entries, referred also as events, contain a more or less full list of hits in the TDC channels to which
 2584 the detectors are connected. To this list of hits corresponds a list of time stamps, marking the arrival
 2585 of the hits within the TDC channel.

2586 The infrastructure of the CMS RPC experiment within GIF++ being defined, combining the
 2587 information about the raw data with the information provided by both the mapping/mask file and the
 2588 dimension file allows to build new physical objects that will help in computing efficiency or rates.

2589 B.5.1 RPC hits

2590 The raw data stored in the ROOT file as output of the GIFT++ DAQ, is readout by the analysis tool
 2591 using the structure `RAWData` presented in Source Code B.9 that differs from the structure presented
 2592 in Appendix A.4.2 as it is not meant to hold all of the data contained in the ROOT file. In this sense,
 2593 this structure is in the case of the offline analysis tool not a dynamical object and will only be storing
 2594 a single event contained in a single entry of the `TTree`.

```
2595
  class RPCHit {
    private:
      Uint Channel;      //RPC channel according to mapping (5 digits)
      Uint Trolley;     //0, 1 or 3 (1st digit of the RPC channel)
      Uint Station;     //Slot where is held the RPC in Trolley (2nd digit)
      Uint Strip;       //Physical RPC strip where the hit occurred (last 3
→   digits)
      Uint Partition;   //Readout partition along eta segmentation
      float TimeStamp; //Time stamp of the arrival in TDC

    public:
      //Constructors, destructor & operator =
      RPCHit();
      RPCHit(Uint channel, float time, Infrastructure* Infra);
      RPCHit(const RPCHit& other);
      ~RPCHit();
      RPCHit& operator=(const RPCHit& other);

      //Get RPCHit members
      Uint GetChannel();
      Uint GetTrolley();
      Uint GetStation();
      Uint GetStrip();
      Uint GetPartition();
      float GetTime();
    };

    typedef vector<RPCHit> HitList;
    typedef struct GIFHitList { HitList rpc[NTROLLEYS][NSLOTS][NPARTITIONS]; }
→   GIFHitList;

    bool SortHitbyStrip(RPCHit h1, RPCHit h2);
    bool SortHitbyTime(RPCHit h1, RPCHit h2);
  
```

2597 *Source Code B.8: Description of C++ object `RPCHit`.*

```
2598
  struct RAWData{
    int iEvent;        //Event i
    int TDCNHits;    //Number of hits in event i
    int QFlag;         //Quality flag list (1 flag digit per TDC)
    vector<Uint> *TDCCh; //List of channels giving hits per event
    vector<float> *TDCTS; //List of the corresponding time stamps
  };

```

2599 *Source Code B.9: Description of C++ structure `RAWData`.*

2600 Each member of the structure is then linked to the corresponding branch of the ROOT data tree,
 2601 as shown in the example of Source Code B.10, and using the method `GetEntry(int i)` of the ROOT
 2602 class `TTree` will update the state of the members of `RAWData`.

```

2603   TTree* dataTree = (TTree*)dataFile.Get("RAWData");
2604   RAWData data;
2605
2606   dataTree->SetBranchAddress("EventNumber", &data.iEvent);
2607   dataTree->SetBranchAddress("number_of_hits", &data.TDCNHits);
2608   dataTree->SetBranchAddress("Quality_flag", &data.QFlag);
2609   dataTree->SetBranchAddress("TDC_channel", &data.TDCCh);
2610   dataTree->SetBranchAddress("TDC_TimeStamp", &data.TDCTS);

```

2605 *Source Code B.10: Example of link in between RAWData and TTree.*

2606 The data is then analysed entry by entry and to each element of the TDC channel list, a `RPCHit` is
 2607 constructed by linking each TDC channel to the corresponding RPC channel thanks to the `Mapping`
 2608 object. The information carried by the RPC channel format allows to easily retrieve the trolley and
 2609 slot from which the hit was recorded (see section B.3.2). Using these 2 values, the readout partition
 2610 can be found by knowing the strip channel and comparing it with the number of partitions and strips
 2611 per partition stored into the `Infrastructure` object.

2612 Thus `RPCHit` objects are then stored into 3D dynamical list called `GIFHitList` (Source Code B.9)
 2613 where the 3 dimensions refer to the 3 layers of the readout in `GIF++` : in the bunker there are *trolleys*
 2614 (τ) holding detectors in *slots* (s) and each detector readout is divided into 1 or more pseudo-rapidity
 2615 *partitions* (p). Using these 3 information allows to assign an address to each readout partition and
 2616 this address will point to a specific hit list.

2617

2618 B.5.2 Clusters of hits

2619 All the hits contained in the ROOT file have been sorted into the different hit lists through the
 2620 `GIFHitList`. At this point, it is possible to start looking for clusters. A cluster is a group of adjacent
 2621 strips getting hits within a time window of 25 ns. These strips are then assumed to be part of the same
 2622 physical avalanche signal generated by a muon passing through the chamber or by the interaction of
 2623 a gamma stopping into the electrodes of the RPCs.

2624 To keep the cluster information, `RPCCluster` objects have been defined as shown in Source
 2625 Code B.11. Using the information of each individual `RPCHit` taken out of the hit list, it stores
 2626 the cluster size (number of adjacent strips composing the cluster), the first and last hit, the center for
 2627 spatial reconstruction and finally the start and stop time stamps as well as te time spread in between
 2628 the first and last hit.

```

2629
class RPCCluster{
    private:
        Uint ClusterSize; //Size of cluster #ID
        Uint FirstStrip; //First strip of cluster #ID
        Uint LastStrip; //Last strip of cluster #ID
        float Center; //Center of cluster #ID ((first+last)/2)
        float StartStamp; //Time stamp of the earliest hit of cluster #ID
        float StopStamp; //Time stamp of the latest hit of cluster #ID
        float TimeSpread; //Time difference between earliest and latest hits
                           //of cluster #ID
    public:
        //Constructors, destructor & operator =
        RPCCluster();
        RPCCluster(HitList List, Uint cID, Uint cSize, Uint first, Uint firstID);
        RPCCluster(const RPCCluster& other);
        ~RPCCluster();
        RPCCluster& operator=(const RPCCluster& other);

        //Get Cluster members
        Uint GetID();
        Uint GetSize();
        Uint GetFirstStrip();
        Uint GetLastStrip();
        float GetCenter();
        float GetStart();
        float GetStop();
        float GetSpread();
    };

typedef vector<RPCCluster> ClusterList;

//Other functions to build cluster lists out of hit lists
void BuildClusters(HitList &cluster, ClusterList &clusterList);
void Clusterization(HitList &hits, TH1 *hcSize, TH1 *hcMult);

```

2631 *Source Code B.11: Description of C++ object Cluster.*

2632 To investigate the hit list of a given detector partition, the function `Clusterization()` defined
 2633 in `include/Cluster.h` needs the hits in the list to be time sorted. This is achieved by calling func-
 2634 tion `sort()` of library `<algorithm>` using the comparator `SortHitbyTime(RPCHit h1, RPCHit h2)`
 2635 defined in `include/RPCHit.h` that returns `true` if the time stamp of hit `h1` is lower than that of `h2`.
 2636 A first isolation of strips is made only based on time information. All the hits within the 25 ns win-
 2637 dow are taken separately from the rest. Then, this sub-list of hits is sorted this time by ascending
 2638 strip number, using this time the comparator `SortHitbyStrip(RPCHit h1, RPCHit h2)`. Finally, the
 2639 groups of adjacent strips are used to construct `RPCCluster` objects that are then stored in a temporary
 2640 list of clusters that is at the end of the process used to know how many clusters were reconstructed
 2641 and to fill their sizes into an histogram that will allows to know the mean size of muon or gamma
 2642 clusters.

2643

2644 B.6 DAQ data Analysis

2645 All the ingredients to analyse GIF++ data have been defined. This section will focus on the different
 2646 part of the analysis performed on the data, from determining the type of data the tool is dealing with

2647 to calculating the rate in each detector or reconstructing muon or gamma clusters.

2648 B.6.1 Determination of the run type

2649 In GIF++, both the performance of the detectors in detecting muons in an irradiated environment and
 2650 the gamma background can be independantly measured. These corresponds to different run types
 2651 and thus, to different TDC settings giving different data to look at.

2652

2653 In the case of performance measurements, the trigger for data taking is provided by the coïncidence
 2654 of several scintillators when muons from the beam passing through the area are detected. Data
 2655 is collected in a 600 ns wide window around the arrival of muons in the RPCs. The expected time
 2656 distribution of hits is shown in Figure B.1a. The muon peak is clearly visible in the center of the
 2657 distribution and is to be extracted from the gamma background that composes the flat part of the
 2658 distribution.

2659 On the other hand, gamma background or noise measurements are focussed on the non muon
 2660 related physics and the trigger needs to be independant from the muons to give a good measurement
 2661 of the gamma/noise distribution as seen by the detectors. The trigger is then provided by a pulse
 2662 generator at a frequency of 300 Hz whose pulse is not likely to be on time with a muon. In order
 2663 to increase the integrated time without increasing the acquisition time too much, the width of the
 2664 acquisition windows are increased to 10 μ s. The time distribution of the hits is expected to be flat, as
 2665 shown by Figure B.1b.

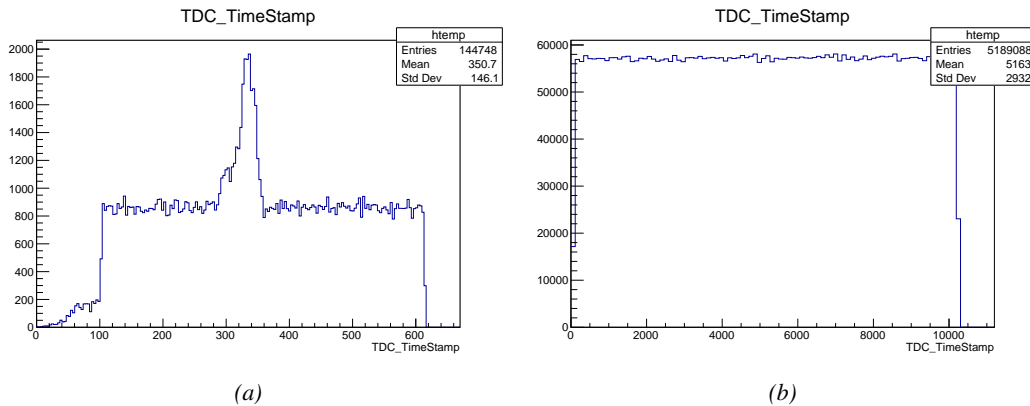


Figure B.1: Example of expected hit time distributions in the cases of efficiency (Figure B.1a) and noise/gamma rate per unit area (Figure B.1b) measurements as extracted from the raw ROOT files. The unit along the x-axis corresponds to ns. The fact that "the" muon peak is not well defined in Figure B.1a is due to the contribution of all the RPCs being tested at the same time that don't necessarily have the same signal arrival time. Each individual peak can have an offset with the ones of other detectors. The inconsistency in the first 100 ns of both time distributions is an artefact of the TDCs and are systematically rejected during the analysis.

2666 The ROOT files include a TTree called RunParameters containing, among other things, the in-
 2667 formation related to the type of run. The run type can then be accessed as described by Source
 2668 Code B.12 and the function IsEfficiencyRun() is then used to determine if the run file is an effi-
 2669 ciency run or, on the contrary, another type of run (noise or gamma measurement).

```

2670
2671     TTree* RunParameters = (TTree*)dataFile.Get("RunParameters");
2672     TString* RunType = new TString();
2673     RunParameters->SetBranchAddress("RunType", &RunType);
2674     RunParameters->GetEntry(0);

```

2672 *Source Code B.12: Access to the run type contained in TTree* RunParameters.*

2673 Finally, the data files will have a slightly different content whether it was collected before or after
 2674 October 2017 and the upgrade of the DAQ software that brought a new information into the ROOT
 2675 output. This is discussed in Appendix A.4.3 and implies that the analysis will differ a little depending
 2676 on the data format. Indeed, as no information on the data quality is stored, in older data files, the cor-
 2677 rections for missing events has to be done at the end of the analysis. The information about the type
 2678 of data format is stored in the variable **bool** `isNewFormat` by checking the list of branches contained
 2679 in the data tree via the methods `TTree::GetListOfBranches()` and `TCollection::Contains()`.

2680 **B.6.2 Beam time window calculation for efficiency runs**

2681 Knowing the run type is important first of all to know the width of the acquisition window to be used
 2682 for the rate calculation and finally to be able to seek for muons. Indeed, the peak that appears in the
 2683 time distribution for each detectors is then fitted to extract the most probable time window in which
 2684 the tool should look for muon hits. The data outside of this time window is then used to evaluate the
 2685 noise or gamma background the detector was subjected to during the data taking. Computing the
 2686 position of the peak is done calling the function `SetBeamWindow()` defined in file `src/RPCHit.cc` that
 2687 loops a first time on the data. The data is first sorted in a 3D array of 1D histograms (`GIFH1Array`, see
 2688 `include/types.h`). Then the location of the highest bin is determined using `TH1::GetMaximumBin()`
 2689 and is used to define a window in which a gaussian fit will be applied to compute the peak width.
 2690 This window is a 80 ns defined by Formula B.1 around the central bin.

$$t_{center}(ns) = bin \times width_{bin}(ns) \quad (\text{B.1a})$$

$$[t_{low}; t_{high}] = [t_{center} - 40; t_{center} + 40] \quad (\text{B.1b})$$

2691 Before the fit is performed, the average number of noise/gamma hits per bin is evaluated using
 2692 the data outside of the fit window. Excluding the first 100 ns, the average number of hits per bin
 2693 due to the noise or gamma is defined by Formula B.2 after extracting the amount of hits in the time
 2694 windows $[100; t_{low}]$ and $[t_{high}; 600]$ thanks to the method `TH1::Integral()`. This average number
 2695 of hits is then subtracted to every bin of the 1D histogram, in order to *clean* it from the noise or
 2696 gamma contribution as much as possible to improve the fit quality. Bins where $\langle n_{hits} \rangle$ is greater
 2697 than the actual bin content are set to 0.

$$\Delta t_{noise}(ns) = 600 \overbrace{-t_{high} + t_{low}}^{-80ns} - 100 = 420ns \quad (\text{B.2a})$$

$$\langle n_{hits} \rangle = width_{bin}(ns) \times \frac{\sum_{t=100}^{t_{low}} + \sum_{t=t_{high}}^{600}}{\Delta t_{noise}(ns)} \quad (\text{B.2b})$$

2698 Finally, the fit parameters are extracted and saved for each detector in 3D arrays of **float**
 2699 (`muonPeak`, see `include/types.h`), a first one for the mean arrival time of the muons, `PeakTime`,

2700 and a second one for the width of the peak, `PeakWidth`. The width is defined as 6σ of the gaussian
 2701 fit. The same settings are applied to every partitions of the same detector. To determine which one
 2702 of the detector's partitions is directly illuminated by the beam, the peak height of each partition is
 2703 compared and the highest one is then used to define the peak settings.

2704 **B.6.3 Data loop and histogram filling**

2705 3D arrays of histogram are created to store the data and display it on the DQM of GIF++ webDCS
 2706 for the use of shifters. These histograms, presented in section B.2.1.1, are filled while looping on
 2707 the data. Before starting the analysis loop, it is necessary to control the entry quality for the new
 2708 file formats featuring `QFlag`. If the `QFlag` value for this entry shows that 1 TDC or more have a
 2709 `CORRUPTED` flag, then this event is discarded. The loss of statistics is low enough to be neglected.
 2710 `QFlag` is controled using the function `IsCorruptedEvent()` defined in `src/utils.cc`. As explained
 2711 in Appendix A.4.3, each digit of this integer represent a TDC flag that can be 1 or 2. Each 2 is
 2712 the sign of a `CORRUPTED` state. Then, the data is accessed entry by entry in the ROOT `TTree` using
 2713 `RAWData` and each hit in the hit list is assigned to a detector channel and saved in the corresponding
 2714 histograms. In the first part of the analysis, in which the loop over the ROOT file's content is
 2715 performed, the different steps are:

2716 **1- RPC channel assignment and control:** a check is done on the RPC channel extracted thanks
 2717 to the mapping via the method `Mapping::GetLink()`. If the channel is not initialised and is 0, or if
 2718 the TDC channel was greater than 5127, the hit is discarded. This means there was a problem in the
 2719 mapping. Often a mapping problem leads to the crash of the offline tool.

2720 **2- Creation of a `RPCHit` object:** to easily get the trolley, slot and partition in which the hit has
 2721 been assigned, this object is particularly helpful.

2722 **3- General histograms are filled:** the hit is filled into the time distribution and the general hit
 2723 distribution histograms, and if the arrival time is within the first 100 ns, it is discarded and nothing
 2724 else happens and the loop proceeds with the next hit in the list.

2725 **4- Multiplicity counter:** the hit multiplicity counter of the corresponding detectors incremented.

2726 **5-a- Efficiency runs - Is the hit within the peak window? :** if the peak is contained in the peak
 2727 window previously defined in section B.6.2, the hit is filled into the beam hit profile histogram of
 2728 the corresponding chamber, added into the list of muon hits and increments the counter of *in time*
 2729 hits. The term *in time* here refers to the hits that are likely to be muons by arriving in the expected
 2730 time window. If the hit is outside of the peak window, it is filled into the noise profile histogram
 2731 of the corresponding detector, added into the list of noise/gamma hits and increments the counter of
 2732 noise/gamma hits.

2733 **5-b- Noise/gamma rate runs - Noise histograms are filled:** the hit is filled into the noise profile
 2734 histogram of the corresponding detector, added into the list of noise/gamma hits and increments the
 2735 counter of noise/gamma hits.

2736

2737 After the loop on the hit list of the entry is over, the next step is to clusterize the 3D lists filled
 2738 in the previous steps. A 3D loop is then started over the active trolley, slot and RPC partitions to
 2739 access these objects. Each `NoiseHitList` and `MuonHitList`, in case of efficiency run, are clusterized
 2740 as described in section B.5.2. There corresponding cluster size and multiplicity histograms are filled
 2741 at the end of the clustering process. Then, the efficiency histogram is filled in case of efficiency run.
 2742 The selection is simply made by checking whether the RPC detected signals in the peak window
 2743 during this event. Nevertheless, it is useful to highlight that at this level, it is not possible yet to
 2744 discriminate in between a muon hit and noise or gamma hit. Thus, `MuonCSize_H`, `MuonCMult_H`
 2745 and `Efficiency0_H` are subjected to noise and gamma contamination. This contamination will be
 2746 estimated and corrected at the moment the results will be written into output CSV files. Finally, the
 2747 loop ends on the filling of the general hit multiplicity histogram.

2748 **B.6.4 Results calculation**

2749 As mentioned in section B.2.1, the analysis of DAQ data provides the user with 3 CSV files and
 2750 a ROOT file associated to each and every ROOT data file. The fourth CSV file is provided by the
 2751 extraction of the CEAN main frame data monitored during data taking and will be discussed later.
 2752 After looping on the data in the previous part of the analysis macro, the output files are created and a
 2753 3D loop on each RPC readout partitions is started to extract the histograms parameters and compute
 2754 the final results.

2755

2756 **B.6.4.1 Rate normalisation**

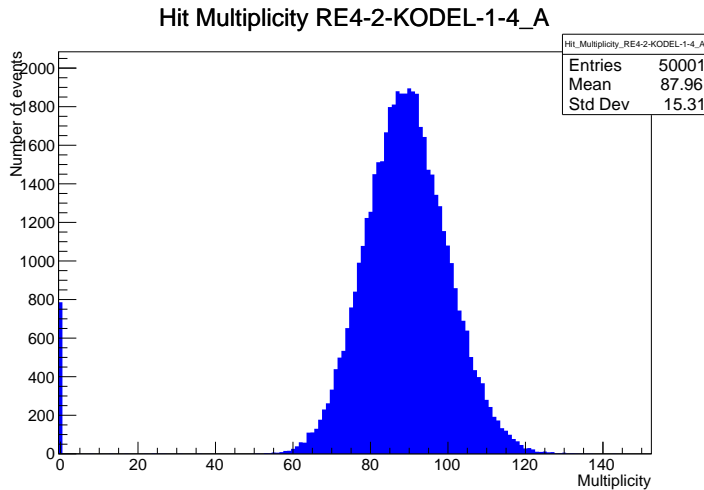


Figure B.2: The effect of the quality flag is explained by presenting the reconstructed hit multiplicity of a data file without `Quality_flag`. The artificial high content of bin 0 is the effect of corrupted data.

2757 To analyse old data format files, not containing any quality flag, it is needed to estimate the amount
 2758 of corrupted data via a fit as the corrupted data will always fill events with a fake "0 multiplicity".
 2759 Indeed, as no hits were stored in the DAQ ROOT files, these events artificially contribute to fill
 2760 the bin corresponding to a null multiplicity, as shown in Figure B.2. In the case the mean of the

hit multiplicity distribution is high, the contribution of the corrupted data can easily be evaluated for later correction by comparing the level of the bin at multiplicity 0 and of a skew fit curve that should indicate a value consistent with 0. A skew fit has been chosen over a Poisson fit as it was giving better results for lower mean multiplicity values. Nevertheless, for low irradiation cases, as explained in Appendix A.4.3, the hit multiplicity distribution mean is, on the contrary, rather small and the probability to record events without hits can't be considered small anymore, leading to a difficult and non-reliable estimation of the corruption. As can be seen in Source Code B.13, conditions have been applied to prevent bad fits and wrong corruption estimation in cases where :

- The difference in between the data for multiplicity 1 and the corresponding fit value should be lower than 1% of the total amount of data : $\frac{|n_{m=1} - sk(1)|}{N_{tot}} < 0.01$ where $n_{m=1}$ is the number of entries with multiplicity 1, $sk(1)$ the value of the skew fit, as defined by Formula 5.3, for multiplicity 1 and N_{tot} the total number of entries.

- The amount of data contained in the multiplicity 0 bin should not exceed 40% : $\frac{n_{m=0}}{N_{tot}} \leq 0.4$ where $n_{m=0}$ is the number of entries with multiplicity 0. This number has been determined to be the maximum to be able to separate the excess of data due to corruption from the hit multiplicity distribution.

Those 2 conditions need to be fulfilled to estimate the corruption of old data format files. If the fit was successful, the level of corruption is written in `Offline-Corrupted.csv` and the number of corrupted entries, refered as the integer `nEmptyEvent`, is subtracted from the total number of entries when the rate normalisation factor is computed as explicit in Source Code B.13. Note that for new data format files, the number of corrupted entries being set to 0, the definition of `rate_norm` stays valid.

```

2783
if(!isNewFormat){
    TF1* GaussFit = new TF1("gaussfit","[0]*exp(-0.5*((x-[1])/[2])**2)",0,Xmax);
    GaussFit->SetParameter(0,100);
    GaussFit->SetParameter(1,10);
    GaussFit->SetParameter(2,1);
    HitMultiplicity_H.rpc[T][S][p]->Fit(GaussFit,"LIQR","",0.5,Xmax);

    TF1* SkewFit = new TF1("skewfit","[0]*exp(-0.5*((x-[1])/[2])**2) / (1 +
→ exp(-[3]*(x-[4])))",0,Xmax);
    SkewFit->SetParameter(0,GaussFit->GetParameter(0));
    SkewFit->SetParameter(1,GaussFit->GetParameter(1));
    SkewFit->SetParameter(2,GaussFit->GetParameter(2));
    SkewFit->SetParameter(3,1);
    SkewFit->SetParameter(4,1);
    HitMultiplicity_H.rpc[T][S][p]->Fit(SkewFit,"LIQR","",0.5,Xmax);

    double fitValue = SkewFit->Eval(1,0,0,0);
    double dataValue = (double)HitMultiplicity_H.rpc[T][S][p]->GetBinContent(2);
    double difference = TMath::Abs(dataValue - fitValue);
    double fitTOdataVSentries_ratio = difference / (double)nEntries;
    bool isFitGOOD = fitTOdataVSentries_ratio < 0.01;

2784
    double nSinglehit = (double)HitMultiplicity_H.rpc[T][S][p]->GetBinContent(1);
    double lowMultRatio = nSinglehit / (double)nEntries;
    bool isMultLOW = lowMultRatio > 0.4;

    if(isFitGOOD && !isMultLOW){
        nEmptyEvent = HitMultiplicity_H.rpc[T][S][p]->GetBinContent(1);
        nPhysics = (int)SkewFit->Eval(0,0,0,0);
        if(nPhysics < nEmptyEvent)
            nEmptyEvent = nEmptyEvent-nPhysics;
    }
}

double corrupt_ratio = 100.*(double)nEmptyEvent / (double)nEntries;
outputCorrCSV << corrupt_ratio << '\t';

float rate_norm = 0.;
float stripArea = GIFIInfra->GetStripGeo(tr,sl,p);

if(IsEfficiencyRun(RunType)){
    float noiseWindow = BMTDCWINDOW - TIMEREJECT - 2*PeakWidth.rpc[T][S][p];
    rate_norm = (nEntries-nEmptyEvent)*noiseWindow*1e-9*stripArea;
} else
    rate_norm = (nEntries-nEmptyEvent)*RDMNOISEWDW*1e-9*stripArea;

```

Source Code B.13: Definition of the rate normalisation variable. It takes into account the number of non corrupted entries and the time window used for noise calculation, to estimate the total integrated time, and the strip active area to express the result as rate per unit area.

2786 B.6.4.2 Rate and activity

2787 At this point, the strip rate histograms, StripNoiseProfile_H.rpc[T][S][p], only contain an in-
2788 formation about the total number of noise or rate hits each channel received during the data taking.
2789 As described in Source Code B.14, a loop on the strip channels will be used to normalise the content
2790 of the rate distribution histogram for each detector partitions. The initial number of hits recorded for
2791 a given bin will be extracted and 2 values will be computed:

- 2792 ● the strip rate, defined as the number of hits recorded in the bin normalised like described in
 2793 the previous section, using the variable `rate_norm`, and

- 2794 ● the strip activity, defined as the number of hits recorded in the bin normalised to the average
 2795 number of hits per bin contained in the partition histogram, using the variable `averageNhit`.
 2796 This value provides an information on the homogeneity of the detector response to the gamma
 2797 background or of the detector noise. An activity of 1 corresponds to an average response.
 2798 Above 1, the channel is more active than the average and bellow 1, the channel is less active.

```

int nNoise = StripNoiseProfile_H.rpc[T][S][p]->GetEntries();
float averageNhit = (nNoise>0) ? (float)(nNoise/nStripsPart) : 1.;

for(Uint st = 1; st <= nStripsPart; st++) {
    float stripRate =
        StripNoiseProfile_H.rpc[T][S][p]->GetBinContent(st)/rate_norm;
    float stripAct =
        StripNoiseProfile_H.rpc[T][S][p]->GetBinContent(st)/averageNhit;

    StripNoiseProfile_H.rpc[T][S][p]->SetBinContent(st,stripRate);
    StripActivity_H.rpc[T][S][p]->SetBinContent(st,stripAct);
}

```

2800 *Source Code B.14: Description of the loop that allows to set the content of each strip rate and strip activity
 channel for each detector partition.*

2801 On each detector partitions, which are readout by a single FEE, all the channels are not processed
 2802 by the same chip. Each chip can give a different noise response and thus, histograms using a chip
 2803 binning are used to investigate chip related noise behaviours. The average values of the strip rate
 2804 or activity grouped into a given chip are extracted using the using the function `GetChipBin()` and
 2805 stored in dedicated histograms as described in Source Codes B.15 and B.16 respectively.

```

float GetChipBin(TH1* H, Uint chip){
    Uint start = 1 + chip*NSTRIPSCHIP;
    int nActive = NSTRIPSCHIP;
    float mean = 0.;

    for(Uint b = start; b <= (chip+1)*NSTRIPSCHIP; b++) {
        float value = H->GetBinContent(b);
        mean += value;
        if(value == 0.) nActive--;
    }

    if(nActive != 0) mean /= (float)nActive;
    else mean = 0.;

    return mean;
}

```

2808 *Source Code B.15: Function used to compute the content of a bin for an histogram using chip binning.*

```

2809   for(UInt ch = 0; ch < (nStripsPart/NSTRIPSCHIP); ch++) {
    ChipMeanNoiseProf_H.rpc[T][S][p]->
        SetBinContent(ch+1,GetChipBin(StripNoiseProfile_H.rpc[T][S][p],ch));
    ChipActivity_H.rpc[T][S][p]->
        SetBinContent(ch+1,GetChipBin(StripActivity_H.rpc[T][S][p],ch));
}

```

Source Code B.16: Description of the loop that allows to set the content of each chip rate and chip activity bins for each detector partition knowing the information contained in the corresponding strip distribution histograms.

The activity variable is used to evaluate the homogeneity of the detector response to background or of the detector noise. The homogeneity h_p of each detector partition can be evaluated using the formula $h_p = \exp(-\sigma_p^R / \langle R \rangle_p)$, where $\langle R \rangle_p$ is the partition mean rate and σ_p^R is the rate standard deviation calculated over the partition channels. The more homogeneously the rates are distributed and the smaller will σ_p^R be, and the closer to 1 will h_p get. On the contrary, if the standard deviation of the channel's rates is large, h_p will rapidly get to 0. This value is saved into histograms as shown in Source Code B.17 and could in the future be used to monitor through time, once extracted, the evolution of every partition homogeneity. This could be of great help to understand the apparition of eventual hot spots due to ageing of the chambers subjected to high radiation levels. The monitored homogeneity information could then be combined with a monitoring of the activity of each individual channel in order to have a finer information. Monitoring tools have been suggested and need to be developed for this purpose.

```

2823
float MeanPartSDev = GetTH1StdDev(StripNoiseProfile_H.rpc[T][S][p]);
float strip_homog = (MeanPartRate==0)
    ? 0.
    : exp(-MeanPartSDev/MeanPartRate);
StripHomogeneity_H.rpc[T][S][p]->Fill("exp -#left(#frac{\#sigma_{Strip}
    \rightarrow Rate}{\#mu_{Strip Rate}}\#right)",strip_homog);
StripHomogeneity_H.rpc[T][S][p]->GetYaxis()->SetRangeUser(0.,1.);

2824
float ChipStDevMean = GetTH1StdDev(ChipMeanNoiseProf_H.rpc[T][S][p]);
float chip_homog = (MeanPartRate==0)
    ? 0.
    : exp(-ChipStDevMean/MeanPartRate);
ChipHomogeneity_H.rpc[T][S][p]->Fill("exp -#left(#frac{\#sigma_{Chip}
    \rightarrow Rate}{\#mu_{Chip Rate}}\#right)",chip_homog);
ChipHomogeneity_H.rpc[T][S][p]->GetYaxis()->SetRangeUser(0.,1.);


```

Source Code B.17: Storage of the homogeneity into dedicated histograms.

B.6.4.3 Strip masking tool

The offline tool is automatically called at the end of each data taking to analyse the data and offer the shifter DQM histograms to control the data quality. After the histograms have been published online in the DQM page, the shifter can decide to mask noisy or dead channels that will contribute to bias the final rate calculation by editing the mask column of `ChannelsMapping.csv` as can be seen in Figure B.3.

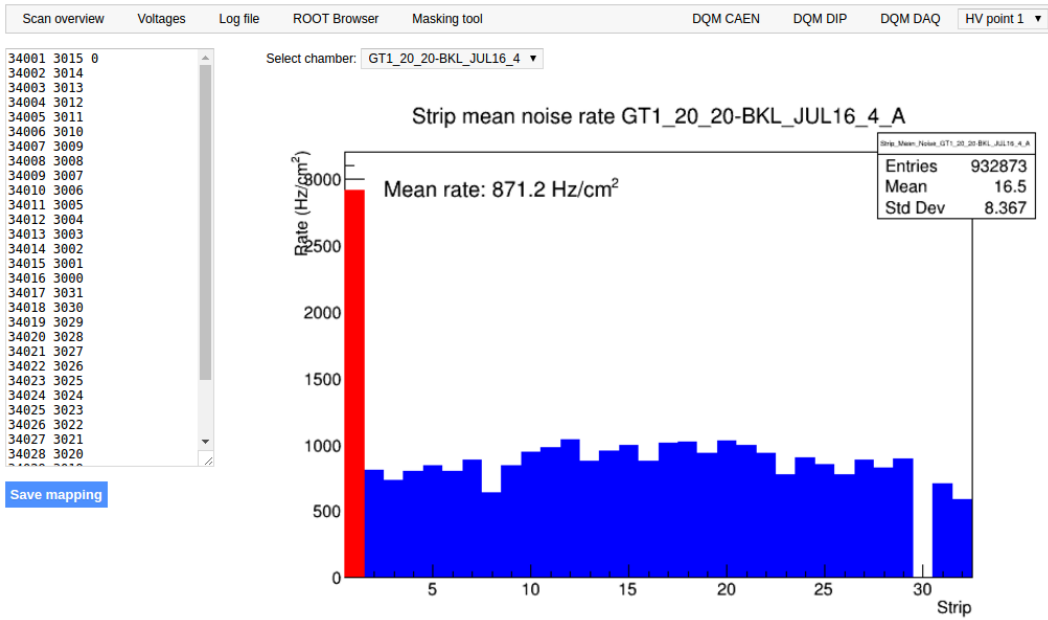


Figure B.3: Display of the masking tool page on the webDCS. The window on the left allows the shifter to edit ChannelsMapping.csv. To mask a channel, it only is needed to set the 3rd field corresponding to the strip to mask to 0. It is not necessary for older mapping file formats to add a 1 for each strip that is not masked as the code is versatile and the default behaviour is to consider missing mask fields as active strips. The effect of the mask is directly visible for noisy channels as the corresponding bin turns red. The global effect of masking strips will be an update of the rate value showed on the histogram that will take into consideration the rejected channels.

2832 From the code point of view, the function `GetTH1Mean()` is used to retrieve the mean rate par-
 2833 tition by partition after the rates have been calculated strip by strip and filled into the histograms
 2834 `StripNoiseProfile_H.rpc[T][S][p]`, as described through Source Code B.18.

2835 Once the mask for each rejected channel has been updated, the shifter can manually run the of-
 2836 fline tool again to update the DQM plots, now including the masked strips, as well the rate results
 2837 written in the output CSV file `Offline-Rate.csv`. If not done during the shifts, the strip masking
 2838 procedure needs to be carefully done by the person in charge of data analysis on the scans that were
 2839 selected to produce the final results.

```

2840
float GetTH1Mean(TH1* H) {
    int nBins = H->GetNbinsX();
    int nActive = nBins;
    float mean = 0.;

    for(int b = 1; b <= nBins; b++) {
        float value = H->GetBinContent(b);
        mean += value;
        if(value == 0.) nActive--;
    }

    if(nActive != 0) mean /= (float)nActive;
    else mean = 0.;

    return mean;
}

```

Source Code B.18: The function `GetTH1Mean()` is used to return the mean along the y-axis of TH1 histograms containing rate information. In order to take into account masked strips whose rate is set to 0, the function looks for masked channels and decrement the number of active channels for each null value found.

2843 B.6.4.4 Output CSV files filling

2844 All the histograms have been filled. Parameters will then be extracted from them to compute the
 2845 final results that will later be used to produce plots. Once the results have been computed, the very
 2846 last step of the offline macro is to write these values into the corresponding CSV outputs. Aside of
 2847 the file `Offline-Corrupted.csv`, 2 CSV files are being written by the macro `offlineAnalysis()`,
 2848 `Offline-Rates.csv` and `Offline-L0-EffCl.csv` that respectively contain information about noise
 2849 or gamma rates, cluster size and multiplicity, and about level 0 reconstruction of the detector effi-
 2850 ciency, muon cluster size and multiplicity. Details on the computation and file writing are respec-
 2851 tively given in Sources Codes B.19 and B.20.

2852 **Noise/gamma background variables** are computed and written in the output file for each detector
 2853 partitions. A detector average of the hit and cluster rate is also provided, as shown through Sources
 2854 Code B.19. The variables that are written for each partition are:

- 2855 • The mean partition hit rate per unit area, `MeanPartRate`, that is extracted from the histogram
 2856 `StripNoiseProfile_H` as the mean value along the y-axis, as described in section B.6.4.3. No
 2857 error is recorded for the hit rate as this is considered a single measurement. No statistical error
 2858 can be associated to it and the systematics are unknown.
- 2859 • The mean cluster size, `cSizePart`, is extracted from the histogram `NoiseCSize_H` and it's
 2860 statistical error, `cSizePartErr`, is taken to be 2σ of the total distribution.
- 2861 • The mean cluster multiplicity per trigger, `cMultPart`, is extracted from the histogram `NoiseCMult_H`
 2862 and it's statistical error, `cMultPartErr`, is taken to be 2σ of the total distribution. It is impor-
 2863 tant to point to the fact that this variable gives an information that is dependent on the buffer
 2864 window width used for each trigger for the calculation.
- 2865 • The mean cluster rate per unit area, `ClustPartRate`, is defined as the mean hit rate normalised

2866 to the mean cluster size and it's statistical error, `ClustPartRateErr`, is then obtained using the
 2867 relative statistical error on the mean cluster size.

```

for (UInt tr = 0; tr < GIFInfra->GetNTrolleys(); tr++) {
    UInt T = GIFInfra->GetTrolleyID(tr);

    for (UInt sl = 0; sl < GIFInfra->GetNSlots(tr); sl++) {
        UInt S = GIFInfra->GetSlotID(tr,sl) - 1;

        float MeanNoiseRate = 0.;
        float ClusterRate = 0.;
        float ClusterSDev = 0.;

        for (UInt p = 0; p < GIFInfra->GetNPartitions(tr,sl); p++) {
            float MeanPartRate = GetTH1Mean(StripNoiseProfile_H.rpc[T][S][p]);
            float cSizePart = NoiseCSIZE_H.rpc[T][S][p]->GetMean();
            float cSizePartErr = (NoiseCSIZE_H.rpc[T][S][p]->GetEntries()==0)
                ? 0.
                : 2*NoiseCSIZE_H.rpc[T][S][p]->GetStdDev() /
                    sqrt(NoiseCSIZE_H.rpc[T][S][p]->GetEntries());
            float cMultPart = NoiseCMult_H.rpc[T][S][p]->GetMean();
            float cMultPartErr = (NoiseCMult_H.rpc[T][S][p]->GetEntries()==0)
                ? 0.
                : 2*NoiseCMult_H.rpc[T][S][p]->GetStdDev() /
                    sqrt(NoiseCMult_H.rpc[T][S][p]->GetEntries());
            float ClustPartRate = (cSizePart==0) ? 0.
                : MeanPartRate/cSizePart;
            float ClustPartRateErr = (cSizePart==0) ? 0.
                : ClustPartRate * cSizePartErr/cSizePart;

            outputRateCSV << MeanPartRate << '\t'
                << cSizePart << '\t' << cSizePartErr << '\t'
                << cMultPart << '\t' << cMultPartErr << '\t'
                << ClustPartRate << '\t' << ClustPartRateErr << '\t';

            RPCarea += stripArea * nStripsPart;
            MeanNoiseRate += MeanPartRate * stripArea * nStripsPart;
            ClusterRate += ClustPartRate * stripArea * nStripsPart;
            ClusterSDev += (cSizePart==0)
                ? 0.
                : ClusterRate*cSizePartErr/cSizePart;
        }

        MeanNoiseRate /= RPCarea;
        ClusterRate /= RPCarea;
        ClusterSDev /= RPCarea;

        outputRateCSV << MeanNoiseRate << '\t'
            << ClusterRate << '\t' << ClusterSDev << '\t';
    }
}

```

2869 *Source Code B.19: Description of rate result calculation and writing into the CSV output Offline-Rate.csv.
 Are saved into the file for each detector, the mean partition rate, cluster size and cluster mutiplicity, along with
 their errors, for each partition and as well as a detector average.*

2870 **Muon performance variables** are computed and written in the output file for each detector parti-
 2871 tions as shown through Sources Code B.20. The variables that are written for each partition are:

- 2872 ● The muon efficiency, `eff`, extracted from the histogram `Efficiency0_H`. It is reminded that
2873 this offline tool doesn't include any tracking algorithm to identify muons from the beam and
2874 only relies on the hits arriving in the time window corresponding to the beam time. The con-
2875 tent of the efficiency histogram is thus biased by the noise/gamma background contribution
2876 into this window and is thus corrected by estimating the muon data content in the peak re-
2877 gion knowing the noise/gamma content in the rate calculation region. Both time windows
2878 being different, the choice was made to normalise the noise/gamma background calculation
2879 window to it's equivalent beam window in order to have comparable values using the variable
2880 `windowRatio`. Finally, to estimate the data ratio in the peak region, the variable `DataRatio`
2881 is defined as the ratio in between the estimated mean cluster multiplicity of the muons in the
2882 peak region, `MuonCM`, and of the total mean cluster multiplicity in the peak region, `PeakCM`.
2883 `MuonCM` is itself defined as the difference in between the total mean cluster multiplicity in the
2884 peak region and the normalised mean noise/gamma cluster multiplicity calculated outside of
2885 the peak region. The statistical error related to the efficiency, `eff_err`, is computed using a
2886 binomial distribution, as the efficiency measure the probability of "success" and "failure" to
2887 detect muons.
- 2888 ● The mean muon cluster size, `MuonCS`, is calculated using the total mean cluster size and multi-
2889 plicity in the peak region, respectively extracted from histograms `MuonCSize_H` and `MuonCMult_H`,
2890 the noise/gamma background mean cluster size and normalised multiplicity, extracted from
2891 `NoiseCSize_H` and `NoiseCMult_H`, and of the estimated muon cluster multiplicity `MuonCM` pre-
2892 viously explicated. The associated statistical error, `MuonCM_err`, is calculated using the propa-
2893 gation of errors of the mentioned variables.
- 2894 ● The mean muon cluster multiplicity in the peak region, `MuonCM`, explicated above whose sta-
2895 tistical error, `MuonCM_err`, is the sum of statistical error associated to the total mean clus-
2896 ter multiplicity in the peak reagion, `PeakCM_err`, and of the mean noise/gamma cluster size,
2897 `NoiseCM_err`.

2898 In addition to these 2 CSV files, the histograms are saved in ROOT file `Scan00XXXX_HVY_Offline.root`
2899 as explained in section B.2.1.1.

2900

```

for (UInt tr = 0; tr < GIFInfra->GetNTrolleys(); tr++) {
    UInt T = GIFInfra->GetTrolleyID(tr);
    for (UInt sl = 0; sl < GIFInfra->GetNSlots(tr); sl++) {
        UInt S = GIFInfra->GetSlotID(tr,sl) - 1;
        for (UInt p = 0; p < GIFInfra->GetNPartitions(tr,sl); p++) {
            float noiseWindow =
                BMTDCWINDOW - TIMEREJECT - 2*PeakWidth.rpc[T][S][p];
            float peakWindow = 2*PeakWidth.rpc[T][S][p];
            float windowRatio = peakWindow/noiseWindow;

            float PeakCM = MuonCMult_H.rpc[T][S][p]->GetMean();
            float PeakCS = MuonCSize_H.rpc[T][S][p]->GetMean();
            float NoiseCM = NoiseCMult_H.rpc[T][S][p]->GetMean() *windowRatio;
            float NoiseCS = NoiseCSize_H.rpc[T][S][p]->GetMean();
            float MuonCM = (PeakCM<NoiseCM) ? 0. : PeakCM-NoiseCM;
            float MuonCS = (MuonCM==0 || PeakCM*PeakCS<NoiseCM*NoiseCS)
                ? 0.
                : (PeakCM*PeakCS-NoiseCM*NoiseCS) / MuonCM;
            float PeakCM_err = (MuonCMult_H.rpc[T][S][p]->GetEntries()==0.)
                ? 0.
                : 2*MuonCMult_H.rpc[T][S][p]->GetStdDev() /
                    sqrt(MuonCMult_H.rpc[T][S][p]->GetEntries());
            float PeakCS_err = (MuonCSize_H.rpc[T][S][p]->GetEntries()==0.)
                ? 0.
                : 2*MuonCSize_H.rpc[T][S][p]->GetStdDev() /
                    sqrt(MuonCSize_H.rpc[T][S][p]->GetEntries());
            float NoiseCM_err = (NoiseCMult_H.rpc[T][S][p]->GetEntries()==0.)
                ? 0.
                : windowRatio*2*NoiseCMult_H.rpc[T][S][p]->GetStdDev() /
                    sqrt(NoiseCMult_H.rpc[T][S][p]->GetEntries());
            float NoiseCS_err = (NoiseCSize_H.rpc[T][S][p]->GetEntries()==0.)
                ? 0.
                : 2*NoiseCSize_H.rpc[T][S][p]->GetStdDev() /
                    sqrt(NoiseCSize_H.rpc[T][S][p]->GetEntries());
            float MuonCM_err = (MuonCM==0) ? 0. : PeakCM_err+NoiseCM_err;
            float MuonCS_err = (MuonCS==0 || MuonCM==0) ? 0.
                : (PeakCS*PeakCM_err + PeakCM*PeakCS_err +
                    NoiseCS*NoiseCM_err + NoiseCM*NoiseCS_err +
                    MuonCS*MuonCM_err) / MuonCM;

            float DataRatio = MuonCM/PeakCM;
            float DataRatio_err = (MuonCM==0) ? 0.
                : DataRatio*(MuonCM_err/MuonCM + PeakCM_err/PeakCM);
            float eff = DataRatio*Efficiency0_H.rpc[T][S][p]->GetMean();
            float eff_err = DataRatio*2*Efficiency0_H.rpc[T][S][p]->GetStdDev() /
                sqrt(Efficiency0_H.rpc[T][S][p]->GetEntries()) +
                Efficiency0_H.rpc[T][S][p]->GetMean()*DataRatio_err;

            outputEffCSV << eff << '\t' << eff_err << '\t'
                << MuonCS << '\t' << MuonCS_err << '\t'
                << MuonCM << '\t' << MuonCM_err << '\t';
        }
    }
}

```

2901

Source Code B.20: Description of efficiency result calculation and writing into the CSV output Offline-L0-EffCl.csv. Are saved into the file for each detector, the efficiency, corrected taking into account the background in the peak window of the time profile, muon cluster size and muon cluster multiplicity, along with their errors, for each partition and as well as a detector average.

2902

2903 B.7 Current data Analysis

2904 Detectors under test at GIF++ are connected both to a CAEN HV power supply and to a CAEN
2905 ADC that reads the currents inside of the RPC gaps bypassing the supply cable. During data tak-
2906 ing, the webDCS records into a ROOT file called `Scan00XXXX_HVY_CAEN.root` histograms with the
2907 monitored parameters of both CAEN devices. Are recorded for each RPC channels (in most cases,
2908 a channel corresponds to an RPC gap):

- 2909 • the effective voltage, HV_{eff} , set by the webDCS using the PT correction on the CAEN power
2910 supply,
- 2911 • the applied voltage, HV_{app} , monitored by the CAEN power supply, and the statistical error
2912 related to the variations of this value through time to follow the variation of the environmental
2913 parameters defined as the RMS of the histogram divided by the square root of the number of
2914 recorded points,
- 2915 • the monitored current, I_{mon} , monitored by the CAEN power supply, and the statistical error
2916 related to the variations of this value through time to follow the variation of the environmental
2917 parameters defined as the RMS of the histogram divided by the square root of the number of
2918 recorded points,
- 2919 • the corresponding current density, J_{mon} , defined as the monitored current per unit area,
2920 $J_{mon} = I_{mon}/A$, where A is the active area of the corresponding gap,
- 2921 • the ADC current, I_{ADC} , recorded through the CAEN ADC module that monitors the dark
2922 current in the gap itself. First of all, the resolution of such a module is better than that of
2923 CAEN power supplies and moreover, the current is not read-out through the HV supply line
2924 but directly at the chamber level giving the real current inside of the detector. The statistical
2925 error is defined as the RMS of the histogram distribution divided by the square root of the
2926 number of recorded points.

2927 Once extracted through a loop over the element of GIF++ infrastructure via the C++ macro
2928 `GetCurrent()`, these parameters, organised in 9 columns per detector HV supply line, are written in
2929 the output CSV file `Offline-Current.csv`. The macro can be found in the file `Current.cc`.

References

- [1] T. Massam et al. “Experimental observation of antideuteron production”. In: *Il Nuovo Cimento A* 63 (1965), pp. 10–14.
- [2] UA1 Collaboration. “Experimental observation of isolated large transverse energy electrons with associated missing energy at $s = 540 \text{ GeV}$ ”. In: *Physics Letters B* 122 (1983), pp. 103–116.
- [3] UA2 Collaboration. “Observation of single isolated electrons of high transverse momentum in events with missing transverse energy at the CERN pp collider”. In: *Physics Letters B* 122 (1983), pp. 476–485.
- [4] UA1 Collaboration. “Experimental observation of lepton pairs of invariant mass around $95 \text{ GeV}/c^2$ at the CERN SPS collider”. In: *Physics Letters B* 126 (1983), pp. 398–410.
- [5] UA2 Collaboration. “Evidence for $Z_0 \rightarrow e^+e^-$ at the CERN pp collider”. In: *Physics Letters B* 129 (1983), pp. 130–140.
- [6] ALEPH Collaboration. “Determination of the number of light neutrino species”. In: *Physics Letters B* 231 (1989), pp. 519–529.
- [7] CERN, ed. (1985).
- [8] CERN, ed. (1986).
- [9] CERN, ed. (1994).
- [10] CERN, ed. (1998).
- [11] CERN, ed. (1999).
- [12] CERN. Geneva. LHC Experiments Committee. *Letter of Intent for A Large Ion Collider Experiment [ALICE]*, note = CERN-LHCC-93-016. Tech. rep. ALICE Collaboration, 1993.
- [13] CERN. Geneva. LHC Experiments Committee. *ATLAS : technical proposal for a general-purpose pp experiment at the Large Hadron Collider at CERN*, note = CERN-LHCC-94-43. Tech. rep. ATLAS Collaboration, 1994.
- [14] CERN. Geneva. LHC Experiments Committee. *CMS : letter of intent by the CMS Collaboration for a general purpose detector at LHC*, note = CERN-LHCC-92-003. Tech. rep. CMS Collaboration, 1992.
- [15] CERN. Geneva. LHC Experiments Committee. *LHCb : letter of intent*. Tech. rep. CERN-LHCC-95-5. LHCb Collaboration, 1995.
- [16] L. Evans and P. Bryant. “LHC Machine”. In: *JINST* 3 (2008). S08001.
- [17] CMS Collaboration ATLAS Collaboration. “Combined Measurement of the Higgs Boson Mass in pp Collisions at $\sqrt{s} = 7$ and 8 TeV with the ATLAS and CMS Experiments”. In: *Physical Review Letters* 114 (2015). 191803.
- [18] LHCb Collaboration. “Observation of $J/\psi p$ Resonances Consistent with Pentaquark States in $\Lambda_b^0 \rightarrow J/\psi K^- p$ Decays”. In: *Physical Review Letters* 115 (2015). 072001.

- [19] LHCb Collaboration. “Observation of $J/\psi\phi$ Structures Consistent with Exotic States from Amplitude Analysis of $B^+ \rightarrow J/\psi\phi K^+$ Decays”. In: *Physical Review Letters* 118 (2017). 022003.
- [20] CERN. Geneva. *High-Luminosity Large Hadron Collider (HL-LHC) Technical Design Report V. 0.1*. Tech. rep. CERN-2017-007-M. 2017.
- [21] CERN. Geneva. LHC Experiments Committee. *The CMS muon project : Technical Design Report*. Tech. rep. CERN-LHCC-97-032. CMS Collaboration, 1997.
- [22] CERN. Geneva. LHC Experiments Committee. *CMS, the Compact Muon Solenoid : technical proposal*. Tech. rep. CERN-2015-005. 2015.
- [23] CERN. Geneva. LHC Experiments Committee. *The Phase-2 Upgrade of the CMS Muon Detectors*. Tech. rep. CERN-LHCC-2017-012, CMS-TDR-016. CMS Collaboration, 2017.
- [24] CERN. Geneva. LHC Experiments Committee. *The Phase-2 Upgrade of the CMS Level-1 Trigger - Interim Report to the LHCC*. Tech. rep. CERN-LHCC-2017-013, CMS-TDR-017. CMS Collaboration, 2017.
- [25] CERN. Geneva. LHC Experiments Committee. *Technical Proposal for the Phase-II Upgrade of the CMS Detector*. Tech. rep. CERN-LHCC-2015-010, CMS-TDR-15-02. CMS Collaboration, 2015.
- [26] CERN. Geneva. LHC Experiments Committee. *High-Luminosity Large Hadron Collider (HL-LHC) Preliminary Design Report*. Tech. rep. CERN-LHCC-94-38. CMS Collaboration, 1994.
- [27] R. Santonico and R. Cardarelli. “Development of resistive plate counters”. In: *Nucl. Instr. Meth. Phys. Res.* 187 (1981), pp. 377–380.
- [28] Yu.N. Pestov and G.V. Fedotovich. *A picosecond time-of-flight spectrometer for the VEPP-2M based on local-discharge spark counter*. Tech. rep. SLAC-TRANS-0184. SLAC, 1978.
- [29] W.W. Ash, ed. *Spark Counter With A Localized Discharge*. Vol. SLAC-R-250. 1982, pp. 127–131.
- [30] I. Crotty et al. “The non-spark mode and high rate operation of resistive parallel plate chambers”. In: *NIMA* 337 (1993), pp. 370–381.
- [31] I. Crotty et al. “Further studies of avalanche mode operation of resistive parallel plate chambers”. In: *NIMA* 346 (1994), pp. 107–113.
- [32] R. Cardarelli et al. “Avalanche and streamer mode operation of resistive plate chambers”. In: *NIMA* 382 (1996), pp. 470–474.
- [33] E. Cerron Zeballos et al. “A new type of resistive plate chamber: The multigap RPC”. In: *NIMA* 374 (1996), pp. 132–135.
- [34] M.C.S. Williams. “The development of the multigap resistive plate chamber”. In: *Nucl. Phys. B* 61 (1998), pp. 250–257.
- [35] H. Czyrkowski et al. “New developments on resistive plate chambers for high rate operation”. In: *NIMA* 419 (1998), pp. 490–496.
- [36] P. Camarri et al. “Streamer suppression with SF₆ in RPCs operated in avalanche mode”. In: *NIMA* 414 (1998), pp. 317–324.
- [37] E. Cerron Zeballos et al. “Effect of adding SF₆ to the gas mixture in a multigap resistive plate chamber”. In: *NIMA* 419 (1998), pp. 475–478.
- [38] CERN. Geneva. LHC Experiments Committee. *ATLAS muon spectrometer: Technical design report*. Tech. rep. CERN-LHCC-97-22. ATLAS Collaboration, 1997.

BIBLIOGRAPHY

- 3010 [39] CERN. Geneva. LHC Experiments Committee. *ALICE Time-Of-Flight system (TOF) : Technical Design Report*. Tech. rep. CERN-LHCC-2000-012. ALICE Collaboration, 2000.
- 3011
- 3012 [40] The CALICE collaboration. “First results of the CALICE SDHCAL technological prototype”. In: *JINST* 11 (2016).
- 3013
- 3014 [41] PoS, ed. *Density Imaging of Volcanoes with Atmospheric Muons using GRPCs*. International Europhysics Conference on High Energy Physics - HEP 2011. 2011.
- 3015
- 3016 [42] C. Lippmann. “Detector Physics of Resistive Plate Chambers”. PhD thesis. Johann Wolfgang Goethe-Universität, 2003.
- 3017
- 3018 [43] M. Abbrescia et al. “Properties of C2H2F4-based gas mixture for avalanche mode operation of resistive plate chambers”. In: *NIMA* 398 (1997), pp. 173–179.
- 3019
- 3020 [44] G. Battistoni et al. “Sensitivity of streamer mode to single ionization electrons”. In: *NIMA* 235 (1985), pp. 91–97.
- 3021
- 3022 [45] W. Riegler. “Induced signals in resistive plate chambers”. In: *NIMA* 491 (2002), pp. 258–271.
- 3023
- 3024 [46] E. Cerron Zeballos et al. “A comparison of the wide gap and narrow gap resistive plate chamber”. In: *NIMA* 373 (1996), pp. 35–42.
- 3025
- 3026 [47] M. Abbrescia et al. “Cosmic ray tests of double-gap resistive plate chambers for the CMS experiment”. In: *NIMA* 550 (2005), pp. 116–126.
- 3027
- 3028 [48] ALICE Collaboration. “A study of the multigap RPC at the gamma irradiation facility at CERN”. In: *NIMA* 490 (2002), pp. 58–70.
- 3029
- 3030 [49] B. Bonner et al. “A multigap resistive plate chamber prototype for time-of-flight for the STAR experiment at RHIC”. In: *NIMA* 478 (2002), pp. 176–179.
- 3031
- 3032 [50] S. Yang et al. “Test of high time resolution MRPC with different readout modes for the BESIII upgrade”. In: *NIMA* 763 (2014), pp. 190–196.
- 3033
- 3034 [51] A. Akindinov et al. “RPC with low-resistive phosphate glass electrodes as a candidate for the CBM TOF”. In: *NIMA* 572 (2007), pp. 676–681.
- 3035
- 3036 [52] JINST, ed. *Development of the MRPC for the TOF system of the MultiPurpose Detector*. RPC2016: XII Workshop on Resistive Plate Chambers and Related Detectors. 2016.
- 3037
- 3038 [53] M.C.S. Williams. “Particle identification using time of flight”. In: *Journal of Physics G* 39 (2012).
- 3039
- 3040 [54] A. Alici et al. “Aging and rate effects of the Multigap RPC studied at the Gamma Irradiation Facility at CERN”. In: *NIMA* 579 (2007), pp. 979–988.
- 3041
- 3042 [55] M. Abbrescia et al. “The simulation of resistive plate chambers in avalanche mode: charge spectra and efficiency”. In: *NIMA* 431 (1999), pp. 413–427.
- 3043
- 3044 [56] M. Abbrescia et al. “Study of long-term performance of CMS RPC under irradiation at the CERN GIF”. In: *NIMA* 533 (2004), pp. 102–106.
- 3045
- 3046 [57] H.C. Kim et al. “Quantitative aging study with intense irradiation tests for the CMS forward RPCs”. In: *NIMA* 602 (2009), pp. 771–774.
- 3047
- 3048 [58] S. Agosteo et al. “A facility for the test of large-area muon chambers at high rates”. In: *NIMA* 452 (2000), pp. 94–104.
- 3049
- 3050 [59] PoS, ed. *CERN GIF ++ : A new irradiation facility to test large-area particle detectors for the high-luminosity LHC program*. Vol. TIPP2014. 2014, pp. 102–109.
- 3051
- 3052 [60] A. Fagot. *GIF++ DAQ v4.0*. 2017. URL: https://github.com/afagot/GIF_DAQ.
- 3053 [61] CAEN. *Mod. V1190-VX1190 A/B, 128/64 Ch Multihit TDC*. 14th ed. 2016.

BIBLIOGRAPHY

- 3053 [62] CAEN. *Mod. VI718 VME USB Bridge*. 9th ed. 2009.
- 3054 [63] W-Ie-Ne-R. *VME 6021-23 VXI*. 5th ed. 2016.
- 3055 [64] Wikipedia. *INI file*. 2017. URL: https://en.wikipedia.org/wiki/INI_file.
- 3056 [65] S. Carrillo A. Fagot. *GIF++ Offline Analysis v6*. 2017. URL: https://github.com/afagot/GIF_OfflineAnalysis.
- 3057